

THE DRAPER TECHNOLOGY DIGEST

The Draper Technology Digest (CSDL-R-3009) is published annually by The Charles Stark Draper Laboratory, Inc., 555 Technology Square, Cambridge, MA 02139. Requests for individual copies or permission to reprint the text should be submitted to:

Draper Laboratory
Media Services
Phone: (617) 258-1811
Fax: (617) 258-1800
E-mail: techdigest@draper.com

Editor-in-Chief
Dr. George Schmidt

Creative Director
Charya Peou

Designer
Pamela Toomey

Editor
Beverly Tuzzalino

Photography Coordinator
Drew Crete

Photography
Jay Couturier

Copyright © 2007 by The Charles Stark Draper Laboratory, Inc. All rights reserved.

Front cover photo:
Improved accuracy of MEMS-based Inertial Navigation System achieved with coordinated gimbal movements during operational calibration updates.

Table of contents

Letter from the President and CEO, James D. Shields	2
Introduction by Vice President, Engineering, Eli Gai	3
Papers	
Innovative Indoor Geolocation Using RF Multipath Diversity Donald E. Gustafson, John M. Elwell, J. Arnold Soltz	4
Engineering MEMS Resonators with Low Thermoelastic Damping Amy E. Duwel, Rob N. Candler, Thomas W. Kenny, Mathew Varghese	14
Improving Lunar Return Entry Footprints Using Enhanced Skip Trajectory Guidance Zachary R. Putnam, Robert D. Braun, Sarah H. Bairstow, and Gregory H. Barton	24
A Deep Integration Estimator for Urban Ground Navigation Dale Landis, Tom Thorvaldsen, Barry Fink, Peter Sherman, Steven Holmes	34
Error Sources in In-Plane Silicon Tuning-Fork MEMS Gyroscopes Marc S. Weinberg, Anthony Kourepenis	42
Model-Based Variational Smoothing and Segmentation for Diffusion Tensor Imaging in the Brain Mukund N. Desai, David N. Kennedy, Rami S. Mangoubi, et al.	56
2006 Published Papers	70
Patents	
Patents Introduction	75
Multi-gimbaled borehole navigation system Patent # 7,093,370 B2 Date Issued: August 22, 2006 Mitchell L. Hansberry, Michael E. Ash, Richard T. Martorana	76
Flexural plate wave sensor Patent # 7,109,633 B2 Date Issued: September 19, 2006 Marc S. Weinberg, Brian Cunningham, Eric M. Hildebrandt	79
2006 Patents Issued	82
The 2006 Draper Distinguished Performance Awards	83
The 2007 Charles Stark Draper Prize	84
The 2006 Howard Musoff Student Mentoring Award	86
2006 Graduate Research Theses	87
2006 Technology Exposition	88



James D. Shields,
President and CEO

As Draper's new president, it is my pleasure to introduce this year's edition of The Draper Technology Digest. An important element of our strategy is to focus on a limited set of critical technical capabilities and to maintain our skills in these areas at a world-class level. These capabilities are:

- Guidance, navigation, and control.
- Autonomous air, land, sea, and space systems.
- Reliable, fault-tolerant embedded systems.
- Miniature, low-power electronic and mechanical systems.
- Large-scale networked systems integration.
- Biomedical engineering.

In each of these areas, we strive to be recognized as technology leaders through innovative application of technology to solve sponsors' problems. Technology leadership also requires that our staff share their accomplishments with the broader community by publishing, presenting at conferences, and serving on advisory boards and panels.

The Digest supports our efforts to encourage publishing by recognizing the authors of the best papers that were produced in the previous year. It also provides a forum to consolidate in a single volume a sampling of the technical accomplishments across the range of our critical capabilities. The six papers this year cover topics in guidance, navigation and control, microelectromechanical systems (MEMS), and biomedical engineering. All were either published in a refereed journal or presented at a prestigious technical conference.

Each year, during National Engineers Week, Eli Gai, our Vice President of Engineering, presents an award to the authors of the best technical paper published in the prior calendar year. Eli also gives awards recognizing the best patent, the most effective task leader, and an outstanding mentor to students who work at the Laboratory. I congratulate the winners of these awards, whose accomplishments are described in this issue.

Draper's commitment to advanced technical education through the Draper Fellows program, where Masters and PhD candidates are supported financially and academically by allowing them to do their thesis research on a Draper project, continued for the 34th consecutive year. We recognize this year's graduates by listing them and their thesis titles.

Eli Gai,
Vice President, Engineering



This issue marks the beginning of the second decade of the Draper Technology Digest. The fundamental purpose of the Digest is to recognize the outstanding achievements of Draper's technical staff, as reflected in the papers published and patents awarded during the most recent calendar year. The Digest also recognizes the important mentoring work performed by Draper's technical staff by honoring the recipient of the Howard Musoff Student Mentoring Award. This year's Digest features six excellent technical papers highlighting important hardware, software, and systems engineering achievements in support of our business areas of Space, Tactical, and Biomedical Systems. Also featured in this year's Digest are the recipients of the Best Patent issued in 2006 and the winner of the Howard Musoff Student Mentoring Award for 2006.

The first paper in this issue by Donald Gustafson, John Elwell, and J. Arnold Soltz was selected to receive the Vice President's Award for Best Paper for 2006. In this paper, a new approach to indoor geolocation in multipath environments based on geometry-based modeling is described. Simulation results show that this approach significantly improves indoor geolocation accuracy.

The second paper by Amy E. Duwel, Rob N. Chandler, Thomas W. Kenny, and Mathew Varghese describes new tools to evaluate and optimize microelectromechanical system (MEMS) structures for low thermoplastic damping. It includes an example that illustrates the use of the tools to design devices with higher quality (Q) factors, which results in improved sensor performance.

The third paper by Zach Putnam, Robert Braun, Sarah Bairstow, and Greg Barton describes modifications of the skip trajectory entry guidance used in the Apollo Program for use in the planned Crew Exploration Vehicle (CEV). A simulation shows that the modified guidance significantly improves the entry footprint of the CEV for the lunar return mission.

The fourth paper by Dale Landis, Tom Thorvaldsen, Barry Fink, Peter Sherman, and Steven Holmes describes optimal estimation techniques used to combine a Global Positioning System (GPS)/inertial Deep Integration algorithm with measurements from

other sensors to provide accurate position information over extended missions for a personal, wearable navigation system. A field test of the system conducted under realistic GPS-stressed conditions demonstrates the practicality of the design.

The fifth paper by Marc Weinberg and Tony Kourepenis describes the error sources limiting the performance of silicon tuning-fork gyroscopes (TFGs) and the techniques that can be used to minimize them. The study includes three different sensors: the Honeywell/Draper TFG, the Systron Donner/BEI quartz sensor, and the Analog Device/ADXRS.

The last paper by Mukund N. Desai, David N. Kennedy, Rami S. Mangoubi, Jayant Shah, Clem Karl, Andrew Worth, Nikos Makris, and Homer Pien describes the application of a unified algorithm to smoothing and segmentation of diffusion tensor imaging in the brain. Results show improvement in brain image quality both qualitatively and quantitatively, as well as the robustness of the algorithm in the presence of added noise.

This year, two patents were selected for the Vice President of Engineering's Award for Best Patent: Multi-Gimbaled Borehole Navigation System authored by Mitchell Hansberry, Richard Martorana, and the late Michael Ash, and Flexural Plate Wave Sensor authored by Marc Weinberg, Brian Cunningham, and Eric Hildebrant.

Nine staff members were nominated for the Howard Musoff Student Mentoring Award, and the winner for 2006 was Laura Forrest. Details on the award and Laura's accomplishments can be found on page 86.

Innovative Indoor Geolocation Using RF Multipath Diversity

Donald E. Gustafson, John M. Elwell, J. Arnold Soltz

Copyright © 2006, The Charles Stark Draper Laboratory, Inc. Presented at IEEE PLANS 2006, San Diego, CA, April 25-27, 2006

BEST PAPER
2006

abstract

A new concept is presented for indoor geolocation in multipath environments where direct paths are sometimes undetectable. In contrast to previous statistically-based approaches, the multipath delays are modeled using a geometry-based argument. Assuming a series of specular reflections off planar surfaces, the model contains a maximum of three unknown multipath parameters per path that may be estimated when geolocation accuracy is sufficiently high. If some of the direct paths subsequently become undetectable, it is possible under certain conditions to maintain geolocation accuracy using only the indirect path length measurements. The new concept is illustrated via simulation using a relatively simple representative scenario. Performance is compared to a traditional method that uses only direct path measurements, indicating the potential for significantly improved indoor geolocation accuracy in environments dominated by multipath. Since the estimated multipath parameters are geometry-dependent, this approach allows the possibility of building up indoor map information as the geolocation process commences.

INTRODUCTION

A number of approaches have been suggested for locating and tracking people and objects inside buildings where Global Positioning System (GPS) operation is denied. Most of these use radio frequency (RF) phenomena and are limited in performance by a single phenomenon: RF multipath. Performance has relied on the ability to determine the direct path distance from a number of reference sources to the person or object of interest. Within indoor environments, the received signal strength of indirect paths is often greater than the direct paths, sometimes resulting in undetected direct paths and detected indirect paths.^[1] In these situations, methods based on direct paths cannot maintain accurate tracking over a period of time, particularly when the object being tracked moves in an unpredictable fashion. This limitation can be overcome in some cases by exploiting the geolocation information contained in the indirect path measurements.

This paper presents a new solution to this problem. Rather than treating multipath signals as noise and attempting to mitigate multipath-induced errors, this technique exploits the multipath signals by using them as additional measurements within a nonlinear filter. The nonlinear filter uses simultaneous indirect and direct path measurements to build up parametric models of all detected indirect paths. If one or more direct paths are subsequently lost, the nonlinear filter is able to maintain tracking by navigating off the indirect path measurements. Previous approaches to indirect path length modeling have relied on statistical models (e.g., direct-path length plus bias). In contrast, our approach is geometry-based. Of importance is the fact that the indirect path distance after a sequence of specular reflections off planar surfaces can be modeled exactly using only two parameters in two dimensions and three parameters in three dimensions, *for any number of reflections*. These parameters are estimated in real time in the nonlinear filter.

PROBLEM FORMULATION

A typical indoor multipath RF signature is shown in Figure 1, assuming a bandwidth of 200 MHz.^[2] Received signal amplitude is plotted vs. time delay. The direct path amplitude is below the detection threshold, while the amplitude of several indirect paths is higher than threshold. In particular, the strongest path is the first indirect path, which results in an error of 5.3 m for a geolocation system based on direct path measurements.

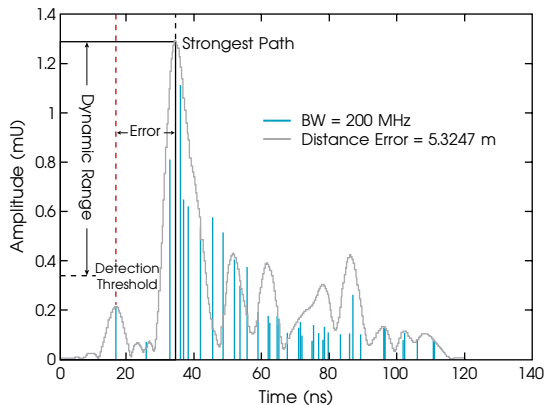


Figure 1. Typical indoor multipath RF signature.

Indoor Geolocation System Architecture

The architecture for the indoor geolocation system under consideration is shown in Figure 2. Without loss of generality, we consider the problem of tracking a single transponding tag. The space is instrumented with multiple RF sources at known and fixed locations (nodes). Means are available to identify the RF source without error. The signal received at a node after reception and retransmission from the tag is modeled as

$$y(t) = \sum_{i=0}^m a_i(t)z(t-2\tau_i(t)-\tau_d) + n(t),$$

where $z(t)$ is the transmitted signal, subscript i refers to the i^{th} path, ($i = 0$ is the direct path, and $i > 0$ is an indirect path), $a_i(t)$ is the complex attenuation factor, $\tau_i(t)$ is the path delay, $n(t)$ is noise, m is the number of indirect paths, and τ_d is the processing delay within the tag, which is assumed to be known. The direct path delay is $\tau_0(t) = \|r(t)-s\|/c$, where $r(t)$ is the tag location, s is the node location, and c is the signal propagation speed.

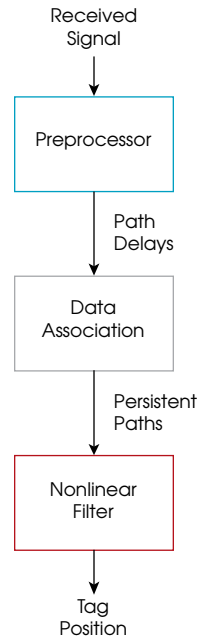


Figure 2. Geolocation system architecture.

The differential delay is the excess delay of the indirect path relative to the direct path:

$$\delta\tau_i(t) = \tau_i(t) - \tau_0(t) > 0; i = 1, 2, \dots, m.$$

A preprocessor is used to estimate all detected path delays. A number of methods have been developed for this purpose. In Reference [3], the received signal was modeled as the sum of the direct-path signal and a delayed version (one indirect path), with the indirect path amplitude less than the direct path amplitude. Using a first-order finite impulse response filter model, the differential delay and indirect path amplitude were estimated using the autocorrelation of the received signal. Another approach^[4] used maximum likelihood to estimate the direct path delay in a multipath environment. In Reference [5], multipath measurements were used to increase the accuracy of the direct path delay estimate. This method required an a priori statistical model of indirect path delay statistics. Differential delays were modeled as biases in Reference [6], and algorithms were developed for multipath detection and bias estimation. In Reference [7], the known autocorrelation function within a GPS receiver was used for multipath mitigation. In Reference [8], GPS differential delays were estimated using a multiple-hypothesis Kalman filter. Differential delays were modeled as biases in Reference [9], and a particle filter was used for joint estimation of bias and tag location in an

indoor environment. The statistical bias model was generated using ultra-wideband measurements.

In practice, it is important to correctly associate each calculated delay with the direct path or a specific indirect path (i.e., a specific sequence of reflections off the same set of reflecting planes). This is not a straightforward process in some scenarios with multiple nodes and complex environments containing many reflecting surfaces of various orientations and size. The problem is made challenging by the presence of crossovers between pairs of time delays, appearance of new paths, disappearance and reappearance of existing paths, and the presence of noise. In order to be effective, the *data association* algorithm should be capable of detecting path persistence, so that the largest possible number of measurements for each path are obtained; this enhances the accuracy of multipath parameter estimation.

All the methods mentioned above rely on a single parameter, the differential delay, for the multipath model. Multipath estimation is based on a priori statistical models of differential delay, typically as a bias (including means to detect sudden bias changes) or output of a low-order linear filter. In contrast, the approach suggested here is based on a geometrical model and the assumption that the indirect path length is the result of a series of specular reflections off planar surfaces. This model contains several geometry-based parameters and does not depend on a priori statistical models of multipath delay. Thus, use of this model allows the possibility of inferring geometrical structure within the indoor environment. We now develop the measurement model that is appropriate for use in a nonlinear filter that is capable of joint estimation of tag location and the geometry-based multipath parameters.

GEOMETRY-BASED MEASUREMENT MODEL

In the following, time delays have been converted into distances using the known signal propagation velocity in air. The indirect path distance after a sequence of m specular reflections off planar surfaces is derived as follows. Referring to Figure 3, the relevant equations are, for $i = 1, 2, \dots, m$

$$p_i = s + \sum_{j=1}^i d_j w_j \quad (1)$$

$$u_i^T p_i = b_i \quad (2)$$

$$w_i = E_i w_{i+1}, E_i = I - 2u_i u_i^T, E_i = E_i^{-1}; \quad (3)$$

$$u_i^T w_i = -\cos \theta_i \quad (4)$$

and

$$r = p_m + d_{m+1} w_{m+1} \quad (5)$$

$$d = \sum_{j=1}^{m+1} d_j \quad (6)$$

where p_i is the specular point on the i^{th} plane, d_1 is the distance from the source to p_1 , $\{d_i; i = 2, 3, \dots, m\}$ is the

distance from p_{i-1} to p_i , d_{m+1} is the distance from p_m to r , w_i is the unit vector along the incident ray, b_i is the distance of the plane to the origin of the navigation frame, u_i is the unit vector normal to the plane, and d is indirect path length. From (1), (5), and (6),

$$r = s + \sum_{i=1}^{m+1} d_i w_i = s + \sum_{i=1}^m d_i (w_i - w_{m+1}) + d w_{m+1} \quad (7)$$

Thus,

$$\begin{aligned} d &= w_{m+1}^T r - w_{m+1}^T s + \sum_{i=1}^m d_i (1 - w_{m+1}^T w_i) \\ &= w_{m+1}^T r - w_{m+1}^T s + \sum_{i=1}^{m-1} d_i (1 - w_{m+1}^T w_i) + d_m (1 - w_{m+1}^T w_m) \end{aligned} \quad (8)$$

From (3) and (4),

$$w_{i+1} = w_i + 2u_i \cos \theta_i; \quad i = 1, 2, \dots, m \quad (9)$$

Thus,

$$d = w_{m+1}^T r - w_{m+1}^T s + \sum_{i=1}^{m-1} d_i (1 - w_{m+1}^T w_i) + 2d_m \cos^2 \theta_m \quad (10)$$

But, from (1) and (2),

$$d_i = \frac{u_i^T s - b_i + \sum_{j=1}^{i-1} d_j u_i^T w_j}{\cos \theta_i}; \quad i = 1, 2, \dots, m \quad (11)$$

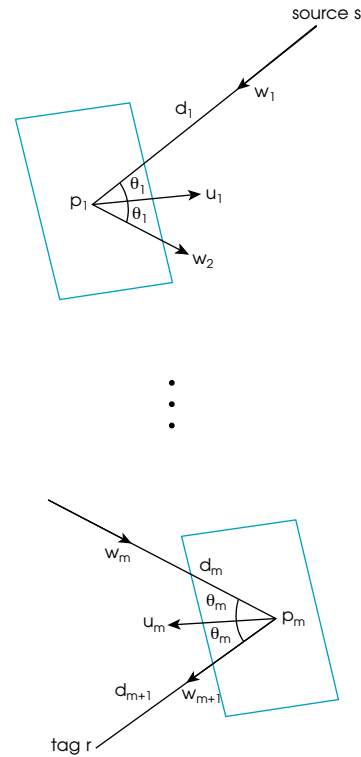


Figure 3. Geometry for m specular reflections.

Thus

$$\begin{aligned} d &= w_{m+1}^T r - w_{m+1}^T s + \sum_{i=1}^{m-1} d_i (1 - w_{m+1}^T w_i) \\ &\quad + 2[u_m^T s - b_m + \sum_{j=1}^{m-1} d_j u_m^T w_j] \cos \theta_m \\ &= w_{m+1}^T r - w_m^T s + \sum_{i=1}^{m-1} d_i (1 - w_m^T w_i) - 2b_m \cos \theta_m \end{aligned} \quad (12)$$

Continuing, we find that

$$\begin{aligned} d &= w_{m+1}^T r - w_m^T s + \sum_{i=1}^{m-2} d_i (1 - w_m^T w_i) - 2b_m \cos \theta_m \\ &\quad + 2[u_{m-1}^T s - b_{m-1} + \sum_{j=1}^{m-2} d_j u_{m-1}^T w_j] \cos \theta_{m-1} \\ &= w_{m+1}^T r - w_{m-1}^T s + \sum_{i=1}^{m-2} d_i (1 - w_{m-1}^T w_i) \\ &\quad - 2b_{m-1} \cos \theta_{m-1} - 2b_m \cos \theta_m \end{aligned} \quad (13)$$

By induction, we see from (8), (12) and (13) that for $k=1, 2, \dots, m+1$

$$d = w_{m+1}^T r - w_k^T s + \sum_{i=1}^{k-1} d_i (1 - w_k^T w_i) - 2 \sum_{j=k}^m b_j \cos \theta_j \quad (14)$$

The case of most interest is $k = 1$, which gives

$$d = w_{m+1}^T r - w_1^T s - 2 \sum_{j=1}^m b_j \cos \theta_j \quad (15)$$

which can be written in the form

$$d = w_{m+1}^T r + c_m \quad (16)$$

where

$$c_m = -w_1^T s - 2 \sum_{i=1}^m b_i \cos \theta_i \quad (17)$$

is a scalar offset distance that contains contributions from all m reflections. In (16), w_{m+1} is the unit vector from the last specular point to the tag and contains potentially useful information regarding the geometry of the indoor space.

The multipath parameters $\{w_{m+1}, c_m\}$ vary as the tag moves through the indoor space. If the variations are too large, the parameters may be essentially unobservable, resulting in poor performance. Generally, the variations decrease as the node moves away from the tag. To see this, write (5) in the form

$$r = M_1 s + 2 \sum_{i=1}^m b_i M_{i+1} u_i + d w_{m+1} \quad (18)$$

where

$$M_k = \prod_{i=k}^m E_i, \quad M_{m+1} = I$$

Then

$$w_{m+1} = \text{unit}(r - M_1 s - 2 \sum_{i=1}^m b_i M_{i+1} u_i)$$

and

$$w_{m+1} \rightarrow \text{unit}(-M_1 s) \quad \text{as } s \rightarrow \infty$$

Since M_1 depends only on the orientation of the reflecting planes, w_{m+1} becomes independent of r as $s \rightarrow \infty$. Similarly, from (17),

$$c_m = -w_{m+1}^T M_1 s - 2 \sum_{i=1}^m b_i w_{m+1}^T M_{i+1} u_i \quad (19)$$

so that

$$c_m \rightarrow -w_{m+1}^T M_1 s \quad \text{as } s \rightarrow \infty$$

Thus, c_m also becomes independent of r as $s \rightarrow \infty$. For typical indoor environments and tag motion, parameter values are generally stable enough to allow reasonable tag localization accuracy. A representative example is given in the sequel to illustrate this point. An important limiting case is the problem of navigation using GPS measurements in the presence of multipath. The distance to the nodes (GPS satellites) is essentially infinite and the multipath parameters are *constant* over sufficiently short periods of time where the effects of satellite motion may be ignored. This considerably simplifies the problem of navigating using GPS measurements in multipath environments.

The indirect path parameter set $\{w_{m+1}, c_m\}$ contains three unknown parameters in three-dimensional space and two unknown parameters in two-dimensional space. Importantly, the form of (16) is independent of the number of reflections, although the offset distance is significantly different. Hence, it does not matter that the number of reflections is unknown in practice, and the accuracy of estimating $\{w_{m+1}, c_m\}$ is not affected by the number of reflections. For this reason, the reflection subscript m is dropped in the sequel.

Multipath Geolocation System Design

Equation (16) is in the form of a bilinear measurement equation that can be handled using appropriate recursive nonlinear filtering methods in which the goal is to track the tag location r and estimate the multipath parameters $\{w, c\}$ simultaneously by processing a sequence of noisy measurements of d as the tag moves through the indoor space. Note that this model includes the unknown effects of additional path delays associated with attenuation through materials in which the signal propagation speed is slower than in air.

If the parameters are known exactly, then (16) is in the form of the usual linear measurement equation for a Kalman filter. If the parameter uncertainties are small enough, then tag position can be estimated with reasonable accuracy using an extended Kalman filter. In some practical situations, the uncertainty associated with the initial parameter

estimates may be large enough to preclude the initial use of an extended Kalman filter, and other means (e.g., particle filters, multiple-hypothesis filters, information filters) must be used at least initially to get within the linear range of an extended Kalman filter.

The form of (16) indicates that accurate estimation of the multipath parameters $\{w, c\}$ depends on meeting several conditions: 1) relatively accurate tag location estimates over a sufficient length of time, 2) tag motion sufficient to ensure observability of the parameters, 3) relatively small variation of the of multipath parameters as the tag moves through the indoor environment, and 4) persistence of the sequence of reflections. In the sequel, it is shown for a representative indoor scenario that the parameter variations tend to be relatively small as the tag moves through space, allowing reasonably accurate estimates of the multipath parameters to be obtained.

Data Association

A generic measurement data association algorithm is depicted in Figure 4. At any time, data for all current and past detected indirect paths are stored, both as all past raw measurement associated with that path and the coefficients of low-order ordinary least squares regression models of the path delays. When a new measurement is obtained, the distance to all current paths is calculated by comparing the predicted values in the current database with the new value. If the minimum distance is less than a prespecified threshold, then the closest current path is updated, including the regression model. If the distance exceeds the threshold, a new indirect path is started. Note that new indirect paths may be started if a new path appears, an old path reappears, or a current path changes by a relatively large amount due to tag motion since the last measurement of that indirect path. The output of the data association algorithm is the identity of the path associated with the current measurement.

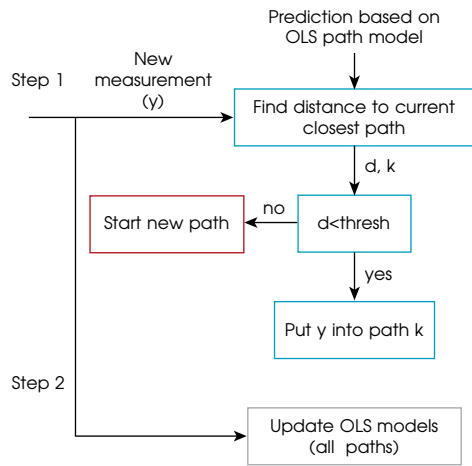


Figure 4. Generic measurement data association algorithm.

Nonlinear Filter

Tracking the tag position in real time is accomplished using a nonlinear filter. A two-step process was used: 1) initialization using a particle filter, and 2) tracking using an extended Kalman filter. The purpose of the particle filter is to reduce the initially large tag position uncertainty to an error that is within the linearization range of the extended Kalman filter. A generic particle filter^[10] can be used for initialization. Assuming no measurement data association errors, the first few direct-path measurements from each node may be correctly identified and processed to reduce the localization error to within the linearization region of an extended Kalman filter.

Recursive estimation of the tag location and the multipath parameters is carried out in two sequential steps: 1) propagation between measurements and 2) updating at a measurement. The tag position is assumed to propagate according to

$$r(i) = r(i-1) + u(i-1) \quad (20)$$

where $u(i-1)$ is the control. In the sequel, we assume that no dead reckoning sensors are available so that $u(i-1)$ is unknown. The state vector employed in the filter is $x^T(i) = [r^T(i) \ w^T(i) \ c(i)]$. Between measurements, estimates of the conditional mean and error covariance matrix are propagated in the filter using

$$x'(i) = \hat{x}(i-1) ; P'(i) = \hat{P}(i-1) + Q(i-1) \quad (21)$$

where the prime (caret) denotes an estimate just prior to (just after) measurement updating,

$$P'(i) = E\{(x'(i) - x(i))(x'(i) - x(i))^T\},$$

$$\hat{P}(i) = E\{(\hat{x}(i) - x(i))(\hat{x}(i) - x(i))^T\},$$

and $Q(i-1) > 0$ is used in the filter to model the uncertainty associated with the unknown control $u(i-1)$.

From (16), the indirect path length measurements are modeled as

$$y_m(i) = h(x(i)) + n(i) \quad (22)$$

where $n(i)$ is zero-mean Gaussian measurement error.

Updating at a measurement is performed using the extended Kalman filter update equations (cf., Reference [11])

$$\hat{x}(i) = x'(i) + K(i)v_m(i), \hat{P}(i) = [I - K(i)]P'(i) \quad (23)$$

where

$$v_m(i) = y_m(i) - w^T(i)r'(i) - c'(i)$$

is the measurement residual and $K(i)$ is the optimal gain matrix:

$$K(i) = P'(i)H^T(i)/[H^T(i)P'(i)H^T(i) + \sigma_n^2(i)] \quad (24)$$

where

$$H'(i) = \left. \frac{\partial h}{\partial x} \right|_{x=x'(i)} = [w'^T(i) \ r'^T(i) \ 1]$$

and $\sigma_n(i)$ is the rms measurement error.

In case the parameters are assumed to be completely unknown initially, it is necessary to initialize the parameter estimates and the associated error covariance matrix using the first several measurements. This is accomplished using the information form of the Kalman filter.^[12] Let α denote the parameter vector: $\alpha^T(i) = [w^T(i) \ c(i)]$ and write the measurement equation as

$$y_m(i) = g^T(i)\alpha(i) + n(i); \quad g^T(i) = [r^T(i) \ 1] \quad (25)$$

Assume that the first k measurements are direct path measurements resulting in accurate estimates of tag position and let

$$\hat{P}_{\alpha\alpha}(i) = E\{(\hat{\alpha}(i) - \alpha(i))(\hat{\alpha}(i) - \alpha(i))^T\}.$$

Then, using the recursion,

$$\Lambda(i) = \Lambda(i-1) + \hat{g}(i)\hat{g}^T(i); \quad \Lambda(0) = 0 \quad (26)$$

$$\lambda(i) = \lambda(i-1) + \hat{g}(i)y_m(i); \quad \lambda(0) = 0 \quad (27)$$

the initialization is:

$$\hat{P}_{\alpha\alpha}(k) = \Lambda^{-1}(k); \quad \hat{\alpha}(k) = \Lambda^{-1}(k)\lambda(k) \quad (28)$$

Direct path measurements are processed using the extended Kalman filter equations with $x = r$, $h(x) = \|r-s\|$, $H' = \text{unit}(r'-s)^T$.

Estimates of the multipath parameters and covariances are unchanged.

Example

A relatively simple two-dimensional example is presented here to demonstrate the potential effectiveness of the proposed approach. The performance of two filters was compared: 1) the multipath filter, and 2) a conventional extended Kalman filter, which operates on direct path measurements only. A single RF transponding tag is moving within a 30 x 30-m area with planar walls. The initial conditions are shown in Figure 5. Two fixed RF nodes at known locations are located at adjacent corners of the space. It is assumed that the signal attenuation associated with a reflection is large enough to preclude detection of signals resulting from more than one reflection. Multipath signals are thus created by a single specular reflection off either a side (East/West) wall or the South wall. A single 5 x 10-m rectangular object is located within the room, which blocks all RF signals. The geometry in Figure 5 shows the direct paths (solid black lines) and the indirect paths (dotted black lines) to the transponding tag from the two nodes. The two direct paths are unblocked. The two indirect paths resulting from reflection off the East and West walls are also unblocked; however, the two indirect paths resulting from reflection off the South wall are blocked.

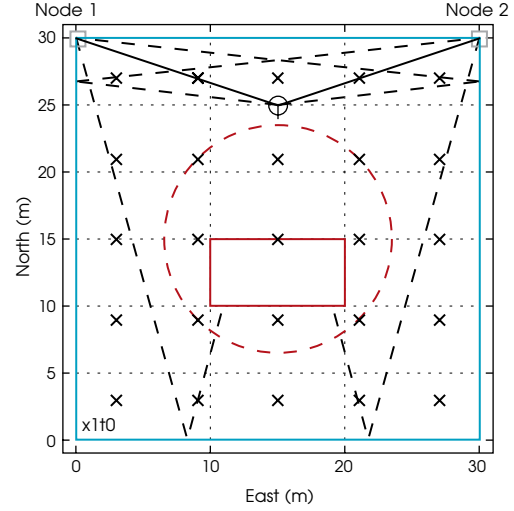


Figure 5. Example: initial conditions.

A particle filter was used initially to reduce the geolocation uncertainty to within the linearization region of an extended Kalman filter. A total of 25 particles was assumed, with the particles initially distributed uniformly within the room (black “x” in Figure 5). The initial 1-sigma error ellipse is shown by the dotted red circle. Initialization was accomplished by sequential processing of one direct path measurement from each of the two nodes (solid black lines) at the initial time. A standard sequential importance sampling algorithm^[10] was used, with the normalized importance weights proportional to the measurement likelihood function. The rms measurement error was $\sigma_n = 1$ ft. Since there were relatively few particles and the measurement error was much smaller than the initial position uncertainty, the first particle filter update yielded only two unique particle locations (population = 10 and 15), an example of the well-known problem of particle impoverishment. A simple spreading algorithm was used to increase particle diversity. The particles at each location were spread by sampling from a Gaussian distribution with an rms value of 1.5 m/axis. The same process was followed after updating using the measurement from Node 2.

The results of the initialization procedure are shown in Figure 6. Both filters were initialized with the same estimates. The particle mean was used to initialize the tag position estimates to

$$\hat{r}(1) = \begin{bmatrix} \hat{r}_1(1) \\ \hat{r}_2(1) \end{bmatrix} = \begin{bmatrix} 27.053 \\ 15.010 \end{bmatrix} \begin{matrix} \text{North} \\ \text{East} \end{matrix}$$

meters, while the tag position error covariance matrices were initialized to $P(1) = 0.09 \ I_2$ meter², in agreement with the assumed rms measurement error. The maximum dispersion of any particle from the true tag location was 5.7 m, so that the dispersion of the particles was reduced to the point where initialization of the extended Kalman filter could be performed.

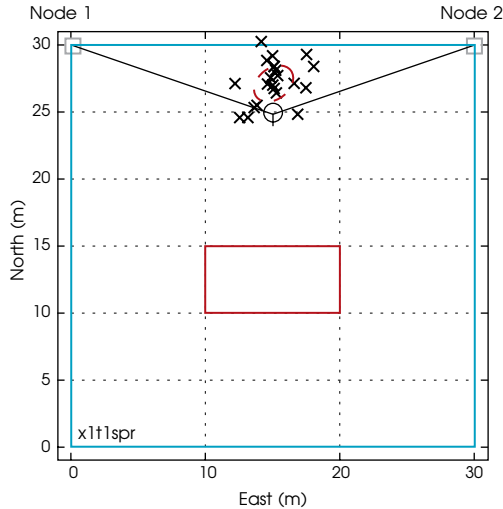


Figure 6. Conditions after particle filter initialization.

Available measurements were processed every 0.5 s. Tag speed was held constant at 0.5 m/s. No dead reckoning sensors were employed, so that the geolocation estimates calculated by both filters were not propagated between measurements; however, the error covariance matrices were increased within both filters using (21). The process noise covariance matrix $Q(i) = v(i)I$ was calculated using sequential differencing of the position estimates to estimate the variance $v(i)$.

The simulation was run for 94 s at a time step of 0.5 s. The time delay (in meters) for the direct and indirect paths are plotted in Figure 7. The two indirect paths from Node 1 have a single crossover point at 20 s. The two indirect paths from Node 2 have a single crossover point at 70 s, with a near-crossover at 17 s. The data association algorithm given in the previous section was employed using quadratic regression models and produced no data association errors.

The true and estimated paths over time for both filters are shown in Figure 8. True tag location is shown by the solid black line. The estimated path for the multipath filter (MP) is shown by the solid colored line, while the estimated path for the conventional filter (CV) is shown by the dotted colored line. While both direct paths are detected (for the first 55 s), the MP filter and the CV filter produce identical geolocation estimates (blue line). After the direct path from Node 2 is lost at 55.5 s, the CV filter is able to navigate off the direct path from Node 1 only, while the MP filter, in addition, is able to navigate off the indirect path from Node 1 reflected off the bottom wall and the indirect path from Node 2 reflected off the West wall. The MP filter estimate (solid red line) produces very small tracking errors, while the CV filter errors (dotted silver line) start to grow. When both direct paths become undetected at 73.5 s, the CV filter can no longer track at all; its geolocation estimate remains constant for the remainder of the simulation. In comparison, the MP filter is able to navigate off the

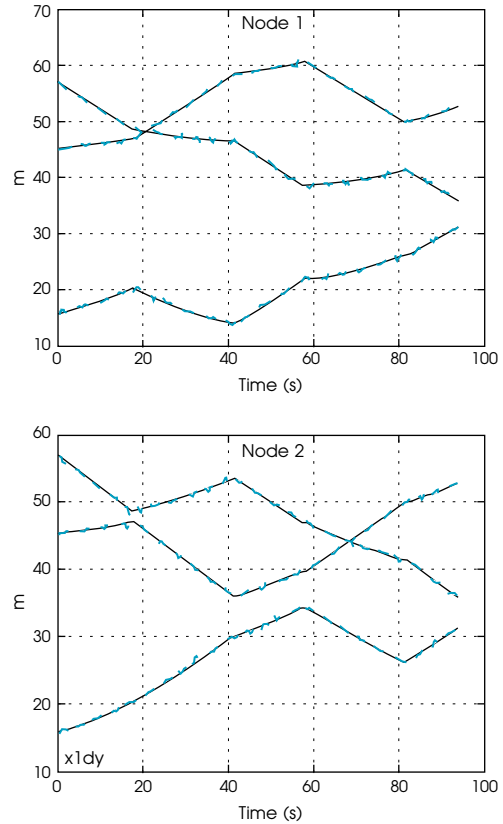


Figure 7. Measurement delay vs. time.

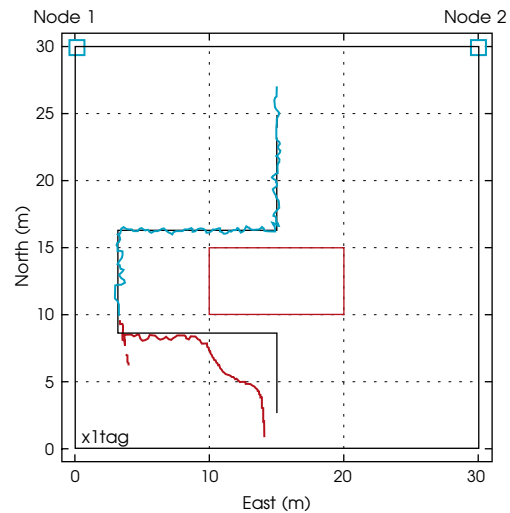


Figure 8. Comparison of true and estimated paths.

detected indirect paths. Between 73.5 and 77.5 s, the MP filter navigates off the indirect path from Node 1 reflected off the bottom wall and both indirect paths from Node 2. At 78 s, the indirect path from Node 2 reflected from the West wall becomes undetected, and the MP filter is reduced to using both indirect path measurements off the bottom wall. At 84 s, all four indirect paths become detectable and are used by the MP filter until the end of the simulation.

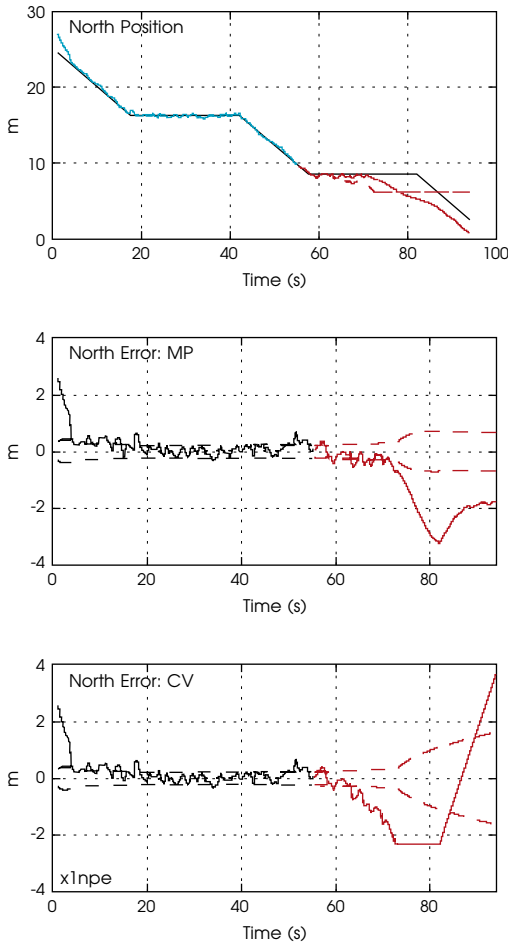


Figure 9. North position tracking performance comparison.

Figures 9 and 10 compare the tracking performance for the two filters along North and East. Position estimate histories are shown in the top panel. Solid lines show MP estimates, while dotted lines show CV estimates; red lines begin at 55.5 s, when the direct path from Node z is lost. The middle panel displays the error histories for MP, while the bottom panel displays the error histories for the CV. True errors are indicated by solid lines and filter-derived 1σ error bounds are shown in dotted lines. The red lines indicate the performance after the direct path from Node 2 is lost at 55.5 s. The ability of MP to recover over the last 10 s, after all four indirect paths are detected, is clearly shown. In comparison, CV cannot use the indirect path measurements and its geolocation errors continue to diverge.

Multipath parameter estimation performance is shown in Figure 11 for the two indirect paths associated with Node 1 and in Figure 12 for the two indirect paths associated with Node 2. In this two-dimensional example, the multipath parameters are the angle $\psi(i) = \arctan(x_1(i)/x_2(i))$ (four quadrant) and the offset parameter $c(i)$. In the figures, the solid black lines denote the true parameter values. The blue lines denote the estimates during periods of time

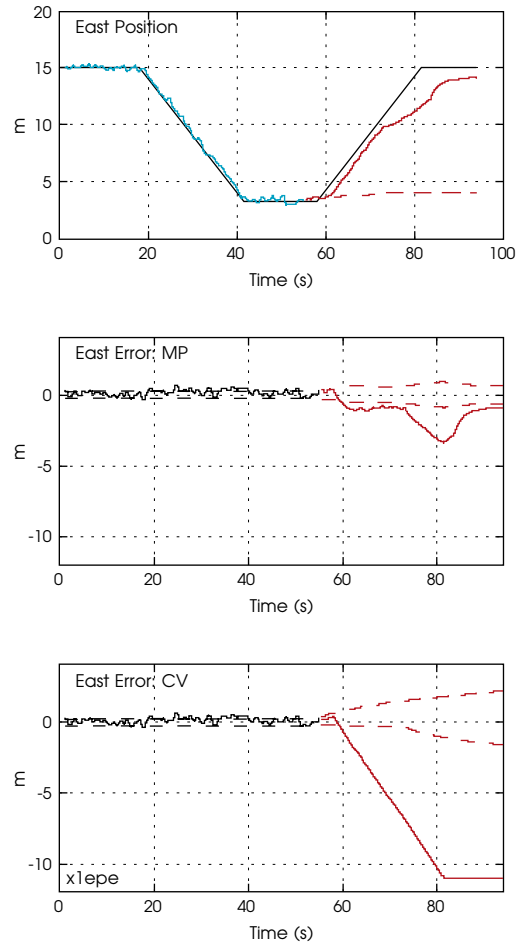


Figure 10. North position tracking performance comparison.

when the multipath parameters are being estimated (direct and indirect path measurements are available simultaneously), while the red lines denote the estimates during periods when direct path measurements are unavailable.

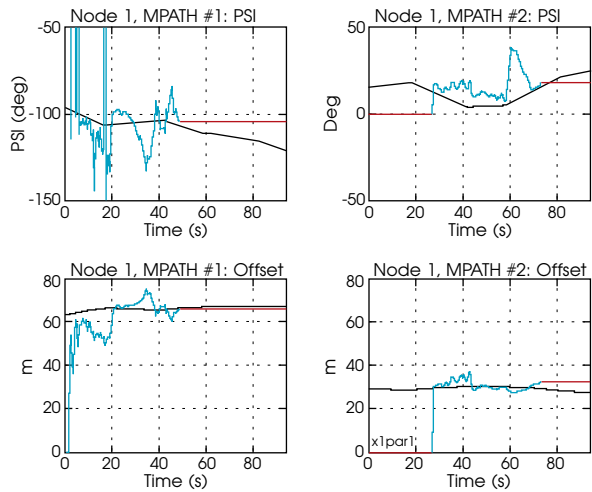


Figure 11. Multipath parameter estimation: Node 1 measurements.

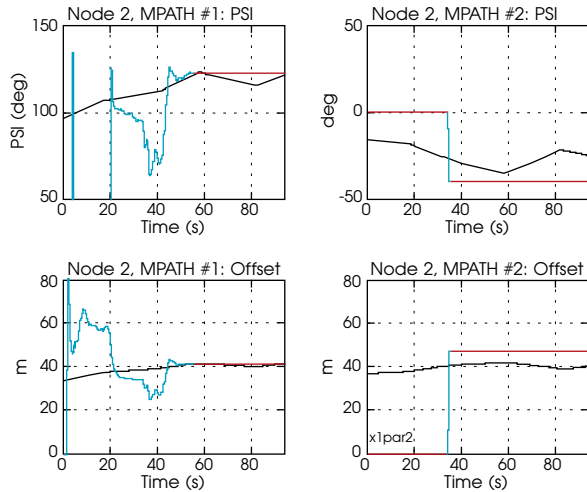


Figure 12. Multipath parameter estimation: Node 2 measurements.

For Node 1, the parameters for the first indirect path (off the West wall) are estimated with reasonable accuracy after 40 s. The parameters for the second path (off the South wall) cannot be estimated for the first 27 s since the indirect path is blocked by the rectangular object. When estimation commences at 27.5 s, the parameters are almost immediately estimated with high accuracy, and this accuracy level continues until the direct path is blocked at 73.5 s.

For Node 2, the parameters for the first indirect path (off the East wall) are estimated with reasonable accuracy after 45 s. The direct path becomes blocked at 55.5 s, so that further updating of the parameter estimates was not possible. The second indirect path (off the South wall) was blocked for the first 34 s. At 34.5 s, the indirect path became unblocked and the indirect path parameters were estimated. At the next time step (35 s), the direct path became blocked and remained blocked for the remainder of the simulation, precluding further estimation of the indirect path parameters. Thus, in this case, the indirect parameter estimates are based on a single measurement pair.

As discussed previously, the variation in the true multipath parameters was relatively small in this representative example, so that relatively accurate tag tracking could be maintained when it was no longer possible to perform parameter estimation.

CONCLUSION

A new approach is suggested for the problem of indoor geolocation in the presence of dominating multipath using RF time-of-arrival measurements. Multipath delays are modeled using a geometry-based argument. Assuming a series of specular reflections off planar surfaces, the model contains a maximum of three unknown multipath parameters per path, which may be estimated in a nonlinear filter. Simulation results for a relatively simple representative example suggest that multipath parameters can be estimated with sufficient accuracy to maintain geolocation accuracy when one or more direct paths are undetected. This approach allows the possibility of building up indoor map information as the geolocation process commences.

REFERENCES

- [1] Pahlavan, K. and X. Li, "Indoor Geolocation Science and Technology," *IEEE Communications Magazine*, February 2002.
- [2] Pahlavan, K., F. Akgul, M. Heidari, and H. Hatami, "Precision Indoor Geolocation in the Absence of Direct Path," submitted to *IEEE Communications Magazine*.
- [3] Moghaddam, P.P., H. Amindavar, R. L. Kirlin, "A New Time-Delay Estimation in Multipath," *IEEE Trans. on Signal Processing*, Vol. 51, No. 5, May 2003, pp. 1129-1142.
- [4] Voltz, P.J. and D. Hernandez, "Maximum Likelihood Time of Arrival Estimation for Real-Time Physical Location Tracking of 802.11a/g Mobile Stations in Indoor Environments," IEEE Paper No. 0-7803-8416-4/04, 2004.
- [5] Qi, Y., H. Suda, H. Kobayashi, "On Time-of-Arrival Positioning in a Multipath Environment," IEEE Paper No. 0-7803-8521-7/04, 2004.
- [6] Giremus, A. and J.-Y. Tournet, "Joint Detection/Estimation of Multipath Effects for the Global Positioning System," *Proc. IEEE ICASSP*, 2005.
- [7] Do, J.-Y., M. Rabinowitz, P. Enge, "Linear Time-of Arrival Estimation in a Multipath Environment by Inverse Correlation Method," *Proc. ION Annual Meeting*, Cambridge, MA, June 2005.
- [8] Erickson, J.W., P.S. Maybeck, J.F. Raquet, "Multipath-Adaptive GPS/INS Receiver," *IEEE Trans. Aero. Elect. Sys.*, Vol. 41, April 2005, pp. 645-657.
- [9] Jourdan, D.B., J.J. Deyst, M.Z. Win, N. Roy, "Monte Carlo Localization in Dense Multipath Environments Using UWB Ranging," *Proc. IEEE International Conference on Ultra-Wideband*, Zurich, September 2005, pp. 314-319.
- [10] Ristic, B., S. Arulampalam, N. Gordon, *Beyond the Kalman Filter*, Chapter 3, Artech House, Boston, 2004.
- [11] Jazwinski, A.H., *Stochastic Processes and Filtering Theory*, Academic Press, New York, 1970.
- [12] Bierman, G.J., *Factorization Methods for Discrete Sequential Estimation*, Academic Press, New York, 1977.

(clockwise from left)
 Donald E. Gustafson,
 John M. Elwell and
 J. Arnold Soltz



Donald E. Gustafson is a Distinguished Member of the Technical Staff at Draper with over 40 years experience in the conceptual design and analysis of guidance, navigation, and control (GN&C) systems. He is one of the principal developers of Draper's Deep Integration system for GPS-based navigation. Currently, he is working on concepts to exploit RF multipath signals in noisy multipath-rich urban and indoor environments for geolocation and mapping. Previously, at MIT Lincoln Laboratory, he worked on target surveillance using antenna arrays. Prior to this, he was co-founder and Vice President of Scientific Systems, Cambridge, MA, where he worked on aircraft failure detection, adaptive control of plastic injection molding machines, biomedical signal processing, meteorological satellite data processing, and financial forecasting. At the MIT Instrumentation Laboratory, he worked on Apollo navigation system design and computerized electrocardiogram interpretation. He was the co-recipient of two Draper Best Technical Publication Awards, two Draper Patent of the Year Awards, and was co-recipient of the 2000 Draper Distinguished Performance Award for the development and demonstration of Draper's GPS/Inertial Navigation System (INS) Deep Integration technique and hardware. He has authored more than 35 technical papers. He holds a PhD in Instrumentation and Automatic Control from the Massachusetts Institute of Technology (MIT) (1973).

John M. Elwell is a Laboratory Technical Staff Member and is currently Tactical System Program Development Manager with 40 years experience developing systems for guidance, precision pointing and tracking, and fire control. Recent activity has been in the area of long-range guided projectiles for electromagnetic railguns and in the exploitation of RF phenomena in urban environments. He is a co-developer of Deep Integration antijam technology for GPS receivers. He has been a member of the Defense Science Board Task Forces on Precision Targeting, Missile Defense, and Modeling and Simulation, and has been presented the SDIO/AIAA Award for contributions to guidance technology. He has authored numerous papers relating to GN&C and has several patents associated with precision pointing and navigation. He holds a BSEE from Northeastern University, an MEE from Rensselaer Polytechnic Institute, and an MBA from Canisius College.

J. Arnold Soltz is a Principal Member of the Technical Staff at Draper with over 40 years experience in the design, implementation, and verification of the models of signals, sensors, and systems used for navigation in spacecraft, aircraft, terrestrial surveying, and undersea vehicles. Fielded systems have included the integration of inertial navigation technology with GPS, laser tracking, RF tracking, and sonar. Recent contributions have included design and development of generalized linear covariance analysis software, verification of a model of the indoor RF environment, and the design and verification of a 5-state Kalman filter for removing the effects of the ionosphere on GPS signals. He has two Draper patents and was the co-recipient of two Draper Best Technical Publication Awards. He has a BA from Johns Hopkins University (1964) and an MS from Northeastern University (1969), and is a member of the Institute of Navigation (ION).

Engineering MEMS Resonators with Low Thermoelastic Damping

Amy E. Duwel,¹ Rob N. Candler,² Thomas W. Kenny,² Mathew Varghese¹

Copyright © 2006, IEEE. Published in *IEEE JMEMS*, Vol. 15, No. 6, 2006

abstract

This paper presents two approaches to analyzing and calculating thermoelastic damping in micromechanical resonators. The first approach solves the fully coupled thermomechanical equations that capture the physics of thermoelastic damping in both two and three dimensions (2D and 3D) for arbitrary structures. The second approach uses the eigenvalues and eigenvectors of the uncoupled thermal and mechanical dynamics equations to calculate damping. We demonstrate the use of the latter approach to identify the thermal modes that contribute most to damping, and present an example that illustrates how this information may be used to design devices with higher quality factors. Both approaches are numerically implemented using a finite-element solver (Comsol Multiphysics). We calculate damping in typical micromechanical resonator structures using Comsol Multiphysics and compare the results with experimental data reported in literature for these devices.

NOMENCLATURE

Variable	Physical Definition
E	Young's modulus
α	Coefficient of thermal expansion
T_o	Nominal average temperature (300 K)
ρ	Density of solid
C_{sp}	Specific heat capacity of a solid
C_v	Heat capacity of a solid, $C_v = \rho C_{sp}$
κ	Thermal conductivity of a solid
ω_{mech}	Mechanical resonance frequency
τ_n	Characteristic time constant for thermal mode n
σ	Stress
ϵ	Strain
λ, μ	Elastic Lamé parameters
T	Temperature
S	Entropy
$[u \ v \ w]$	Components of displacement in x,y, and z directions, respectively
$\bar{u} = [u, \ v]$	2D vector of mechanical displacements
U_m	Mechanical mode amplitude
$\bar{\Phi}_m$	Mechanical eigenmode shape function
ω_m	Mechanical resonant frequency for eigenmode m
A_n	Thermal mode amplitude
T_n	Thermal eigenmode shape function
ω_{th}	Characteristic frequency of dominant thermal mode
ΔW	Energy lost from mechanical resonator system
W	Energy stored in mechanical resonator

¹ Draper Laboratory, Cambridge, MA

² Stanford University, Departments of Mechanical and Electrical Engineering, Stanford, CA

INTRODUCTION

Micromechanical resonators are used in a wide variety of applications, including inertial sensing, chemical and biological sensing, acoustic sensing, and microwave transceivers. Despite the distinct design requirements for each of these applications, a ubiquitous resonator performance parameter emerges. This is the resonator's Quality factor (Q), which describes the mechanical energy damping. In all applications, it is important to have design control over this parameter, and in most cases, it is invaluable to minimize the damping. Over the past decade, both experimental and theoretical studies^{[1]-[6],[9],[22]} have highlighted the important role of thermoelastic damping (TED) in micromechanical resonators. However, the tools available to analyze and design around TED in typical micromechanical resonators are limited to analytical calculations that can be applied to relatively simple mechanical structures. These are based on the defining work done by Zener in References [7] and [8].

Zener developed general expressions for thermoelastic damping in vibrating structures, with the specific case study of a beam in its fundamental flexural mode. In Reference [8], Zener's calculation was based on fundamental thermodynamic expressions for stored mechanical energy, work, and thermal energy that used *coupled* thermal-mechanical constitutive relations for stress, strain, entropy, and temperature. However, in order to evaluate these energy expressions for a specific resonator, Zener proposed that the strain and temperature solutions from *uncoupled dynamical equations* could be sufficient. He found the eigensolutions of the mechanical equation, and, separately, the eigensolutions of the uncoupled thermal equation. By applying these to the coupled thermodynamic energies, Zener calculated the thermoelastic Q of an isotropic homogenous resonator to be:

$$Q^{-1} = \left(\frac{E\alpha^2 T_o}{C_v} \right) \sum_n \frac{\omega_{\text{mech}} \tau_n}{1 + (\omega_{\text{mech}} \tau_n)^2} f_n \quad (1)$$

where the physical constants are listed in the Nomenclature, ω_{mech} is the mechanical resonance frequency, and τ_n is the characteristic time constant of a given thermal mode. This takes into account the fact that multiple thermal modes may add to the damping of a single mechanical resonance. The contribution of a given mode, n , is determined by its weighting function, f_n .

Zener explicitly calculated the weighting functions for a simple beam resonating in its fundamental flexural mode. In order to make the analysis tractable, he assumed that only thermal gradients across the beam width (dimension in the direction of the flexing) were significant. This left only a 1D thermal equation to solve. Zener found that a single thermal mode dominated, giving

$$Q^{-1} = \left(\frac{E\alpha^2 T_o}{C_v} \right) \frac{\omega_{\text{mech}} \tau}{1 + \omega_{\text{mech}}^2 \tau^2} \quad (2)$$

Few structures are amenable to the simplifications that led to expression (2) for Q . However, Zener's expression (1) is quite general. In the section "Weakly Coupled Approach to TED Solutions," we show how numerical solutions to the uncoupled mechanical and thermal dynamics of a resonator can be used to evaluate (1). This adds a great deal of power to Zener's approach, since arbitrary geometries can be considered.

We show how Zener's weighting function approach offers an intuition into the details of the energy transfer. At the same time, our results highlight the limits of intuition in identifying the thermal modes of interest. For example, we find that the simplification Zener made in assuming only thermal gradients in one direction along the beam were significant does not capture the most important thermal mode, even for a simple beam. In addition, past efforts to estimate Q without explicitly calculating the weighting functions have been shown^[9] to greatly overestimate the damping behavior of real systems. This "modified" interpretation of Zener's method can be misleading.

In this paper, we describe a method for using full numerical solutions to evaluate Q using Zener's approach. We call this a "weakly coupled" approach. We also present our numerical method for solving the fully coupled thermoelastic dynamics equations to calculate Q for an arbitrary structure. Using numerical solutions in the weakly coupled approach offers powerful guidance in engineering around thermoelastic damping, while fully coupled solutions offer the ability to precisely evaluate and optimize the thermoelastic Q of a resonator.

NUMERICAL SOLUTION OF THE FULLY COUPLED TED EQUATIONS

The coupled equations governing thermoelastic vibrations in a solid are derived in Reference [19]. The following section, "Governing Equations in 3D," outlines the basic principles of this derivation. "Governing Equations in 2D with Plane Stress Approximations" highlights modifications required for a 2D plane stress formulation. The full 2D and 3D equations are written explicitly so that they are accessible to the user community. We numerically solve the 2D and 3D dynamical equations using the finite-elements based package Comsol Multiphysics.^[11] The Comsol implementation is described in References [12] and [13]. This analysis can be applied to the wide variety of microelectromechanical system (MEMS) resonator structures reported in the literature. It is a useful tool for determining whether TED limits performance or whether other damping mechanisms, such as anchor damping,^[23] should be investigated instead. "Quality Factor Calculations for Typical MEMS Resonators" demonstrates the application of TED simulations to a few example MEMS resonator structures. Quality factors are calculated and compared with the analytical Eq. (1) as well as with experimental measurements reported in the literature.

Governing Equations in 3D

The constitutive relations for an isotropic thermoelastic solid, derived from thermodynamic energy functions, are in matrix form

$$\begin{bmatrix} \sigma_1 \\ \sigma_2 \\ \sigma_3 \\ \sigma_4 \\ \sigma_5 \\ \sigma_6 \end{bmatrix} = \begin{bmatrix} \lambda+2\mu & \lambda & \lambda & 0 & 0 & 0 \\ \lambda & \lambda+2\mu & \lambda & 0 & 0 & 0 \\ \lambda & \lambda & \lambda+2\mu & 0 & 0 & 0 \\ 0 & 0 & 0 & \mu & 0 & 0 \\ 0 & 0 & 0 & 0 & \mu & 0 \\ 0 & 0 & 0 & 0 & 0 & \mu \end{bmatrix} \begin{bmatrix} \epsilon_1 \\ \epsilon_2 \\ \epsilon_3 \\ \epsilon_4 \\ \epsilon_5 \\ \epsilon_6 \end{bmatrix} - (3\lambda+2\mu)\mathbb{T} \begin{bmatrix} \alpha \\ \alpha \\ \alpha \\ 0 \\ 0 \\ 0 \end{bmatrix} \quad (3)$$

and

$$S = [\alpha \ \alpha \ \alpha \ 0 \ 0 \ 0] \begin{bmatrix} \lambda+2\mu & \lambda & \lambda & 0 & 0 & 0 \\ \lambda & \lambda+2\mu & \lambda & 0 & 0 & 0 \\ \lambda & \lambda & \lambda+2\mu & 0 & 0 & 0 \\ 0 & 0 & 0 & \mu & 0 & 0 \\ 0 & 0 & 0 & 0 & \mu & 0 \\ 0 & 0 & 0 & 0 & 0 & \mu \end{bmatrix} \begin{bmatrix} \epsilon_1 \\ \epsilon_2 \\ \epsilon_3 \\ \epsilon_4 \\ \epsilon_5 \\ \epsilon_6 \end{bmatrix} + \frac{C_v}{T_0} \mathbb{T} \quad (4)$$

where reduced tensor notation has been used, and the variables are defined in the Nomenclature.

To obtain the coupled dynamics, the constitutive relations are applied to the force balance constraints and Fourier's law of heat transfer. Force balance in the x direction gives

$$\rho \frac{\partial^2 u}{\partial t^2} = \left(\frac{\partial \sigma_1}{\partial x} + \frac{\partial \sigma_5}{\partial y} + \frac{\partial \sigma_6}{\partial z} \right) \quad (5)$$

with similar relations for the y and z directions.

Substituting displacement for strain and simplifying, the 3D equations of motion become

$$\rho \frac{\partial^2 u}{\partial t^2} = \mu \left(\frac{\partial^2 u}{\partial x^2} + \frac{\partial^2 u}{\partial y^2} + \frac{\partial^2 u}{\partial z^2} \right) + (\lambda + \mu) \left(\frac{\partial^2 u}{\partial x^2} + \frac{\partial^2 v}{\partial x \partial y} + \frac{\partial^2 w}{\partial x \partial z} \right) - \alpha(3\lambda + 2\mu) \frac{\partial T}{\partial x} \quad (6)$$

$$\rho \frac{\partial^2 v}{\partial t^2} = \mu \left(\frac{\partial^2 v}{\partial x^2} + \frac{\partial^2 v}{\partial y^2} + \frac{\partial^2 v}{\partial z^2} \right) + (\lambda + \mu) \left(\frac{\partial^2 u}{\partial y \partial x} + \frac{\partial^2 v}{\partial y^2} + \frac{\partial^2 w}{\partial y \partial z} \right) - \alpha(3\lambda + 2\mu) \frac{\partial T}{\partial y} \quad (7)$$

$$\rho \frac{\partial^2 w}{\partial t^2} = \mu \left(\frac{\partial^2 w}{\partial x^2} + \frac{\partial^2 w}{\partial y^2} + \frac{\partial^2 w}{\partial z^2} \right) + (\lambda + \mu) \left(\frac{\partial^2 u}{\partial z \partial x} + \frac{\partial^2 v}{\partial z \partial y} + \frac{\partial^2 w}{\partial z^2} \right) - \alpha(3\lambda + 2\mu) \frac{\partial T}{\partial z} \quad (8)$$

To obtain the thermal dynamics, we apply Fourier's law

$$\mathbb{T} \dot{S} = \kappa \nabla^2 T \quad (9)$$

The constitutive relations are applied, and the resulting equation is linearized around T_0 , the ambient temperature, to give, in 3D

$$\kappa \nabla^2 T - C_v \dot{T} - \alpha(3\lambda + 2\mu) T_0 \left(\frac{\partial \dot{u}}{\partial x} + \frac{\partial \dot{v}}{\partial y} + \frac{\partial \dot{w}}{\partial z} \right) = 0 \quad (10)$$

In summary, Eqs. (6)-(8) and (10) form a set of coupled linear equations in 3D. Since the equations are linear, we can use a finite-elements-based approach to solving them on an arbitrary geometry. We solve for the unforced eigenmodes. The generalized eigenvectors contain u , v , w , and T at every node. The eigenvalues, ω_i , are complex. The imaginary component represents the mechanical vibration frequency, while the real part provides the rate of decay for an unforced vibration due to the thermal coupling. The quality factor of the resonator is defined as

$$Q_i = \text{Im}\{\omega_i\} / 2 \text{Re}\{\omega_i\} \quad (11)$$

Governing Equations in 2D with Plane Stress

Approximations

For long beams in flexural vibrations, we can identify one axis (we chose to be z) in which all strains are uniform and no loads are applied. For clarity, we define the x axis along the beam length and the y axis in the direction of flexing. Along the z direction σ_3 , σ_4 , and σ_5 must be zero throughout the structure. This is essentially a plane stress approximation. When $\sigma_3 = 0$ is applied to Eq. (3) above, we find that

$$\epsilon_3 = -\frac{\lambda}{\lambda + 2\mu} (\epsilon_1 + \epsilon_2) + \alpha \left(\frac{3\lambda + 2\mu}{\lambda + 2\mu} \right) T \quad (12)$$

In the plane stress approximation, the force balance relation (5) is

$$\rho \frac{\partial^2 u}{\partial t^2} = \left(\frac{\partial \sigma_1}{\partial x} + \frac{\partial \sigma_6}{\partial y} \right) \quad (13)$$

Expanding the stress terms using the constitutive relations

$$\rho \frac{\partial^2 u}{\partial t^2} = \lambda \frac{\partial}{\partial x} (\epsilon_1 + \epsilon_2 + \epsilon_3) + 2\mu \frac{\partial}{\partial x} \epsilon_1 + \mu \frac{\partial}{\partial y} \epsilon_6 - \alpha(3\lambda + 2\mu) \frac{\partial T}{\partial x} \quad (14)$$

Applying (12) to (14), the equations of motion become

$$\rho \frac{\partial^2 u}{\partial t^2} = \mu \left(\frac{\partial^2 u}{\partial x^2} + \frac{\partial^2 u}{\partial y^2} \right) + \left(\frac{2\mu^2 + 3\lambda}{\lambda + 2\mu} \right) \frac{\partial^2 u}{\partial x^2} + \left(\frac{2\mu\lambda}{\lambda + 2\mu} \right) \frac{\partial^2 v}{\partial x \partial y} + \mu \frac{\partial^2 v}{\partial y \partial x} - 2\alpha\mu \frac{(3\lambda + 2\mu)}{\lambda + 2\mu} \frac{\partial T}{\partial x} \quad (15)$$

$$\rho \frac{\partial^2 v}{\partial t^2} = \mu \left(\frac{\partial^2 v}{\partial x^2} + \frac{\partial^2 v}{\partial y^2} \right) + \left(\frac{2\mu^2 + 3\lambda}{\lambda + 2\mu} \right) \frac{\partial^2 v}{\partial y^2} + \left(\frac{2\mu\lambda}{\lambda + 2\mu} \right) \frac{\partial^2 u}{\partial y \partial x} + \mu \frac{\partial^2 u}{\partial x \partial y} - 2\alpha\mu \frac{(3\lambda + 2\mu)}{\lambda + 2\mu} \frac{\partial T}{\partial y} \quad (16)$$

The linearized temperature equation is

$$\kappa \nabla^2 T - C_v \dot{T} - \alpha(3\lambda + 2\mu) T_0 (\dot{\epsilon}_1 + \dot{\epsilon}_2 + \dot{\epsilon}_3) = 0 \quad (17)$$

We apply Eq. (12) and also neglect z -directed temperature gradients to obtain

$$\kappa \left(\frac{\partial^2}{\partial x^2} T + \frac{\partial^2}{\partial y^2} T \right) - \left(C_v + \alpha^2 \frac{(3\lambda + 2\mu)^2}{\lambda + 2\mu} T_0 \right) \dot{T} - 2\alpha\mu \frac{(3\lambda + 2\mu)}{\lambda + 2\mu} T_0 \left(\frac{\partial \dot{u}}{\partial x} + \frac{\partial \dot{v}}{\partial y} \right) = 0 \quad (18)$$

In summary, Eqs. (15)-(16) and (18) form a set of coupled linear equations in 2D. In order to find Q, we solve for the unforced eigenmodes. The generalized eigenvectors contain u, v, and T at every node.

Quality Factor Calculations for Typical MEMS Resonators

The thermoelastic Q values for several example MEMS resonators have been calculated. Table 1 introduces the resonator structures and the material parameters used. In Table 2, we summarize the simulated Q values for the various structures. We compare simulated results to calculations based on Eq. (2) where applicable. We also compare to data reported in the literature. In some cases, the experimental data appear to have achieved the thermoelastic limit. For these devices, it is clear that structural modifications that





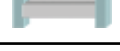
can engineer a higher thermoelastic limit are warranted. In devices where the measured Q value is less than half the thermoelastic limit, investigation into and minimization of other damping mechanisms is warranted.

A polysilicon beam resonating in its fundamental flexural mode was simulated and compared to measurements.^[9] In the experiments, the beam was actually part of a doubly clamped tuning fork to minimize anchor damping. For a resonator operating at 0.57 MHz, the measured Q equaled 10,281. Zener's formula, Eq. (2), predicts Q = 10,300, for the beam at 0.57 MHz and with $\tau = a^2/\pi^2 D_{th}$ ($a = 12\text{-}\mu\text{m}$ beamwidth in the direction of flexural motion, and $D_{th} = \kappa/\rho C_{sp}$). The simulations used only a single clamped beam with dimensions matching the beam of the tuning fork. The simulated frequency was 0.63 MHz and the simulated TED Q = 10,211. This remarkable correlation between simulation results and experiments suggests that the flexural beam Q is limited by thermoelastic damping. Higher thermoelastic Q might be achieved by geometry modifications as explored in Reference [9] or by fabricating a given structure from different materials as explored in Reference [6].

Table 1. Summary of Parameters Used in Q Simulation and Calculations for a Longitudinal Resonator.

Resonator	Units	Flexural (2D)	Longitudinal (2D)	Longitudinal (3D)	Torsional (3D)	Flexural with Slit (3D)
Material		Polysilicon	Silicon	Si _{0.35} Ge _{0.65}	Silicon	Polysilicon
Material Property References		Ref. [9]		Refs. [14], [24]		Ref. [9]
Critical Dimensions	μm	400 x 12 x 20	290 x 10 x 10	32 x 40 x 2.2	5.5 x 2 x 0.2	150 x 3.5 x 35
Young's Modulus	GPa	157	180	155	180	157
Density	kg/m ³	2330	2330	4810	2330	2330
Specific Heat	J/kg • K	700	700	377	700	700
Thermal Conductivity	W/m • K	90	130	59	130	90
Thermal Expansion Coeff.	ppm/K	2.6	2.6	4.3	2.6	2.6

Table 2. Summary of Simulated Q Values for a Selection of MEMS Resonators. Simulation Results Are Compared with Calculations Based on Zener's Single-Mode Approximation and Measured Results Reported in the Literature.

Resonator	Simulated Frequency	Measured Frequency	Simulated Q	Analytical Q	Measured Q	Experimental Reference
Fixed-fixed beam 2D 	0.63 MHz	0.57 MHz	10,300	10,300	10,281	Reference [9]
Longitudinal 2D 	15.3 MHz	14.7 MHz	1,650,000	N/A	170,000	Reference [20]
Longitudinal 3D 	70.5 MHz	74.4 MHz	366,000	N/A	2863	Reference [15]
Torsional 3D 	4.4 MHz	5.6 MHz	2E8	N/A	3300	Reference [16]
Fixed-fixed beam 2D 	1.27 MHz	1.15 MHz	26,000	N/A	5600	Reference [21]

A $\text{Si}_{0.35}\text{Ge}_{0.65}$ capacitively-actuated, longitudinal mode resonator was modeled and simulated based on geometry information provided in Reference [15] and material properties reported in References [14], [24]. $4\ \mu\text{m} \times 4\ \mu\text{m}$ anchors were included in the simulation, with fixed boundary conditions at the ends of the anchors. Quévy et al. report the Q measurement of 2863 for the fundamental longitudinal mode of a bar resonator. Equation (2) was not applied to calculate the analytical Q, since the derivation was for flexural modes only. We find that the TED Q is two orders higher than the measured Q. This suggests that thermoelastic damping, for the fundamental longitudinal mode, is not a significant contributor to the overall energy loss in this resonator. Other mechanisms, such as anchor damping, are being optimized by this group with tangible impact on Q being reported.^[25]

A second longitudinal resonator was also simulated. The device described in Reference [20] is single-crystal silicon, and its resonance length of $290\ \mu\text{m}$ far exceeds its other dimensions. This resonator is also capacitively actuated and operates at 14.7 MHz. The measured Q is 170,000, while the simulated thermoelastic Q is an order of magnitude larger. This device also does not appear to be thermoelastically limited.

A paddle resonator operating in its torsional resonance was simulated. The simulation model was based on the nonmetalized silicon-on-insulator (SOI) device described in Reference [16]. Fixed-fixed boundary conditions were applied to the ends of the tethers. The simulated resonant frequency was about 20% lower than the measured torsional frequency. The value of Young's modulus used in the simulations was on the high end of values reported in Reference [17], so is unlikely to explain the discrepancy. Analytical calculation of the torsional frequency using Reference [18] given a total torsional stiffness of $9.4 \times 10^{-12}\ \text{N} \cdot \text{m}/\text{rad}$ for the beams, and a second moment of inertia of $1.3 \times 10^{-26}\ \text{kg} \cdot \text{m}^2$ for the plate yields 4.3 MHz, within 3% of the simulated result. The discrepancy between the measured frequency and the theoretical frequencies may be the result of fabrication-induced variations in the sample dimensions. Evoy et al. reported experimental Q values in the range of 3300 for room temperature measurements, while the simulations predict thermoelastic Q values of 200 million. The simulated result is consistent with the physical understanding that torsional deformations produce little or no volumetric expansion and should therefore have negligible thermoelastic damping.

Finally, the flexural mode polysilicon beam with a center opening described in Reference [21] was simulated. The case with a beam length of $150\ \mu\text{m}$ and width of $3.5\ \mu\text{m}$ was considered. Since the material parameters of the device were not available, we used the polysilicon values of Reference [9]. Although the center opening dimensions were not provided, the scanning electron microscope (SEM) indicated that the slit was extremely narrow. Using Comsol

Multiphysics, the narrowest slit we were able to model was $0.1\ \mu\text{m}$ wide, centered in the $3.5\text{-}\mu\text{m}$ beamwidth. The slit was also centered in the $35\text{-}\mu\text{m}$ beam height, spaced $2\ \mu\text{m}$ from top and bottom. The measured Q was 5600, while the simulated TED-limited Q was 26,000. This simulated Q dropped to 25,000 for a solid polysilicon beam at the same frequency. We also simulated a wider slit and found that the Q went up to 26,200 for a slit $0.35\ \mu\text{m}$ wide. This suggests that at this frequency, the polysilicon beam has a TED-limited Q that starts at 25,000 and can be increased with an increasingly wider slit. The experimental reference may have had a narrower slit than we were able to model, but the simulations were useful in bounding the TED-limited Q between approximately 25,000-26,000 and in identifying the trend. The TED Q is about 4.5 times higher than the experimentally measured Q. Though the device does not appear to be TED limited, thermoelastic damping is clearly important in this device and can still be optimized.

Weakly Coupled Approach to TED Solutions

Thermoelastic damping in MEMS resonators can also be calculated via a weakly coupled approach proposed by Zener. This approach uses eigenvalue solutions to the uncoupled mechanical and thermal equations.^[8] We show how to numerically implement Zener's approach so that structures more complicated than a solid beam can be studied. While the fully coupled numerical analysis presented in the previous section is much more accurate, we emphasize that Zener's approach can offer design insights that might not otherwise be possible. The next four sections describe the analysis. For simplicity, the formulas in this section are written for the 2D case and use vector notations, with

$$\bar{\mathbf{u}} = \begin{bmatrix} \mathbf{u} \\ \mathbf{v} \end{bmatrix}$$

where \mathbf{u} and \mathbf{v} are the displacements in the x and y directions, respectively.

In the next section, "Modal Solutions to Thermal and Mechanical Systems," we introduce time-harmonic modal expansions for the mechanical and thermal domain solutions. Both the thermal modes and the mechanical modes of a given structure can be found numerically by eigenvalue analysis, assuming no thermoelastic coupling. This section also shows how to calculate the relative thermal mode amplitudes that are driven by the one mechanical mode. The two sections that follow introduce two expressions for the energy loss per cycle. In "Energy Lost from Mechanical Domain," the mechanical energy loss as a function of mechanical and thermal modes is derived. By energy conservation, this is equal to the energy transferred to the thermal domain. In "Energy Transferred to Thermal Domain," the energy coupled into the thermal domain is taken directly from Reference [8], where the net heat rise is derived in terms of the entropy generated per cycle. The expressions for energy lost per cycle in these

two sections can be evaluated directly from the modal solutions obtained numerically. Although it is not obvious on inspection that the two expressions are algebraically identical, energy conservation requires that they are equal. We have validated this numerically for isotropic solids, and Reference [8] provides an algebraic proof for solids with cubic symmetry.

In “Using Weighting Functions to Optimize a UHF Beam Resonator,” we apply the weakly coupled formulation to the cases of a solid beam and two versions of a slotted beam. We describe insights gained by studying the modes obtained in the weakly coupled approach. In each example, we compare the Q value found with the Q calculated through a fully coupled analysis. A thorough experimental study of the slotted beam is referenced,^[9] where TED calculations are compared with experimental measurements over a wide range of frequencies.

Modal Solutions to Thermal and Mechanical Systems

Zener first identified the mechanical resonant mode of interest and assumed a sinusoidal steady state of the form

$$\bar{u}(x, y, t) = \text{Re}(U_m \bar{\Phi}_m(x, y) e^{j\omega_m t}) \quad (19)$$

This is the m^{th} eigensolution to the vector version of Eqs. (15)-(16), without the thermal coupling term. $\bar{\Phi}(x, y)$ is a real valued modal shape function, U_m is the mode amplitude, and ω_m is the mechanical resonant frequency. Note that the shape functions and frequencies can be found numerically using either Comsol Multiphysics or another commercially-available software package.

Spatial variations of strain caused by the mechanical vibration generate thermal gradients that are captured by the driven thermal equation

$$\kappa \nabla^2 T - C_v \dot{T} = \theta_c T_o \nabla \cdot \dot{\bar{u}} \quad (20)$$

where θ_c captures the combination of constants written explicitly in Eq. (17), and where the term of order α^2 is neglected. For simplicity, we also limit our study to one mechanical mode at a time, $\bar{\Phi}_{\text{mech}}$ and ω_{mech}

$$\kappa \nabla^2 T - C_v \dot{T} = \theta_c T_o \nabla \cdot \dot{\bar{\Phi}}_{\text{mech}} (U_{\text{mech}} j\omega_{\text{mech}} e^{j\omega_{\text{mech}} t}) \quad (21)$$

This equation is solved as a function of the mechanical resonance amplitude, U_{mech} . Applying separation of variables, the response to a drive at frequency ω_{mech} is

$$T(x, y, t) = T_o + \text{Re} \left(\sum_n A_n T_n(x, y) e^{j\omega_{\text{mech}} t} \right) \quad (22)$$

The functions $T_n(x, y)$ are the real-valued spatial eigenmodes of the undriven thermal equation and A_n are the complex modal amplitudes. To find the modal amplitudes, we apply the orthogonality of the eigenmodes $T_n(x, y)$. The expansion (22) is substituted into (21). Multiplying equation (21) by T_1 and integrating over the volume, we obtain

$$A_n = \frac{j\omega_{\text{mech}} U_{\text{mech}} \theta_c T_o}{\kappa_n - j\omega_{\text{mech}} C_n} \int_V \nabla \cdot \bar{\Phi}_{\text{mech}} T_n dV \quad (23)$$

with

$$\kappa_n = \int_V T_n \kappa \nabla^2 T_n dV \quad (24)$$

$$C_n = \int_V T_n C_v T_n dV \quad (25)$$

The absolute magnitude of $|A_n/U_{\text{mech}}|$ from Eq. (23) can be used to assess the effective coupling of mechanical modes into the thermal domain.

To calculate the mechanical quality factor, we first have to calculate the energy lost by the mechanical system per radian, or equivalently, the energy gained by the thermal system per radian.

Energy Lost from Mechanical Domain

The energy lost from the mechanical domain per radian is

$$\Delta W = \frac{1}{2\pi} \oint \left[\int \left(\sigma_1 \frac{d\varepsilon_1}{dt} + \sigma_2 \frac{d\varepsilon_2}{dt} + \sigma_6 \frac{d\varepsilon_6}{dt} \right) dV \right] dt \quad (26)$$

in 2D, where $\sigma_3 = \sigma_4 = \sigma_5 = 0$. Stress in the above equation is expanded as a function of strain and temperature using Eq. (3). The strain is expressed in terms of the modal amplitude and shape function. This expansion is further simplified by recognizing that only the temperature-dependent terms produce nonzero integrals over one cycle. Integration over time yields

$$\Delta W = \sum_n \Delta W_n = \sum_n \frac{1}{2} \int_V \left[\theta_c \text{Im}(A_n) T_n \right] \left[U_{\text{mech}} \nabla \cdot \bar{\Phi}_{\text{mech}} \right] dV \quad (27)$$

where each term in this sum, ΔW_n , corresponds to the energy dissipated by the n^{th} thermal mode. The thermal component of stress that is out of phase with the strain damps the vibration, and this term may be identified in the first bracket in Eq. (27). The second bracket is the strain.

Energy Transferred to Thermal Domain

The expression for energy gained by the thermal domain per cycle is derived in Reference [8] to be

$$\Delta W = \frac{T_o}{2\pi} \oint \left[\int (T^{-1} \kappa \nabla^2 T) dV \right] dt \quad (28)$$

The T^{-1} term is replaced by its Taylor expansion, $1/T_o - T/T_o^2$, where it is assumed that the driven modal amplitudes are small relative to the ambient temperature. Only the latter term in this expansion produces a nonzero integral over one cycle, so that

$$\Delta W \approx \frac{1}{2\pi} \oint \left[\int \left(\frac{T}{T_o} \kappa \nabla^2 T \right) dV \right] dt \quad (29)$$

Where κ is the thermal conductivity in Joules/(Kelvin-second-meter). Expanding T using (22) and (23), it may be shown that Eq. (29) reduces to

$$\Delta W = \sum_n \Delta W_n = \sum_n \frac{1}{2} \frac{|A_n|^2}{\omega_{\text{mech}} T_0} \kappa_n \quad (30)$$

Weakly Coupled Quality Factor Calculation

The maximum stored energy in the 2D mechanical system is given by

$$W = \frac{1}{2} \int_V (\sigma_1 \varepsilon_1 + \sigma_2 \varepsilon_2 + \sigma_6 \varepsilon_6) dV \quad (31)$$

where the integral is evaluated at the maximum mechanical amplitude. This integral may be evaluated directly for a given mode shape by substituting Eq. (3) for stress with the appropriate 2D approximations ($\sigma_3 = \sigma_4 = \sigma_5 = 0$). The Q of the device is then calculated by

$$Q^{-1} = \sum_n Q_n^{-1} = \sum_n \frac{\Delta W}{W} \quad (32)$$

where Q_n is an effective Q corresponding to the n^{th} thermal mode. In applying Eq. (32) to calculate Q , ΔW can be found from either Eq. (27), the expression for mechanical energy lost, or Eq. (30), the thermal energy gained. These expressions can be shown to be equivalent.

This analysis shows that we can use numerically calculated modal solutions of uncoupled thermal and mechanical equations to calculate the Q . For simplicity, we restricted our analysis to a single mechanical mode of interest. We considered that possibly many thermal modes would contribute to damping in the system. The individual terms in the sum Eq. (32) for Q can be used to identify the thermal modes that contribute most to damping and evaluate their relative weights.

Using Weighting Functions to Optimize a UHF Beam Resonator

Figure 1 shows the calculated Q values for a range of thermal modes in a beam. The beam is assumed to be in its fundamental flexural resonance at frequency 0.63 MHz. The frequency and mode shape were found numerically. The first 40 thermal modes were also found numerically. Using the approach described in the previous four sections, we evaluated the thermoelastic damping associated with each mode. The Comsol Multiphysics module was used to evaluate the overlap integrals in $|A_n|$ (Eq. (23)) that are needed to evaluate ΔW in Eq. (27) or (30). The total Q , based on 40 modes in Eq. (32), was found to be 10,400. The Q calculated in a full TED simulation as described in ‘‘Governing Equations in 2D with Plane Stress Approximations’’ was 10,200. The weakly coupled calculations show that this damping is dominated by the contribution of a single mode, whose thermal eigenfunction is shown in the inset. This mode at 0.605 MHz gave $Q = 11,000$. Interestingly, the temperature distribution of this mode is not

uniform along the beam axis. Although Zener’s original approximation assumed that dominant thermal mode had no variation along the beam axis, we find that the uniform mode, also shown in Figure 1, has a high $Q = 6,250,000$.

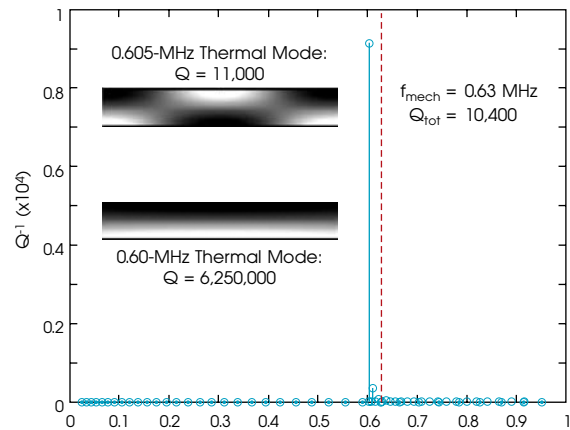


Figure 1. Q values for thermal modes in a fixed-fixed, thermally-insulated beam that is 400 μm long and 12 μm wide. The mechanical resonance is the fundamental flexural mode at 0.63 MHz. The first 40 thermal modes are calculated. The three most heavily damped modes are: at 0.6 MHz with a Q of 6,250,000, at 0.605 MHz with a Q of 11,000, and at 0.611 MHz with a Q of 280,000 (spatial profile not shown in inset). The total device Q , including all 40 thermal modes is 10,400.

After observing the thermal distribution of the dominant thermal mode, we consider the effect of placing slots in the beam. The slots, proposed originally in Reference [9], are designed to alter the dominant thermal mode without significant effect on the fundamental flexural mode frequency. Figure 2 shows the Q_n values for the solid beam from Figure 1 next to the results for a slotted beam. The slots had the effect of modifying the thermal eigensolutions and characteristic frequencies. In the slotted beam, many more thermal modes contribute to the damping of the structure. On the other hand, the thermal modes with the greatest spatial overlap are moved to much higher frequencies, minimizing their overall effect on damping. In this beam, the slots had the effect of raising the total Q value by a significant factor of four.

If the mechanical mode frequency were already much higher than the dominant thermal mode, then moving the dominant modes up in frequency could have a detrimental effect on Q . This case is shown in Figure 3. Originally, in the solid beam, the mechanical frequency is at 4.327 MHz, while the dominant thermal mode is still at 0.605 MHz. When slots are added to this beam, thermal modes with significant spatial overlap move up in frequency, much nearer to the mechanical resonance. This lowers the Q to 20,200 from 38,000 without slots.

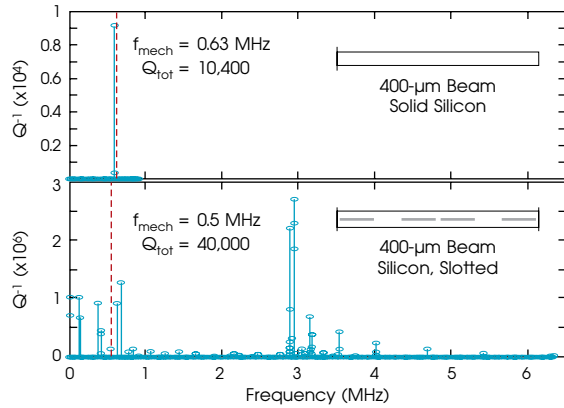


Figure 2. Q values for thermal modes in a fixed-fixed, thermally-insulated beam that is 400 μm long and 12 μm wide. The top plot shows the solid beam thermal modes and mechanical resonance, while the bottom plot shows the same beam with 1- μm wide slits along the beam length. The effect of the slits on the thermal modes and their Q values indicated. The mechanical resonance shifts slightly, as expected. The total Q value is higher in the beam with slits.

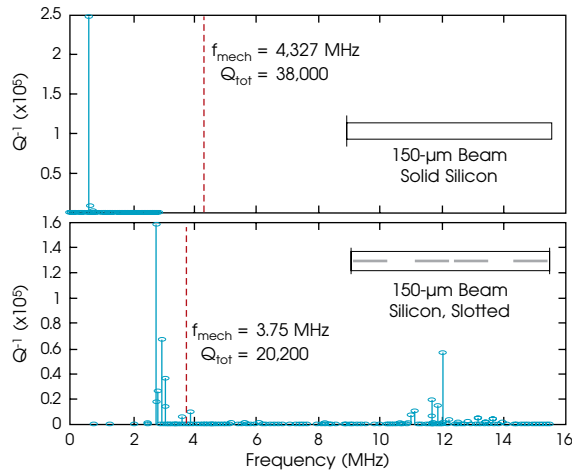


Figure 3. Q values for thermal modes in a fixed-fixed, thermally-insulated beam that is 150 μm long and 12 μm wide. The top plot shows the solid beam thermal modes and mechanical resonance, while the bottom plot shows the same beam with 1- μm wide slits along the beam length. The effect of the slits on the thermal modes and their Q values indicated. The mechanical resonance shifts slightly, as expected. The total Q value is lower in the beam with slits.

Since it is not always possible to predict the most relevant thermal mode and its time constant intuitively, the numerical approach can be extremely helpful. We see that simple modifications to the resonator can have the effect of completely altering the thermal mode structure and introducing complicated weightings in the Q calculation.

Both the frequency and the spatial overlap of the thermal modes are clearly important. When modes that have high spatial overlap are also close to the mechanical resonance frequency, large thermoelastic damping results. Since structural modifications that have a beneficial impact in some frequency regimes can be detrimental in others, engineering to optimize Q can be greatly enabled through the use of the numerical approach described here.

CONCLUSION

This paper presented two new tools to evaluate and optimize MEMS structures for low thermoelastic damping. The weakly coupled approach is based on original work by Zener. We reviewed Zener's approach and showed how numerical finite-elements-based approaches can be used to fully leverage Zener's theory. In the weakly coupled approach, the fundamental thermodynamic energy expressions are coupled. However, the strain and temperature solutions used to evaluate these energies are taken from solutions to uncoupled, standard mechanical and thermal equations. This allows us to use readily available finite-element packages and evaluate thermoelastic damping. The approach enables a great deal of insight into the energy loss mechanism. We find that a spatial overlap of thermal modes with the strain profile in the mechanical mode of interest is a dominant term in the damping. In addition, the frequency separation between relevant thermal modes and the mechanical resonance frequency must be considered. By studying the damping contributions of individual thermal modes, their mode shapes, and their frequencies, it is possible to engineer MEMS resonators for higher Q. In addition, by reviewing the fundamental coupled thermodynamic energy expressions, we achieve a greater insight into the energy loss mechanism itself.

Finally, this paper outlines a method for solving the fully coupled thermoelastic dynamics to obtain exact expressions for Q in an arbitrary resonator. The fully coupled simulations enable a precise evaluation of Q. We derive both 3D equations, as well as 2D plane stress thermoelastic equations. The simulations were conducted in Comsol Multiphysics. This software can parameterize the material parameters and geometry, so that detailed optimization studies are enabled. We showed that the fully coupled simulations predict thermoelastically limited Q in structures reported in the literature.

ACKNOWLEDGMENTS

The authors would like to thank Mark Mescher and Ed Carlen at Draper Laboratory, as well as Saurabh Chandorkar and Professor Ken Goodson at Stanford University for valuable conversations. We also thank Neil Barbour and John McElroy for support at Draper. This work was supported by DARPA HERMIT (ONR N66001-03-1-8942). The authors thank Dr. Clark Nguyen for his support of this portion of the project.

REFERENCES

- [1] Lifshitz, R. and M. Roukes, *Phys. Rev. B*, Vol. 61, No. 8, 2000, p. 61.
- [2] Houston, B.H., D.M. Photiadis, M.H. Marcus, J.A. Bucaro, X. Liu, J.F. Vignola, *Appl. Phys. Lett.*, Vol. 80, No. 7, 2002, pp. 1300.
- [3] Roszhart, T.V., "Micromachined Silicon Resonators," *Electro International*, 1991.
- [4] Srikar, V.T. and S.D. Senturia, "Thermoelastic Damping in Fine-Grained Polysilicon Flexural Beam Resonators," *J. Microelectromechanical Systems*, Vol. 11, No. 5, 2002, pp. 499-504.
- [5] Abdolvand, R. et al., "Thermoelastic Damping in Trench-Re-filled Polysilicon Resonators," *Proc. Transducers, Solid-State Sensors, Actuators and Microsystems*, 12th International Conference, 2003.
- [6] Duwel, A., J. Gorman, M. Weinstein, J. Borenstein, P. Ward, *Sens and Actuators A*, Vol. 103, 2003, pp. 70-75.
- [7] Zener, C., "Internal Friction in Solids: I. Theory of Internal Friction in Reeds," *Physical Review*, Vol. 52, 1937, p. 230.
- [8] Zener, C., "Internal Friction in Solids: II. General Theory of Thermoelastic Internal Friction," *Physical Review*, Vol. 53, 1938, p. 90.
- [9] Candler, R.N., M. Hopcroft, W.-T. Park, S.A. Chandorkar, G. Yama, K.E. Goodson, M. Varghese, A. Duwel, A. Partridge, M. Lutz, and T. W. Kenny, "Reduction in Thermoelastic Dissipation in Micromechanical Resonators by Disruption of Heat Transport," *Proceedings of Solid State Sensors and Actuators*, 2004, pp. 45-48.
- [10] Nowick, A.S. and B.S. Berry, *Anelastic Relaxation in Crystal-line Solids*, Chapter 17, Academic Press, New York, 1972.
- [11] Comsol Multiphysics is a product of Comsol, Inc. <http://www.comsol.com>.
- [12] Gorman, J., *Finite Element Model of Thermoelastic Damping in MEMS*, Master of Science Thesis, Department of Materials Science, Massachusetts Institute of Technology, 2002.
- [13] Antkowiak, B., J.P. Gorman, M. Varghese, D.J.D Carter, A. Duwel, "Design of a High Q Low Impedance, GHz-Range Piezoelectric Resonator," *Proc. Transducers, Solid-State Sensors, Actuators and Microsystems*, 12th International Conference, 2003.
- [14] Schaffler F., *Properties of Advanced Semiconductor Materials GaN, AlN, InN, BN, SiC, SiGe*, M.E. Levinshstein, S.L. Rumyantsev, M.S. Shur, Eds., John Wiley & Sons, Inc., New York, 2001, pp. 149-188.
- [15] Quévy, E.P., S.A. Bhave, H. Takeuchi, T.-J. King, R.T. Howe, "Poly-SiGe High Frequency Resonators Based on Lithographic Definition of Nano-Gap Lateral Transducers," *Proceedings of Solid State Sensors and Actuators*, 2004, pp. 360-363.
- [16] Evoy, S., A. Olkhovets, L. Sekaric, J.M. Parpia, H.G. Craighead, D.W. Carr, "Temperature-Dependent Internal Friction in Silicon Nanoelectromechanical Systems," *Applied Physics Letters*, Vol. 77, No. 15, 2000, pp. 2397-2399.
- [17] <http://www.memsnet.org>
- [18] Roark, Y., *Formulas for Stress and Strain*, McGraw-Hill, New York, 1975.
- [19] Nowacki, *Thermoelasticity*, Pergamon Press, Elmsford, New York, 1962.
- [20] Mattilia, T., A. Oja, H. Seppä, O. Jaakkola, J. Kiihamäki, H. Kattelus, M. Koskenvuori, P. Rantakari, J. Tittonen, "Micro-mechanical Bulk Acoustic Wave Resonator," IEEE Ultrasonics Symposium, 2002, p. 945.
- [21] Abdolvand, R., G. Ho, A. Erbil, F. Ayazi, "Thermoelastic Damping in Trench-Refilled Polysilicon Resonators," *Proc. Transducers, Solid-State Sensors, Actuators and Microsystems*, 12th International Conference, 2003.
- [22] Ayazi, H., "Thermoelastic Damping in Flexural Mode Ring Gyroscopes," 2005 ASME, November 5-11, 2005, Orlando, FL.
- [23] Bindel, D.S. and S. Govindjee, "Elastic PMLs for Resonator Anchor Loss Simulation," *Int. Journal for Numerical Methods in Engineering*, Vol. 64, No. 6, October 2005, pp. 789-818.
- [24] Bhave, S.A., B.L. Bircumshaw, W.-Z. Low, Y.-S. Kim, A.P. Pisano, T.-J. King, and R.T. Howe, "Poly-SiGe: a High-Q Structural Material for Integrated RF MEMS," Solid-State Sensor, Actuator and Microsystems Workshop, Hilton Head Island, South Carolina, June 2-6, 2002.
- [25] Bindel, D.S., E. Quévy, T. Koyama, S. Govindjee, J.W. Demmel, and R.T. Howe, "Anchor Loss Simulation in Resonators," 18th IEEE Microelectromechanical Systems Conference (MEMS-05), Miami, Florida, January 30 - February 3, 2005.

(l-r) Amy E. Duwel and Mathew Varghese



Amy E. Duwel is currently the MEMS Group Leader at Draper Laboratory and a Principal Member of the Technical Staff. Her technical interests focus on microscale energy transport and on the dynamics of MEMS resonators in applications as inertial sensors, RF filters, and chemical detectors. She received a BA in Physics from the Johns Hopkins University, Baltimore, MD (1993) and MS and PhD degrees (1995 and 1999, respectively) in Electrical Engineering and Computer Science from MIT, Cambridge.

Rob N. Candler is a Senior Research Engineer at the Robert Bosch Research and Technology Center. His research has focused on wafer-level packaging of silicon resonators and inertial sensors and energy dissipation in resonators. He is currently working on fundamental limitations of MEMS devices under the DARPA Science and Technology Fundamentals Program. He received a BS in Electrical Engineering from Auburn (2000) and MS and PhD degrees in Electrical Engineering from Stanford University (2004 and 2006, respectively).

Thomas W. Kenny was with the NASA Jet Propulsion Laboratory from 1989 to 1993, where his research focused on the development of electron-tunneling high-resolution microsensors. In 1994, he joined the Mechanical Engineering Department at Stanford University, Stanford, CA, where he directs MEMS-based research in a variety of areas including resonators, wafer-scale packaging, cantilever beam force sensors, microfluidics, and novel fabrication techniques for micromechanical structures. He is a founder and CTO of Cooligy, a microfluidics chip cooling components manufacturer, and founder and board member of SiTime, a developer of CMOS timing references using MEMS resonators. He has authored and coauthored more than 200 scientific papers and holds 40 patents. He is currently the Stanford Bosch Faculty Development Scholar and the General Chairman of the 2006 Hilton Head Solid-State Sensor, Actuator, and Microsystems Workshop. He received a BS in Physics from the University of Minnesota (1983) and MS and PhD degrees in Physics from the University of California, Berkeley (1987 and 1989, respectively).

Mathew Varghese was head of the Microsystems Integration Group and was a Principal Member of Technical Staff at Draper Laboratory. His research interests focused on the fabrication, design, and analysis of microsystems. He led projects to build microphones, drug delivery devices, MEMS RF filters, and Chip Scale Atomic Clocks (CSAC). Dr. Varghese won a Distinguished Performance award for leading the CSAC development effort at Draper. He received a BS in Electrical Engineering and Computer Science with a minor in Physics from the University of California, Berkeley, and SM and PhD degrees in Electrical Engineering and Computer Science from MIT (1997 and 2001, respectively).

Improving Lunar Return Entry Footprints Using Enhanced Skip Trajectory Guidance

Zachary R. Putnam,¹ Robert D. Braun,² Sarah H. Bairstow,³ and Gregory H. Barton⁴

Copyright © 2006 The Charles Stark Draper Laboratory, Inc. Presented at Space 2006 Conference, San Jose, CA, September 19-21, 2006. Sponsored by AIAA

abstract

The impending development of NASA's Crew Exploration Vehicle (CEV) will require a new entry guidance algorithm that provides sufficient performance to meet all requirements. This study examined the effects on entry footprints of enhancing the skip trajectory entry guidance used in the Apollo program. The skip trajectory entry guidance was modified to include a numerical predictor-corrector phase during the atmospheric skip portion of the entry trajectory. Four degree-of-freedom (DOF) simulation was used to determine the footprint of the entry vehicle for the baseline Apollo entry guidance and predictor-corrector enhanced guidance with both high and low lofting at several lunar return entry conditions. The results show that the predictor-corrector guidance modification significantly improves the entry footprint of the CEV for the lunar return mission. The performance provided by the enhanced algorithm is likely to meet the entry range requirements for the CEV.

INTRODUCTION

In 2004, the President of the United States fundamentally shifted the priorities of America's civil space program with the Vision for Space Exploration (VSE), calling for long-term human exploration of the Moon, Mars, and beyond.^[1] This program focuses on returning astronauts to the Moon by 2020 with the eventual establishment of a permanent manned station there. Experience gained from human exploration of the Moon is then to be used to prepare for a human mission to Mars. To complete these tasks, a new human exploration vehicle, the Crew Exploration Vehicle (CEV), will be developed.

1 Graduate Research Assistant, School of Aerospace Engineering, Georgia Institute of Technology, Atlanta, GA.

2 Associate Professor, School of Aerospace Engineering, Georgia Institute of Technology, Atlanta, GA.

3 Draper Fellow, Mission Design and Analysis, Draper Laboratory.

4 Group Leader, Mission Design and Analysis, Draper Laboratory.

The NASA Exploration Systems Architecture Study (ESAS) selected a CEV similar to the Apollo program's Command and Service Module, with a crewed command module and uncrewed service module.^[2] The CEV command module will be a scaled version of the Apollo Command Module (CM), maintaining the same outer moldline with a larger radius. In addition, the CEV will be required to return safely to land locations during normal operations, as opposed to the ocean landings performed in the Apollo program. Successful land recovery operations require an entry guidance algorithm capable of providing accurate landings over a large capability footprint. Preliminary requirements indicate that the CEV entry vehicle must be capable of downranges of at least 10000 km.^[3]

The Apollo program entry guidance contained a long-range option to provide an abort mode in the event of poor weather conditions at the primary landing site. A long-range entry capability also simplifies the phasing and targeting problem by allowing the vehicle to perform entry targeting within the atmosphere during entry, possibly saving propellant during in-space entry targeting. Long-range entries can be achieved easily by moderate lift-to-drag ratio (L/D) blunt body entry vehicles, such as the CEV, by employing a skipping entry trajectory. When performing a skipping entry, the vehicle enters the atmosphere and begins to decelerate. The vehicle then uses aerodynamic forces to execute a pull-up maneuver, lofting the vehicle to higher altitudes, possibly exiting the atmosphere. However, enough energy is dissipated during the first atmospheric flight segment to ensure that the vehicle will enter the atmosphere a second time at a point significantly farther downrange than the initial entry point. After the second entry, the vehicle proceeds to the surface. A longer range trajectory is achieved in this manner, as shown in Figure 1.

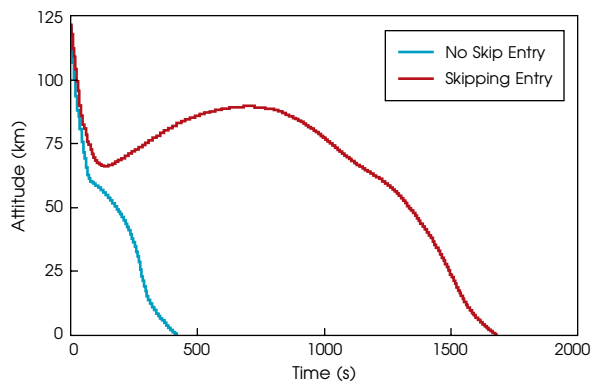


Figure 1. Skipping and nonskipping entry trajectories (altitude vs. time).

The Apollo CM was capable of a maximum entry downrange without dispersions of 4630 km (2500 nmi) when employing the Kepler (ballistic) phase of its skip trajectory guidance.^[4] However, this capability was never utilized. Studies for the First Lunar Outpost in the early 1990s used a 1.05 scale Apollo CM. These studies also employed the Apollo entry guidance algorithm and found a similar maximum downrange without dispersions of 4445 km (2400 nmi).^[5] However, in this study, trajectories using the Kepler phase of the guidance were excluded from nominal trajectory design for the following reasons:

- (1) Desire to maintain aerodynamic control of the vehicle throughout entry.
- (2) Relative difficulty of accurate manual control to long-range targets in the event of a guidance failure.
- (3) Sensitivity to uncertainty at atmospheric interface and within the atmosphere, leading to inaccurate landings.
- (4) No operational necessity for long-range entries.^[5]

While these issues remain significant concerns for the design of the CEV entry system, preliminary requirements state that the CEV must be able to achieve a downrange of at least 10,000 km. Recent analyses indicate that the moldline of the CEV is fully capable of achieving downranges of this magnitude.^[6] However, significant enhancements in the Apollo algorithm are required to maintain landed accuracy at these downranges.

Method

The entry footprint of the CEV entry vehicle was evaluated with a 4-DOF simulation written in Matlab and Simulink. Entry trajectories were simulated over a range of flight path angles, crossrange and downrange commands using the baseline Apollo skip trajectory guidance and both high and low lofting predictor-corrector enhanced entry guidance algorithms. Uncertainty analysis was not included in this feasibility study.

Definitions

This study utilized the following definitions. Atmospheric interface, the altitude at which the entry vehicle enters the sensible atmosphere, was defined to be 122 km (400,000 ft) above the Earth's reference ellipsoid. Flight path angle (FPA) refers to the entry vehicle's inertial flight path angle at atmospheric interface. The inertial flight path angle is the angle between the vehicle's velocity vector and the local horizontal, where negative values refer to angles below the horizon. Downrange is defined as the in-plane distance traveled by the

vehicle from atmospheric interface to landing. Crossrange is defined as the out-of-plane distance traveled by the vehicle from atmospheric interface to landing. Miss distance is defined as the distance between the targeted landing site and the actual landing site. For the purposes of this study, an acceptable footprint was defined as the region within which the CM achieved a miss distance of 3.5 km or less.

Assumptions

Several assumptions were made for the analysis performed in this study. The atmosphere was assumed to be the 1962 U.S. Standard Atmosphere to facilitate comparison with original Apollo program data. All entries were assumed to be posigrade equatorial. The entry state used is given in Table 1. The entry vehicle used was a scaled Apollo CM, as outlined in the ESAS,^[2] with a maximum diameter of 5 m. Hypersonic blunt body aerodynamics were used, and the vehicle was flown at trim angle of attack, generating a lift-to-drag ratio (L/D) of 0.4. Entry vehicle properties are summarized in Table 2.

Table 1. Vehicle Entry State.

Parameter	Value
Inertial Velocity	11032 m/s
Altitude	122 km
Longitude	0 deg
Latitude	0 deg
Azimuth	90 deg

Table 2. Vehicle Properties.

Parameter	Value
Mass	8075 kg
Reference Area	23.758 m ²
L/D	0.4

Parameters Varied

Crossrange commands were varied between 0 km and 1000 km; downrange commands were varied between 1500 km and 13000 km. This set of commands fully captured the capability footprint of the entry vehicle. Three flight path angles were selected to examine vehicle footprints over a range of atmospheric interface conditions, as shown in Table 3. Two of the FPAs were selected based on a CEV emergency ballistic entry (EBE) study conducted at the Charles Stark Draper Laboratory in September 2005. This set of parameters was used with both the baseline skip trajectory guidance and the high and low lofting versions of the enhanced skip trajectory guidance.

Table 3. Flight Path Angle Selections.

FPA	Selection Criteria
-5.635 deg	Center of aerodynamic corridor
-5.900 deg	Approximate shallow boundary for EBE
-6.100 deg	Approximate steep boundary for EBE

RESULTS: BASELINE ALGORITHM

Baseline Algorithm Description

The primary function of the entry guidance algorithm is to manage energy as the spacecraft descends to the parachute deploy interface. The bank-to-steer algorithm controls lift in the coupled vertical and lateral channels, with guidance cycles occurring at a frequency of 0.5 Hz.

Guidance's chief goal is to manage lift in the vertical channel so that the vehicle enters into the wind-corrected parachute deploy box at the appropriate downrange position. For a given FPA, full lift-up provides maximum range while full lift-down provides the steepest descent. Lift-down may be constrained by the maximum allowed g-loads that can be experienced by the crew and vehicle. Any bank orientation other than full lift-up or full lift-down will result in a component of lift in the lateral channel. Crossrange position is controlled in the lateral channel by reversing the lift command into the mirror quadrant (e.g., +30 deg from vertical to -30 deg) once the lateral range errors to the target cross a threshold. The vehicle continues this bank command reversal strategy as it descends to the target. As the energy and velocity decrease, the lateral threshold is reduced so that the vehicle maintains control authority to minimize the lateral errors prior to chute deploy.

The baseline Apollo algorithm consists of seven phases designed to control the downrange position of the vehicle, as shown in Figure 2.

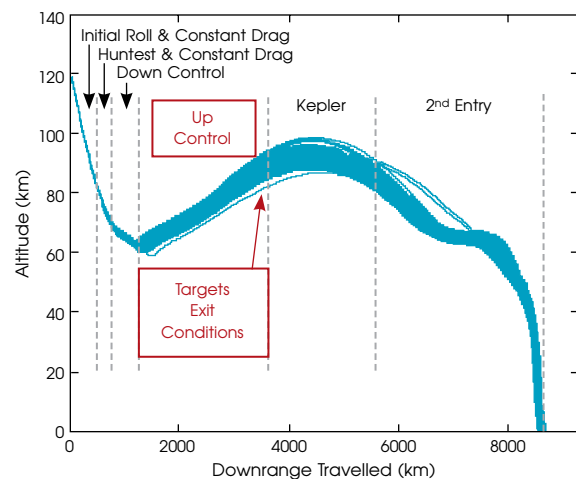


Figure 2. Baseline algorithm entry guidance phases.

- (1) Preentry Attitude Hold: maintains current attitude until a sensible atmosphere has been detected.
- (2) Initial Roll: seeks to guide the vehicle toward the center of the entry corridor, nominally commanding the lift vector upward, otherwise commanding the lift vector downward to steepen a shallow entry.
- (3) Hunttest and Constant Drag: begins once atmospheric capture is ensured, triggered by an altitude rate threshold. This phase determines whether the vehicle will need to perform an upward “skip” in order to extend the vehicle’s range, decides which of the possible phases to use, and calculates the conditions that will trigger those phases. The algorithm transitions to the Downcontrol phase once a suitable skip trajectory is calculated; otherwise, the algorithm transitions directly to the Final (“Second Entry”) phase if no skip is needed.
- (4) Downcontrol: guides the vehicle to pullout using a constant drag policy.
- (5) Upcontrol: guides the vehicle along a reference trajectory, previously generated by the Hunttest phase. This trajectory is not updated during the Upcontrol phase. The algorithm transitions into the Kepler phase if the skip trajectory is large enough to exit the atmosphere; otherwise, the algorithm transitions directly into the Final (“Second Entry”) phase.
- (6) Kepler (“Ballistic”): maintains current attitude along the velocity vector from atmospheric exit to atmospheric second entry. Exit and second entry transitions are defined to occur at an aerodynamic acceleration of 0.2 g.
- (7) Final (“Second Entry”): guides the vehicle along a stored nominal reference trajectory, calculated preflight. Once the velocity drops below a threshold value, the algorithm stops updating bank commands and the guidance algorithm is disabled.

The guidance phases and phase-transition logic are discussed fully in Reference [7].

Results Summary

The results presented below are given in footprint plots. These plots show the miss distance associated with a particular downrange and crossrange command. Dark blue areas indicate accurate landings, while red areas

indicate large miss distances. Light blue and dark blue areas provide acceptable accuracy, corresponding to miss distances of 3.5 km or less. It should be noted that red areas denote miss distance of 10 km or greater, with some miss distances in excess of 1000 km.

Baseline Algorithm Results

The entry guidance algorithm used for the Apollo program was selected as the baseline algorithm for the CM entry guidance. Figures 3-5 show the landed accuracy over a range of downrange and crossrange commands for several FPAs (see Table 3). Figure 4 shows the footprint outlines at several FPAs.

Figure 3 shows the footprint for the baseline algorithm at an FPA of -5.635 deg. Maximum crossrange is approximately ± 700 km. Minimum downrange is 2250 km; maximum downrange is 7000 km. Within these ranges, the algorithm performs well. Figure 4 shows the footprint for the baseline algorithm at an FPA of -5.900 deg. Performance remains similar at this FPA. The minimum downrange decreases to 2000 km, while the maximum downrange remains 7000 km, with the exception of crossranges less than ± 50 km. Some improvement is made in long-range performance, but accurate regions are patchy. Figure 5 shows the footprint for the baseline algorithm at an FPA of -6.100 deg. Significant performance improvements are visible at this FPA. Maximum downrange increases to 7500 km; minimum downrange is 2000 km. Maximum crossrange increases to ± 750 km at large downranges. Long-range performance becomes accurate in two regions at crossranges greater than 400 km.

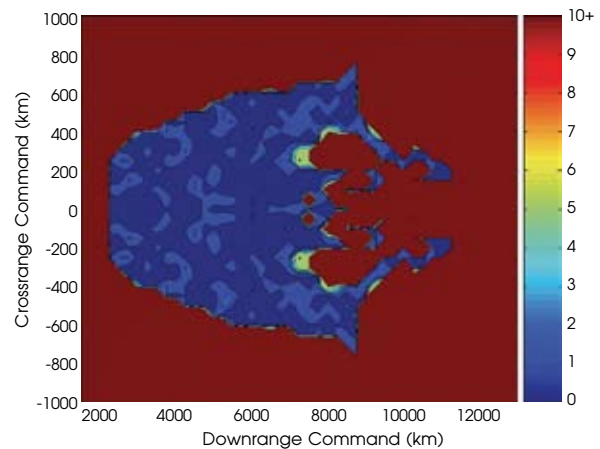


Figure 3. Baseline miss distance (km) with FPA = -5.635 deg.

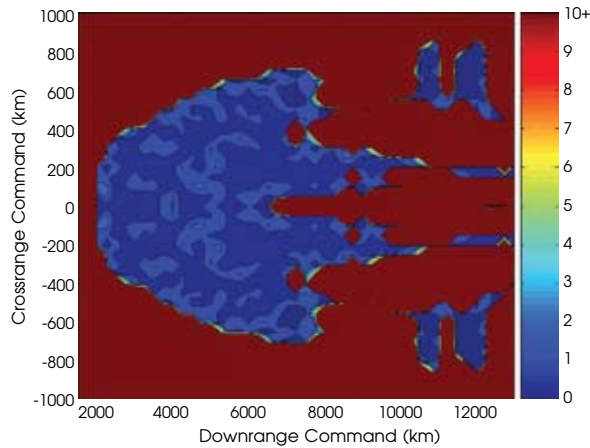


Figure 4. Baseline miss distance (km) with FPA = -5.900 deg.

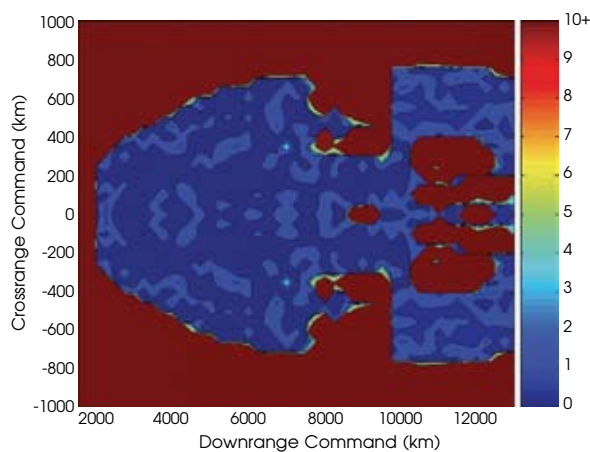


Figure 5. Baseline miss distance (km) with FPA = -6.100 deg.

Overall, the baseline algorithm provides good performance over downrange commands between 2000 km and 7000 km with crossranges up to 700 km, as shown in Figure 6. However, improvement is required for long-range performance.

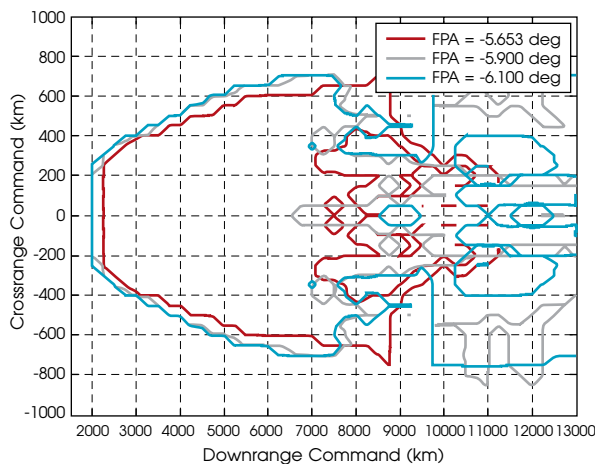


Figure 6. Baseline range capability over several FPAs, miss distance < 3.5 km.

Rationale for Algorithm Improvement

Analysis of trajectories for long target ranges showed that the degradation of precision landing performance for the baseline Apollo algorithm occurred as the result of two issues. First, the Upcontrol phase did not guide the vehicle to the desired exit conditions calculated by the Hunttest phase. The control gains for the reference-following controller were likely designed with shorter target ranges in mind, and did not achieve the intended results for the longest target ranges. Second, the exit conditions calculated by Hunttest were inaccurate due to an outdated assumption. Since the baseline Apollo algorithm was designed for target ranges of less than 4,600 km, the Kepler phase would always be short enough to ignore the effects of accumulated drag in the Kepler phase when calculating the exit conditions. For the much-longer target ranges intended for the CEV, this assumption is no longer valid. These two issues combined to cause severe undershoot in the longest target ranges.

RESULTS: ENHANCED GUIDANCE ALGORITHM

Enhanced Algorithm Description

The issues causing degradation in precision landing performance for long target ranges using the baseline Apollo algorithm were resolved by implementing three enhancements to the algorithm. First, the Upcontrol and Kepler phases were replaced with a numeric predictor-corrector (NPC) algorithm, which targets the second entry conditions rather than the atmospheric exit conditions. This change in the guidance phase logic is reflected in Figure 7. The NPC algorithm used for this purpose, PredGuid, is an aerocapture NPC guidance algorithm developed for the Aero-assist Flight Experiment (AFE). The PredGuid algorithm is described in Reference [8]. An analytic predictor-corrector option was investigated but rejected due to the lack of a suitable closed-form expression to describe the entire skip trajectory.

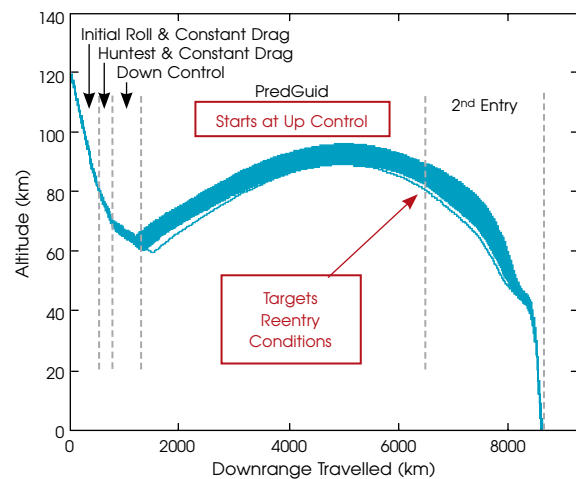


Figure 7. Enhanced PredGuid algorithm.

Next, the Final phase reference trajectory was redefined and extended to recenter it with respect to the CEV's range capability, since the CEV has different vehicle characteristics from the Apollo CM. Finally, the Final phase range estimation method used by the Hunttest and PredGuid phases was updated to enable the new Final phase reference trajectory to support a wider spread of target ranges. More detail about the enhancements made to the algorithm is available in Reference [9].

The affects of modulating the start time of the PredGuid phase was also investigated. A comparison was made between starting the PredGuid phase at the beginning of the Upcontrol Phase (as described above) and starting the PredGuid phase at the beginning of the Downcontrol phase. The difference in these two approaches resulted in different trajectory shaping. Starting the PredGuid phase at the nominal time by replacing the Upcontrol and Kepler phases resulted in a lower-altitude, shallower skip trajectory. Starting the PredGuid phase earlier by also replacing the Downcontrol phase resulted in a higher-altitude, steeper lofting.

Enhanced Algorithm Results

The results presented below detail the entry footprint of the CM using the enhanced numerical predictor-corrector guidance algorithm with both high and low lofting. Figures 8-13 show the landed accuracy, in terms of miss distance, of the CM at various downrange and crossrange commands for a given FPA. Figures 11 and 12 show the footprint outlines for high and low lofts for several FPAs.

Figure 8 shows the footprint for a low loft at an FPA of -5.635 deg. The CM achieves a maximum crossrange of approximately ± 750 km. The minimum downrange is 2250 km and significant accuracy is lost when downranges greater than 10000 km are targeted. The footprint for a low loft at an FPA of -5.900 deg is shown in Figure 9. The CM achieves a maximum crossrange of ± 850 km, an increase of 100 km over the -5.635 deg case. The minimum downrange decreases to 2000 km from 2500 km in the -5.635 deg case. Significant accuracy is still lost when downranges greater than 10000 km are targeted. The footprint for a low loft at an FPA of -6.100 deg is nearly identical to that of the -5.900 deg case (Figure 10). Of note is the much larger red region starting at 11000 km, indicating a deterioration of long-range performance with steepening FPA.

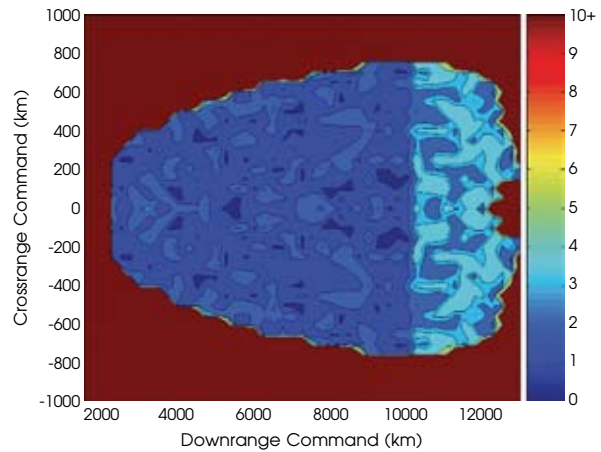


Figure 8. Low loft miss distance (km) with FPA = -5.635 deg.

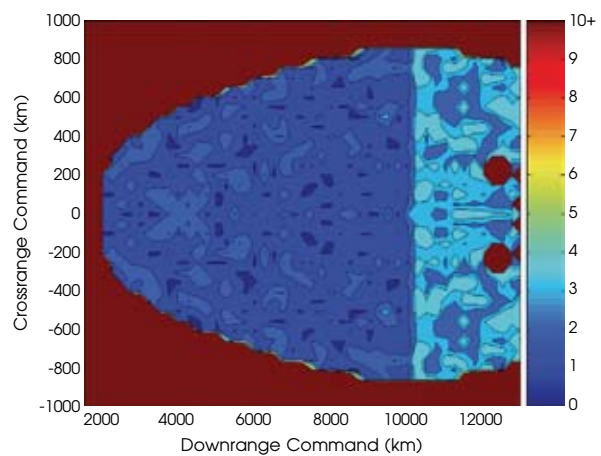


Figure 9. Low loft miss distance (km) with FPA = -5.900 deg.

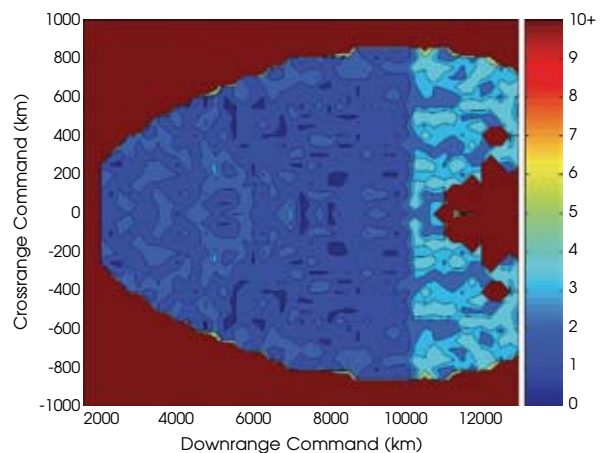


Figure 10. Low loft miss distance (km) with FPA = -6.100 deg.

Figure 11 shows the footprint for a high loft at an FPA of -5.635 deg. The CM achieves a maximum crossrange of approximately ± 900 km, a 150-km increase over the low loft case. The minimum downrange is 2250 km and the maximum downrange is 11250 km. No accuracy is lost between 10000 km and 11250 km as in the low loft case. The footprint for a high loft at an FPA of -5.900 deg is slightly better (Figure 12). The CM achieves a maximum crossrange of ± 950 km. The minimum downrange is 2000 km and the maximum downrange is 11000 km, slightly less than the -5.635 deg case. Of particular note are two regions of inaccuracy near 3000 km downrange. Figure 13 shows the footprint for a high loft at an FPA of -6.100 deg. The CM achieves a maximum crossrange of ± 900 km. Downrange performance is similar to the -5.900 deg case. The two inaccurate regions near 3000 km downrange have disappeared at this FPA.

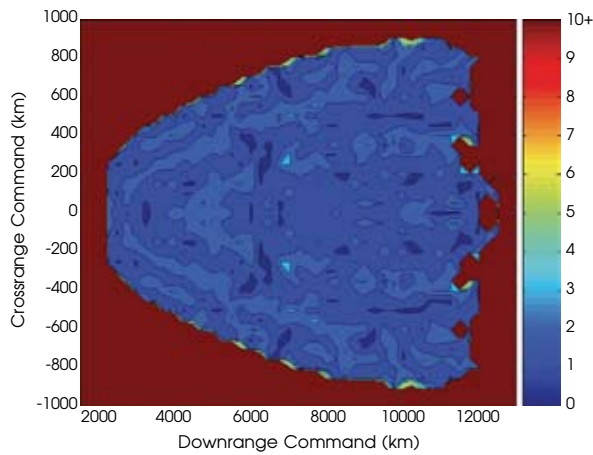


Figure 11. High loft miss distance (km) with FPA = -5.635 deg.

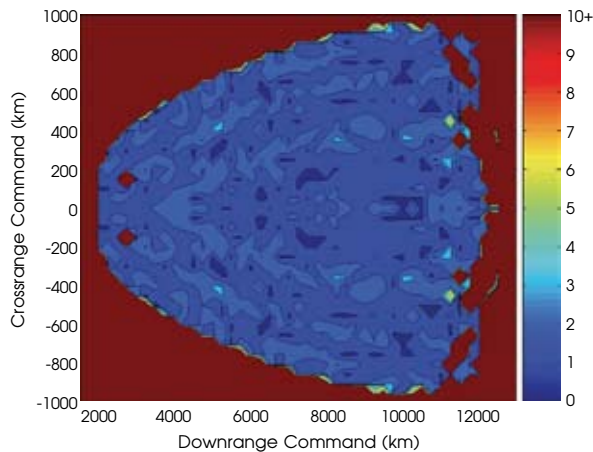


Figure 12. High loft miss distance (km) with FPA = -5.900 deg.

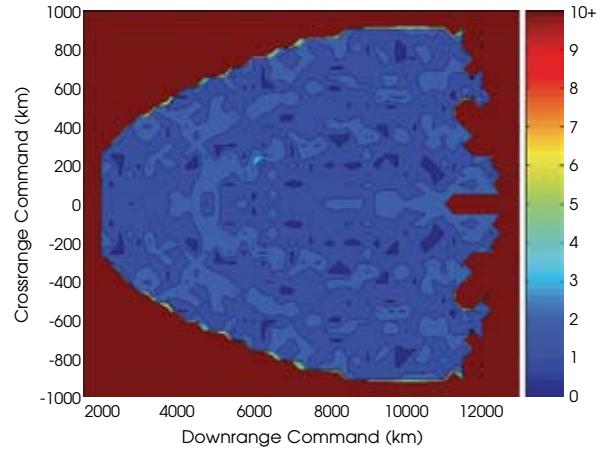


Figure 13. High loft miss distance (km) with FPA = -6.100 deg.

Figures 14 and 15 show the footprints for low and high loft trajectories, respectively, at three FPAs. The footprint outlines correspond to miss distances of 3.5 km or less. As shown before, -5.900 deg and -6.100 deg provide similar performance, while -5.635 deg is slightly less capable. All trajectories begin to lose accuracy beyond 10000 km. As in the low loft cases, the performance of the high loft -5.900 deg and -6.100 deg cases is similar, with the exception of the two inaccurate regions in the -5.900 deg case near 3000 km downrange. The -5.635 deg case is slightly less capable in minimum downrange and maximum crossrange, but slightly more capable in maximum downrange, providing capability to 11250 km.

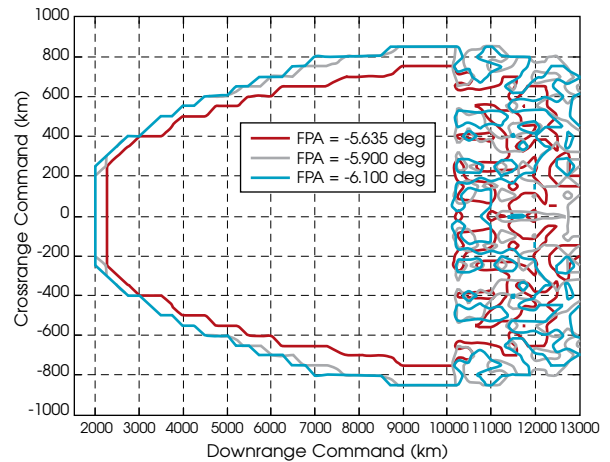


Figure 14. Low loft footprints for several FPAs, miss distance < 3.5 km.

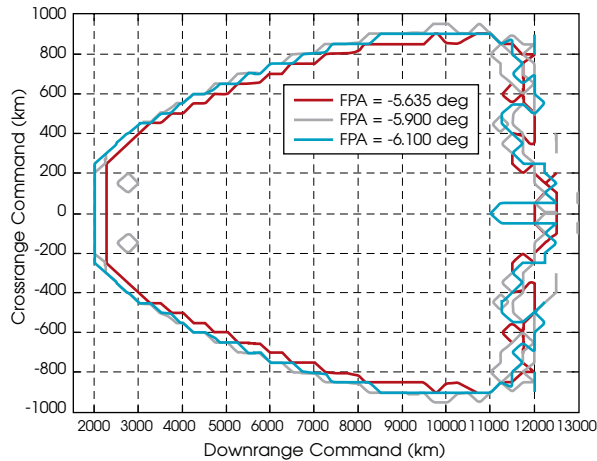


Figure 15. High loft footprints for several FPAs, miss distance $<3.5\text{ km}$.

These data show that with the inclusion of the enhanced guidance algorithm, range performance is consistent over a large downrange and crossrange area. The shapes of the footprints are consistent with previous work performed with the Apollo CM. Over a range of FPAs, a crossrange of $\pm 900\text{ km}$ is easily achievable with reasonable accuracy, while a downrange of $11000+$ km is easily within the vehicle's capability. Table 4 provides a summary of the range performance data.

As shown in Table 4, there is no significant change in landing accuracy within the range of FPAs examined. Miss distances of the CM remain within 3.5 km for low loft trajectories with downranges less than 10000 km . Miss distances of the CM remain within 3.5 km for high loft trajectories with downranges less than 11000 km ,

with the exception of two regions near 3000 km downrange at an FPA of -5.900 deg . It should be noted that these analyses include no uncertainty.

At steeper FPAs with a low loft trajectory, the maximum crossrange capability is increased slightly and the minimum downrange is decreased, both desirable effects. High loft trajectories exhibit similar minimum downrange performance with increased maximum crossranges. While the minimum downrange capability is better for steeper FPAs with high lofting, no clear advantage exists in crossrange performance for steep or shallow FPAs. It should be noted that a compromise between the high and low loft guidance algorithms could be implemented and that such an implementation would further decrease footprint dependence on FPA.

CONCLUSION

The CEV CM achieves significant capability footprint improvements over the baseline algorithm with use of the enhanced predictor-corrector entry guidance algorithm. With this algorithm, the CM can robustly achieve a maximum crossrange of $\pm 900\text{ km}$, a maximum downrange of 10000 km , and a minimum downrange of 2000 km while maintaining a landed accuracy within 3.5 km of the target. In addition, the CM footprint is largely independent of flight path angle at atmospheric interface.

ACKNOWLEDGMENTS

This study was conducted with funding from Draper Laboratory. The authors wish to acknowledge Steve Paschall (Draper Laboratory) for his work in developing the simulation used in this study.

Table 4. Guided Range Performance Summary.

FPA	Minimum Downrange	Maximum Downrange	Maximum Crossrange
Baseline Algorithm			
-5.635 deg	2250 km	7000 km	$\pm 700\text{ km}$
-5.900 deg	2000 km	7000 km	$\pm 700\text{ km}$
-6.100 deg	2000 km	7500 km	$\pm 750\text{ km}$
Low Loft Enhanced Algorithm			
-5.635 deg	2250 km	10000 km	$\pm 750\text{ km}$
-5.900 deg	2000 km	10000 km	$\pm 850\text{ km}$
-6.100 deg	2000 km	10000 km	$\pm 850\text{ km}$
High Loft Enhanced Algorithm			
-5.635 deg	2250 km	11000 km	$\pm 900\text{ km}$
-5.900 deg	2000 km	11000 km	$\pm 950\text{ km}$
-6.100 deg	2000 km	11000 km	$\pm 900\text{ km}$

REFERENCES

- [1] The White House Website Presidential News and Speeches, "President Bush Announces New Vision for Space Exploration Program," URL: <http://www.whitehouse.gov/news/releases/2004/01/20040114-3.html>, October 26, 2005.
- [2] *Exploration Systems Architecture Study Final Report*, NASA TM-2005-214062, November 2005.
- [3] *NASA Solicitation: Conceptual Design of an Air Bag Landing Attenuation System for the Crew Exploration Vehicle*, Langley Research Center Press Release, December 14, 2005.
- [4] Graves, C.A. and J.C. Harpold, *Reentry Targeting Philosophy and Flight Results from Apollo 10 and 11*, MSC 70-FM-48, March 1970.
- [5] Tigges, M. et al., *Earth Land-Landing Analysis for the First Lunar Outpost Mission: Apollo Configuration*, NASA JSC-25895, June 1992.
- [6] Putnam, Z.R. et al. "Entry System Options for Human Return from the Moon and Mars," AIAA 2005-5915, AIAA Atmospheric Flight Mechanics Conference, San Francisco, CA, August 2005.
- [7] Morth, R., *Reentry Guidance for Apollo*, MIT/IL R-532 Vol. I, 1966.
- [8] DiCarlo, J.L., *Aerocapture Guidance Methods for High Energy Trajectories*, SM Thesis, Department of Aeronautics and Astronautics, MIT, June 2003.
- [9] Bairstow, S.H., *Reentry Guidance with Extended Range Capability for Low L/D Spacecraft*, SM Thesis, Department of Aeronautics and Astronautics, MIT, February 2006.

bios

(l-r) Zachary R. Putnam,
Gregg H. Barton and
Robert D. Braun



Zachary R. Putnam performed his graduate research work in the area of entry system design and performance. He currently supports the development of skip entry guidance for NASA's Crew Exploration Vehicle at Draper's Johnson Space Center field site. He holds an MS in Aerospace Engineering from Georgia Tech.

Robert D. Braun is an Associate Professor in the Guggenheim School of Aerospace Engineering at the Georgia Institute of Technology. As Director of Georgia Tech's Space Systems Design Laboratory, he leads a research and education program focused on the design of advanced flight systems and technologies for planetary exploration. In addition, Dr. Braun provides consulting services in the areas of space systems engineering and analysis, planetary entry, and Mars atmospheric flight. He has provided independent analysis and review services for the Mars Global Surveyor, Mars Odyssey, Mars Exploration Rover, Genesis, Phoenix Mars Scout, and Mars Science Laboratory flight projects. Dr. Braun received a BS in Aerospace Engineering from Penn State (1987), an MS in Astronautics from the George Washington University (1989), and a PhD in Aeronautics and Astronautics from Stanford University (1996).

Sarah H. Bairstow performed her Master's thesis research on the topic of reentry guidance algorithms for low L/D spacecraft as a Draper Fellow under the advisement of Gregg Barton, after which she began full-time employment at Draper to expand on that research. She has been employed since June 2006 as a Space Mission Systems Concept Analyst at the Jet Propulsion Laboratory in Pasadena, CA. She received an MS in Aeronautics and Astronautics from MIT (2006).

Gregg H. Barton has been with the Laboratory since 1985 and is currently the Group Leader for the Mission Design and Analysis for Earth, Moon, and Mars GN&C systems, and the Draper Project Lead for Skip Guidance Technologies for Earth return vehicles. Responsibility over the years includes all levels of project development from requirements and interfaces, concept design and analysis, algorithm and software development, and test and verification for flight certification. Management duties have included all levels from task lead, project lead, technical director, proposal manager to program manager. In addition to these duties, he has served as technical supervisor and mentor for new staff and MIT graduates.

A Deep Integration Estimator for Urban Ground Navigation

Dale Landis, Tom Thorvaldsen, Barry Fink, Peter Sherman, Steven Holmes

Copyright © 2006, IEEE. Presented at IEEE PLANS, San Diego, CA, April 25-27, 2006

abstract

The objective of the Personal Navigator System (PNS) is to construct a wearable navigation system that provides accurate position over extended missions in a deprived Global Positioning System (GPS) environment. The prototype multisensor navigator included a set of micromechanical inertial sensors, a three-axis miniature radar, a selective availability anti-spoofing module (SAASM) GPS receiver, and a barometric altimeter. Real-time embedded software sampled sensor data, controlled GPS receiver tracking loops, and hosted a multisensor optimal estimator whose output position was transmitted via wireless link to a high-resolution personal data accessory (PDA) tracking display. The fully packaged system was field tested in Cambridge, Massachusetts under realistic, GPS-stressed conditions.

This paper focuses on the deep integration (DI) algorithm design used for the optimal estimation of both position and receiver tracking control. The algorithm was tailored here for intermittent GPS visibility on the ground and in outdoor-indoor-outdoor maneuvers. DI has been used previously for missile guidance, navigation, and control with clear sky view.

The PNS required an optimal estimator that combined the nonlinear GPS/inertial DI algorithm with measurements from other sensors. The mission duration here was much longer, and the satellite environment over the ground track was highly variable compared with earlier DI applications. This required the development of strategies for dropping satellites from track after long blockage times and for taking control of newly visible satellites under DI tracking. Here, the advantage of DI tracking is the ability to extract GPS pseudorange information almost instantly if a satellite reappears momentarily from a blockage.

This paper reviews the DI approach with stress on the receiver correlator power measurements, nonlinear filter equations, and the calculation of numerically-controlled oscillator (NCO) commands. Specific problems encountered, such as clock error recalculation and numerical issues, will be mentioned. Urban canyon performance data demonstrating accurate navigation under sparse GPS availability are also described.

INTRODUCTION

The PNS is a small package containing a Draper Laboratory micromechanical inertial measurement unit (IMU), a Rockwell Collins GPS receiver, a triad of Doppler radar velocity sensors, a barometric altimeter, a PDA that allows human user interface, and a processor that contains Draper-developed, real-time navigation software. This package is wearable in a front-mounted configuration by a foot soldier, and its objective is to provide long-term accurate coordinates in both outdoor and indoor environments, including significant periods of GPS signal deprivation.

The software comprises strapped-down navigation algorithms combined with Draper's deep integration (DI) nonlinear filter for processing GPS correlator outputs, based on previous Draper munitions shell applications. Doppler updates, navigation initialization, and satellite line-of-sight (LOS) error estimation were among the many features added for the application.

Demonstration in a full hardware mode was done in Spring 2005. An example is shown in Figure 1.

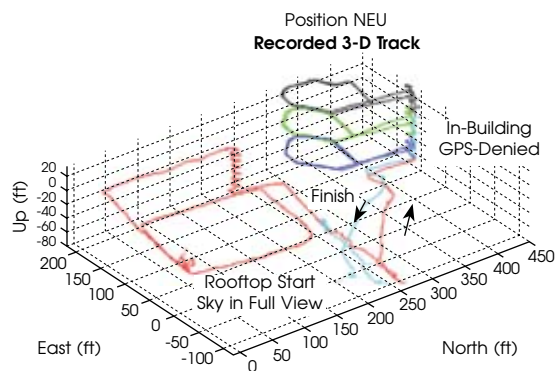


Figure 1. Real-time PNS test results in Technology Square, Cambridge.

The test illustrated involved an outdoor phase followed by an indoor GPS-deprived period. Figure 1 shows that position accuracy was maintained, even during the indoor phase. An overlay of the recorded track onto geolocated floor plans showed very good registration with hallways. In the vertical direction, stairwell landings are clearly seen. The PNS effectively locates the user to the correct floor. The tests also showed that on return to the outdoor environment, GPS resumed almost immediately. Results of this test program were reported at JNC'05.^[1]

The algorithm that accomplished this performance is surveyed in subsequent sections, with emphasis on the components that required fresh techniques.

NAVIGATION ALGORITHM AND RELATED CALCULATIONS

The inputs to the navigation algorithm are 100-Hz sampled specific force (accelerometers) and rate (gyroscopes) in a PNS orthogonal body-fixed frame that is designated by b in this paper. The core of the PNS navigation algorithm is a standard strapped-down integration algorithm comprising

IMU compensation, quaternion third-order integration, gravity compensation of accelerometer outputs, and velocity and position integration in earth-fixed, earth-centered (ecef or e) coordinates. For future reference, the navigation major outputs are:

$$\begin{aligned}\hat{r} &= \text{position } e \text{ frame} \\ \hat{v} &= \text{velocity } e \text{ frame} \\ q &= \text{quaternion } b \text{ to } e \\ C_b^e &= \text{direction cosine matrix}\end{aligned}$$

Navigation initialization, omitting many details, is as follows. The receiver begins with conventional acquisition and tracking, downloads ephemeris, and sends a position and velocity to navigation. A crude azimuth estimate is made by assuming an initial north and level orientation (accuracy of 10 deg in azimuth is sufficient). Once the receiver enters deep integration mode (less than a minute), the wearer moves horizontally, and the filter is able to refine the attitude estimates sufficiently for continued operation using the difference between IMU- and GPS-determined accelerations. Current work at Draper includes more advanced forms of attitude initialization that impose less artificial restraints on the PNS wearer.

In addition to navigation proper, there are calculations that keep track of optimal estimates of other quantities, primarily the following:

$$\begin{aligned}\delta t_R &= \text{user (receiver) clock bias} \\ \delta i &= \text{user clock frequency error} \\ \delta b_k &= \text{LOS delay error satellite } k\end{aligned}$$

An error filter based on perturbation of the navigation algorithm is used to process all the measurements. The filter states are listed for future reference in Table 1.

Table 1. PNS Filter States.

Error	States	Units
Position δr	3	chips
Velocity δv	3	chips/s
Attitude ψ	3	rad
Gyro Bias Shift	3	rad/s
Gyro Bias Markov	3	rad/s
Accel. Bias Shift	3	chips/s ²
Accel. Bias Markov	3	chips/s ²
User Clock Bias	1	chips
User Clock Frequency	1	chips/s
Doppler Misalignment (6)	6	rad
Satellite Delay	12	chips
Altimeter Bias	1	chips

The chip units are defined for P code (which is used in PNS) by 96.146 ft/chip or 9.775×10^{-8} s/chip.

The filter performs the GPS DI updates plus Kalman updates for the other sensors. A set of corrections for the navigation system and clock model are computed and then fed back to the navigation algorithm for a reset of the full system state.

The algorithm-embedded software is coded in three rate groups: high (100 Hz), medium (50 Hz), and low (10 Hz). High rate performs IMU compensation, attitude integration, and incremental transition matrix calculations. Medium rate performs navigation position and velocity integration, bookkeeping of the receiver clock error estimate and satellite atmospheric delay estimates, and all GPS receiver interfacing (described below). Both high and medium rate perform resets based on corrections supplied by the nonlinear filter. Low rate performs all filter updates and sends corrections to high and medium rate.

DEEP INTEGRATION GPS Background of Draper's Deep Integration

DI was developed to extend GPS tracking to poor GPS signal-to-noise conditions, especially intentional jamming environments. Deep integration requires a custom receiver configured so that the navigation software can issue the numerically controlled oscillator (NCO) commands (overriding the internal tracking loops) and also receive integrated correlator outputs. For previous results with DI, see Ref. [2].

Prior to PNS, Draper DI was used successfully in artillery shells with high dynamics and short duration, where the instrumentation was limited to inertial sensors and the receiver.

For the personal navigator, Draper extended the use of DI in significant ways. First, mission duration in the tests was stretched from minutes to one half hour. There is no inherent mission duration limitation here. Second, the capability of the nonlinear algorithm was extended to perform both the nonlinear GPS updates and conventional Kalman updates (from the Doppler radar and altimeter). In contrast to the fixed set of satellites in view for a short time-of-flight missile, the ground navigation system described here needed to adapt to satellite configuration changes. Finally, of course, this was all done with hardware compressed to a point practical for use by a foot soldier.

A key advantage of DI for the ground navigation application is the ability to recover satellite track after signal

is temporarily lost, perhaps due to masking from a landscape fixture. A second advantage is that deep integration, by design, is able to track a satellite when its power is weaker, due to factors such as forest canopy or indoor attenuation.

Summary and Technical Overview

In conventional operation, the GPS receiver is based on internal tracking loops, in which tracking loops are maintained for GPS code and carrier signals, based on correlator outputs and NCO commands, both of which are invisible to the end user. The user is supplied with pseudo and delta range information tapped from these loops, or final position and velocity. Conventional GPS is covered in numerous sources, among which Ref. [3] may be cited.

In deep integration, the correlator outputs are issued to the navigation processor, along with a code phase (or equivalently, pseudorange) for the replica signal. The navigation software sends rate commands to the receiver NCOs, which the receiver uses to generate the replica signal. This operation replaces the internal loops.

In practice, there is an alternation between modes in PNS. Sometimes (initially and during extended signal loss), the receiver maintains control of tracking loops. Whenever possible, internal loops are replaced by the DI process. These modes are referred to as “receiver control” (internal loops) and “host control” (deep integration).

DESCRIPTION OF PNS DEEP INTEGRATION

A compressed technical summary of deep integration can be given by reference to the main interfaces in PNS, shown in Figure 2. First, the code and carrier NCO commands issued to the receiver are discussed in detail. Then the receiver outputs sent to navigation and their transformation into filter observations are discussed. Finally, the filter corrections applied to the navigator are discussed.

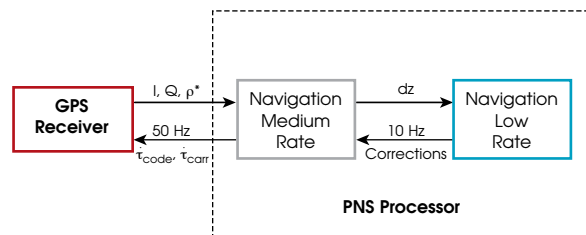


Figure 2. Deep integration interfaces in PNS.

The 50-Hz rate command that the navigator gives to the code NCO is a code phase rate, which may be given in speed of light units as:

$$\dot{\tau}_{\text{code}} = \frac{\tau_{\text{corr}}}{\Delta t} + \dot{\tau} \quad (1)$$

where τ_{corr} is a “correction” to bring the code phase to the navigation predicted position, and the $\dot{\tau}$ reflects navigation predicted rate. Δt is the time interval of the NCO command application (20 ms).

The correction term, also referred to as the NCO “poke,” is represented by:

$$\tau_{\text{corr}} = -\hat{\delta}t_R - \left[\frac{\hat{r}_{\text{nav}}}{c_{\text{light}}} + \hat{t}_{\text{atmos}} \right] + \hat{\delta}t_{\text{SV}} + \rho^* \quad (2)$$

where

$$\begin{aligned} \hat{\delta}t_R &= \text{user time bias estimate} \\ \hat{r}_{\text{nav}} &= \text{range-to-satellite estimate} \\ \hat{t}_{\text{atmos}} &= \text{atmospheric delay estimate} \\ \hat{\delta}t_{\text{SV}} &= \text{satellite clock bias estimate} \\ \rho^* &= \text{replica code pseudorange} \end{aligned}$$

The range term is calculated from navigation position, and the clock error is derived from the navigation filter. ρ^* is the receiver-supplied pseudorange.

It is instructive to see a derivation of this command. Navigation information may be used to calculate the time (referenced to the satellite clock) of transmission of a light pulse currently received, which is the calculated satellite signal code phase. This is:

$$\tau_{\text{calc}} = t_R - \hat{\delta}t_R - \left[\frac{\hat{r}_{\text{nav}}}{c_{\text{light}}} + \hat{t}_{\text{atmos}} \right] + \hat{\delta}t_{\text{SV}} \quad (3)$$

where t_R is receiver user time. The receiver sends a measured replica code pseudorange, from which the replica code phase may be calculated as:

$$\tau^* = t_R - \rho^* \quad (4)$$

The goal is to drive the replica code to a phase where, according to navigation and clock estimates, it would match the incoming code from the satellite. The alteration of code phase that accomplishes this is:

$$\tau_{\text{corr}} = t_{\text{calc}} - \tau^* \quad (5)$$

If Eqs. (3) and (4) are substituted into Eq. (5), the result is precisely Eq. (2).

The second term (also called the “push”) in the command is:

$$\dot{\tau} = 1 - \hat{\delta}t - \frac{\hat{r}_{\text{nav}}}{c_{\text{light}}} + \hat{\delta}t_{\text{SV}} \quad (6)$$

where

$$\begin{aligned} \hat{\delta}t &= \text{user time frequency error estimate} \\ \hat{r}_{\text{nav}} &= \text{range rate estimate (from navigation velocity)} \\ \hat{\delta}t_{\text{SV}} &= \text{satellite clock frequency error estimate} \end{aligned}$$

In the current DI configuration, the carrier NCO is also commanded by the push term derived above. This is sufficient to maintain the accuracy of the P code tracking, which is the primary information source for the PNS.

Note that these commands have the following effect: replica code is lined up with navigation prediction. As a consequence, the correlator information will make the navigation errors (including PNS clock error estimates) directly observable. This forced observability of navigation error in I and Q (in phase and quadrature) output is fundamental to deep integration.

Using the NCO commands to generate the replica code, the receiver produces I and Q integrated correlator outputs in the standard way. (See for example Ref. [3].) As shown in Figure 2, the receiver sends these I and Q data, integrated over 20-ms intervals, to the navigation medium rate function. At each time, these are indexed over the satellite set (N) and over the number of correlators, $T = 2K + 1$ (5 for PNS).

The navigation medium rate task compresses these by summing their squares over five time samples. Using i for the time index ($i = 1, \dots, 5$), k for the correlation index ($k = 1, \dots, T$), and suppressing the satellite (receiver channel) index, the measurement is:

$$dz_k = \frac{1}{5} \sum_{i=1}^5 [I_{i,k}^2 + Q_{i,k}^2], k = 1, \dots, T \quad (7)$$

For each 100-ms interval, this gives a T-element vector measurement (in contrast to conventional loops that form a scalar measurement, gaining local linearity at the cost of information). The vector measurement for one satellite for one 10-Hz filter pass is readily derived from standard equations for I and Q data giving:

$$dz_k = \frac{\delta t^2}{2} S^* R^2 (e - k\Delta) + b + n \quad (8)$$

where

- δt = 20 ms
- S = signal power
- R = pseudorandom code correlation function
- e = LOS delay error in chips
- Δ = correlator spacing = 0.5 chip
- b = bias
- n = noise

The bias and noise both derive from squaring the raw I and Q noise and equations for their distributions may be derived. The ideal correlation function is:

$$R(e) = \begin{cases} 1 - |e|, & -1 \leq e \leq 1 \\ 0, & \text{otherwise} \end{cases} \quad (9)$$

Finally, the LOS error is modeled as:

$$e = u \cdot \delta r + \delta b_a - \delta t_r \quad (10)$$

where u is a unit vector from the IMU to the satellite, δb_a is the residual atmospheric delay error, and δt_r is user clock residual error.

The DI filter first uses the dz measurements to estimate the signal-to-noise ratio (SNR), allowing for smooth adaptation to jamming or low signal strength. Then, the DI filter performs an update of the filter error state. The details of this update algorithm are omitted here. Since the measurement model is highly nonlinear due to the form of R and its square, common Kalman methods must be replaced by algorithms from nonlinear estimation theory. Further discussion is in Ref. [4].

The remaining arrow in Figure 2 shows the low to medium rate transfer of corrections. After all estimates are processed for one 10-Hz filter pass (all satellites, plus radar and altimeter measurements), the error state is used to calculate these corrections. At the end of the next 10-Hz interval, the navigation system incorporates these corrections in a reset. The following items are reset based on filter error states: position, velocity, quaternion, gyroscope, and accelerometer compensators, user clock error estimates, and LOS delay errors for satellites being tracked.

The two-rate scheme of Figure 2 is critical to the operation of DI GPS. The data from the filter are not sent directly to the receiver. Rather, the corrections go to

medium rate, and then indirectly affect NCO commands via the 10-Hz resets. The 50-Hz receiver control allows for tracking high-frequency dynamics in the correlators, while the lower rate filter execution allows for a more advanced estimation algorithm with more accurate estimates.

Clock Errors: Initialization and Reacquisition

Timing and clock errors are critical to deep integration.

The previous section indicated how the navigation filter kept up accurate clock error estimates while tracking satellites in deep integration. Two closely related problems are clock initialization and clock recapture after satellite signal loss.

Time is determined in navigation on the basis of high-speed interrupts from the Rockwell Collins receiver, referred to as t_{10} (10 ms apart) and t_{1000} (1 second apart). These are driven directly by the receiver oscillator.

Navigation time, or user time, is based directly on a count of t_{10} interrupts. The user clock bias and frequency errors are defined in speed-of-light units as:

$$\delta t_r = \text{user time} - \text{GPS time}$$

$$\delta \dot{t}_r = \text{user time frequency} - \text{true frequency}$$

For practical purposes, GPS time is considered perfect. True frequency is, in speed-of-light units, $1 + \text{Doppler}$. As seen above, estimates of these enter into navigation-issued NCO commands. From this follows the deep integration requirement: clock estimates must always be within about a chip (approximately 100 ft) of accuracy to retain code lock in deep integration.

Initialization: At initial operation, the receiver is in control of its NCOs, and the navigation software receives t_{1000} interrupts and messages with the matching GPS times. The navigation wrapper software does careful bookkeeping of these data over at least three low-rate passes (t_{1000} interrupts). From this, a linear relationship between user and GPS time can be determined algebraically. The data are then passed to the navigation algorithm, which in turn (after navigation initialization), issues a command to the receiver to accept host control.

Reacquisition: After a long period of time without visible GPS satellites, it was found that the receiver clock can drift nonlinearly to a point well outside the 100-ft accuracy requirement. An immediate return to DI updates would result in the loss of lock and poor performance of the PNS navigator.

An elementary solution based on a quick coarse clock recalibration was developed. The solution assumes that the time of GPS signal loss is sufficiently short so that the navigation position error has maintained relative accuracy (about 150 ft). This condition can be readily checked from filter variances. On return of signal power from one satellite, the navigation software calculates a candidate τ_{corr} (see Eq.(2)), but instead of sending it to the receiver as an NCO command, it replaces the current clock error estimate with this value. Likewise, a difference in two τ_{corr} calculations is assigned as clock frequency error. At the same time, filter variances are opened to indicate the coarseness of these estimates. At this point, the navigator again takes control of the NCOs, and subsequent filter passes allow for further refinement of clock and position errors.

For the PNS tests conducted in 2005, the position errors were well under 150 ft, thus supporting the validity of the algorithm described above. Draper is currently investigating methods to extend the clock correction to relax the restriction on small position error.

Doppler Radar

The Doppler radar sensors provide a three-dimensional velocity vector using short-range, low-power transceivers. The Doppler measurement is crucial to PNS in situations where GPS signals are unavailable, since it is the primary means (along with the altimeter) of damping position, velocity, and attitude drift inherent in the strapped-down navigation system. Tests have demonstrated that the Doppler allows for excellent performance indoors (with no GPS signals) for extended periods; furthermore, by keeping position errors bounded, it enables quick return to the GPS deep integration mode when satellite signals return.

There are three Doppler sensors nominally in an orthogonal frame (designated dopp), with the sensing axes aligned so that in normal walking motion, each will reflect a signal off the floor or ground. Each sensor outputs 512 measured amplitudes from the reflected signal over 0.1 s, providing 2 cm/s Doppler resolution. The data are sent to the 10-Hz navigation function, which shifts the raw signal to baseband, performs a fast Fourier transform, then applies the Doppler law to derive LOS velocity. This velocity is shifted to the IMU center, giving a final processed Doppler measurement from the triad of:

$$v^* = v^{\text{dopp}} + \delta v_{\text{doppler}} \quad (11)$$

This represents earth-relative velocity of the IMU center in the Doppler axis frame. The velocity is not instantaneous but an average over the 0.1-s interval of validity.

The measurement is linearized for a Kalman update for the navigation error states. The filter observation is calculated as:

$$z = \hat{C}_{\text{imu}}^{\text{dopp}} \hat{C}_e^{\text{imu}} \bar{v}_{\text{nav}}^e - v^* \quad (12)$$

The bar over the navigation velocity indicates an average over the interval of validity.

Finally, an error model for this measurement was derived by taking differentials. Showing only the most important terms, the resulting model is:

$$z = C_e^{\text{dopp}} [v^e \ x] \psi^e - C_e^{\text{dopp}} \delta v_{\text{nav}} + \text{error}_{\text{doppler}} \quad (13)$$

The error states in Eq. (13) are defined in Table 1. The Doppler error term consists of Doppler input axis misalignments (modeled by individual axis, not shown here) and discrete measurement noise.

The fact that Equation 13 employs Doppler coordinates, rather than ecef, has major advantages. In these axes the three scalar measurements can be modeled with independent noise, and the three scalar updates can be done sequentially. This allows skipping or performing updates on a sensor-by-sensor basis, in response to sensor output validity indicators. The power level output by the Doppler sensors is used for this purpose. If one or two Dopplers measure very low power, this is taken to indicate invalid axes; for example, an axis may be pointing to a very distant reflector or to infinity. If all three axes read low power and other sanity checks are met, this indicates a stand-still event, and a zero velocity update is executed instead.

Also note that the Doppler observation is a combination of velocity and attitude error, a consequence of the fact that it measures in a body-fixed frame, in contrast to GPS, which measures velocity in the earth-fixed frame. This can often create interesting results. For example, if GPS signals are strong and velocity is accurate, attitude can be improved by the Doppler. On the other hand, in a GPS-deprived scenario, attitude error can limit the improvement of navigation position accuracy.

SUMMARY

Results have shown that Draper's configuration of deep integration GPS combined with other sensors is a practical design for a personal navigator. This paper has illustrated the main features of the algorithm design.

ACKNOWLEDGMENT

This material is based on work supported by the U.S. Army/Natick Soldier Center under Contract No. DAAD16-02-C-0040 C 2005, The Charles Stark Draper Laboratory, Inc.

REFERENCES

- [1] Sherman, P., A. Kourepenis et al., "Personal Navigation for the Warfighter," JNC'05.
- [2] Gustafson, D. and J. Dowdle, "Deeply Integrated Code Tracking: Comparative Performance Analysis," 16th International Technical Meeting of the Satellite Division of the Institute of Navigation, Portland OR, September 2003.
- [3] Kaplan, E.D., *Understanding GPS: Principles and Applications*, Artech House, 1996.
- [4] Gustafson, D., J. Dowdle, and K. Flueckiger, "A Deeply Integrated Adaptive GPS-Based Navigator with Extended-Range Code Tracking," IEEE PLANS Conference, San Diego, March 2000.

(l-r) Peter Sherman,
Steven Holmes,
Dale Landis and
Tom Thorvaldsen



Dale Landis is a Principal Member of Technical Staff at Draper Laboratory. His specialties include estimation theory, navigation algorithms, and applied mathematics. He has contributed software for munitions, satellites, and

personal navigators. He received a Draper Distinguished Performance Award as a member of the team that first demonstrated the Draper deep integration algorithm on a GPS receiver; much of his recent work is aimed at the maturity and range of application of deep integration. Dr. Landis has a PhD in Mathematics from Lehigh University.

Tom Thorvaldsen is a Distinguished Member of the Technical Staff and Group Leader for Navigation and Localization. He has been responsible for the design, architecture, and data analysis of numerous inertial navigation systems. He is on two patents and has received two Distinguished Performance Awards. He has been at Draper Laboratory since 1975 and holds a BS in Electrical Engineering from New Jersey Institute of Technology and an MA in Mathematics from the University of Michigan.

Barry Fink is a Senior Member of Technical Staff at Draper Laboratory. He has been doing GPS work for 20 years. He has an MA in Mathematics from Boston University.

Peter Sherman is a Principal Member Technical Staff, Special Operations and Tactical Systems, at Draper Laboratory. He was Technical Director of the successful Personal Navigation System project and continues as TD to the PNS follow-on. Prior to coming to Draper, he worked at Kearfott Guidance and Navigation developing a tactical-grade inertial multisensor – a single-chip gyro and accelerometer – using MEMS fabrication techniques. Also at Kearfott, he led software/system development and integration teams for ring-laser gyro (RLG)-based IMU and GPS/INS products. He was an Integrated Product Team (IPT) lead for the Joint Direct Attack Munition (JDAM) navigation subsystem on a Lockheed Martin-Kearfott team. Dr. Sherman is a member of IEEE, received a BS (Hon) from the University of Michigan and a PhD in Chemistry/Chemical Physics from the University of Oregon where he held an IBM Corp. Pre-doctoral Fellowship.

Steven Holmes is a Senior Program Manager and currently leads Draper Laboratory's efforts to become a CMMI Maturity Level III organization. In the recent past, he led Draper's efforts to develop advanced ballistic and guided airdrop capabilities for the U.S. Army and Air Force, as well as efforts to develop a personal navigation system that provides accurate navigation information in a wide range of environments. He received a BS in Mathematics with a minor in Computer Science from Northeastern University (1987) and an MBA from Boston University (1994).

Error Sources in In-Plane Silicon Tuning-Fork MEMS Gyroscopes

Marc S. Weinberg, Anthony Kourepenis

Copyright © 2006 IEEE. Published in *Journal of Microelectromechanical Systems*, Vol. 15, No. 3, June 2006

abstract

This paper analyzes the error sources defining tactical-grade performance in silicon, in-plane tuning-fork gyroscopes such as the Honeywell-Draper units being delivered for military applications. These analyses have not yet appeared in the literature. These units incorporate crystal-line silicon anodically bonded to a glass substrate. After general descriptions of the tuning-fork gyroscope, ordering modal frequencies, fundamental dynamics, force and fluid coupling, which dictate the need for vacuum packaging, mechanical quadrature, and electrical coupling are analyzed. Alternative strategies for handling these engineering issues are discussed by introducing the Systron Donner/BEI quartz rate sensor, a successful commercial product, and the Analog Device (ADXRS), which is designed for automotive applications.

INTRODUCTION

The development of microelectromechanical systems (MEMS) inertial sensors offers revolutionary improvements in cost, size, and ruggedness relative to fiber-optic and spinning mass technologies.^{[1],[2]} Driven by high-volume commercial market needs, applications continue to grow for modest performing components at prices below \$10/axis. The Army is funding a \$100M initiative to realize producible, low-cost, tactical-grade MEMS inertial measurement units (IMUs) for gun-launched munitions and missile applications. The continued maturation of the technology will enable new applications and markets to be realized.

This paper analyzes design considerations necessary to reach tactical-grade performance in a silicon MEMS tuning-fork gyroscope (TFG) such as the Draper-based design that Honeywell is delivering in military systems. In the appendices, alternative strategies for handling these engineering issues are discussed by introducing the Systron Donner/

BEI quartz rate sensor, a successful commercial product, and the Analog Device (ADXRS), which is designed for automotive applications.

While many universities, government organizations, and companies have done research or even advertised the availability of inertial sensors, only a handful produces inertial instruments on a commercial scale. University of California, Berkeley,^{[3]-[5]} University of Sheffield, UK,^[6] University of Newcastle, UK,^[7] Seoul University, Korea, U. Neuchatel, Switzerland,^[8] the Massachusetts Institute of Technology (MIT), Tohoku University, Japan,^[9] Sandia,^[10] Integrated Micro Instruments,^[10] Cal Tech, Jet Propulsion Lab,^[11] University of California, Los Angeles (UCLA),^[11] National University of Singapore,^[12] University of Michigan,^{[13],[14]} Sagem,^[15] and many others have published on MEMS gyros. Three hundred sixty eight MEMS fabrication facilities have been identified worldwide.^[16]

The MEMS angular rate sensor or gyroscope divides itself into tactical and automotive/commercial performance categories. Two companies are producing tactical-grade performance on the order of 1 to 10 deg/h. Several are producing automotive grade, which is loosely defined as several hundred to a few thousand deg/h. The scarcity of commercial sources despite the plethora of research efforts and advertisements underscores the difficulty in constructing MEMS angular rate sensors.

Based on technology developed at Draper Laboratory, Honeywell is delivering HG1900, HG1920, and HG1930 navigation systems. After a decade of excellent test data, production quantities are now being realized. In 2004, several hundred systems were delivered for military applications, such as artillery shell and mortar shell guidance. Discussed further in the next section, this gyro is crystalline silicon-on-glass and has two mechanically-coupled proof masses moving in antiparallel directions, and senses rate in the wafer substrate plane.

Systron Donner/BEI has built hundreds of thousands of quartz TFGs over the past 15 years.^{[17],[18]} For their higher performance units, quoted specification sheet performance is 36 deg/h/√Hz noise, and uncompensated thermal sensitivities are 21 deg/h/°C and 300 ppm/°C. These sensors have been used in many higher performance automobiles for traction and stability control and in military systems.

Automotive or commercial-grade angular rate sensors perform at several hundred to a few thousand deg/h. Analog Devices' ADXRS150 specifies noise of 180 deg/h/√Hz and uncompensated thermal sensitivities of 1440 deg/h/°C and 1700 ppm/°C (typical values are 180 deg/h/°C and 150 ppm/°C). Analog employs polysilicon deposited over oxide sacrificial layers. Because of integrated on-chip electronics, these gyros are small and consume only 30 mW per axis.

Silicon Sensing Systems, a collaboration of BAE Systems and Sumitomo, sells an automotive gyro consisting of a MEMS ring resonator driven by magnetic fields. Delphi

pursued ring resonators for several years, but no information has been released in recent years. In their automotive products, Bosch has incorporated a rate sensor that can be purchased as a replacement part at BMW dealers. The sensor consists of two linear accelerometers supported in a vibrating frame.^[19] Bosch employs a 10-μm polysilicon process^[20] that results in gorgeous parts with straight smooth sidewalls.

For several dollars, Murata sells a vibrating beam gyroscope with a piezoelectric readout. Since stability is poor, high-pass filtering is recommended. This gyro has been applied to vibration control problems such as camera and camcorder stabilization. O-Navi (formerly Gyration) is selling sample quantities.^[21] Crossbow Technology and Cloud Cap Technology, Hood River, Oregon, deliver six-axis systems based on Analog Devices' inertial sensors.

Other gyro manufacturers include L-3, Panasonic, and Samsung.^{[22],[23]} Although mentioned on their web sites, little is known about these angular rate sensors. Imego, Sweden,^[24] produces small numbers of sensors. Kionix,^[25] Ithaca, NY, and Microsensors, a subsidiary of Irvine Sensors, advertise automotive-grade MEMS gyroscopes. SensoNor will ship their SAR10 automotive-grade angular rate sensor on short notice.^[26]

This paper's unique contributions include: 1) analysis and tolerances required to realize antiparallel tuning-fork motion; 2) two-degree-of-freedom model of instrument dynamics, including fluid and mechanical cross-axis couplings; 3) force and fluid coupling models, which dictate evacuated packages for better performance units; and 4) mechanical quadrature models that have led to laser trimming.

When discussing performance, most published work on MEMS angular rate sensors focused on z-axis gyros, which sense rate perpendicular to the substrate, and emphasized wide bandwidth resolution. For z-axis gyros, nonideal suspension geometries were studied in References [27] and [28]. More recently, the University of California, Irvine, has considered z-axis gyro scale-factor variation with frequency and temperature.^{[29],[30]}

DESCRIPTION OF HONEYWELL/DRAPER TFG

The Draper/Honeywell TFG is shown in Figure 1. This sensor was designed to achieve the highest performance consistent with costs that are low compared with traditional mechanical sensors. The gyro consists of two perforated proof masses supported by a system of suspension elements. The suspension and proof masses are doped crystalline silicon anodically bonded to a Pyrex or glass substrate at the suspension beam anchors and at the comb structures.^{[31],[32]} Curling from etch stop doping gradients is avoided by annealing silicon diffused with boron or by employing uniformly grown silicon-on-insulator. The glass substrate precludes on-chip electronics; however, the high resistivity reduces

stray capacitance, which mitigates the need for on-chip circuitry. (With silicon wafers, bond pads are isolated from the conducting substrates by thin dielectric layers so that high stray capacitance limits performance. With on-chip circuits, bond pads and stray capacitance are avoided.)

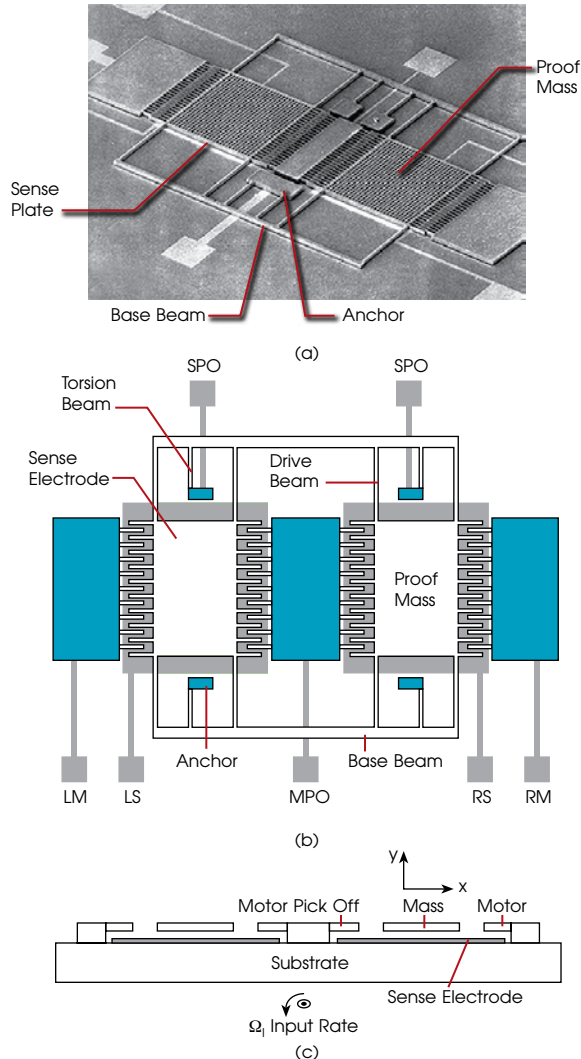


Figure 1. The Draper/Honeywell TFG mechanism. In 1(b) and 1(c), silver is metal, diagonal lines indicate silicon attached to glass, and white indicates suspended silicon. Electrical contact pads are right motor drive (RM), right sense electrode (RS), motor pickoff (MPO), left sense electrode (LS), left motor drive (LM), and sense pick off (SPO).

On either side of each proof mass are interdigitated combs.^[33] The outer combs (left and right motor in Figure 1) are used for electrostatically driving the proof masses antiparallel to the substrate in the x direction. The inner combs (motor pickoff in Figure 1) sense the drive motion and are typically biased to 5 Vdc through an op amp that senses charge traversing the comb gap. As described in “The Fundamental Dynamics of Oscillating Coriolis Sensors”

section, rotation about the in-plane z-axis induces Coriolis acceleration, which deflects the proof masses in opposite directions perpendicular to the substrate. Beneath the plates are deposited metal electrodes that are excited with dc voltages of opposite polarities. The right sense plate (RS in Figure 1) is typically excited with 5 V and the left sense plate (LS) with -5 V. Differential proof mass motion induces electrical currents in the structure that flow through the suspensions and sense pickoff (SPO, Figure 1) into a preamplifier whose input contains the input angular rate modulated by the drive frequency.

With drive resonant frequencies from 10 to 20 kHz, these gyroscopes are relatively stiff with suspension stiffnesses greater than 100 N/m. With 3- μ m gaps, mechanical spring force of 300 μ N is available to overcome sticking; nevertheless, care in etching and release, in electronic excitation, and mechanical handling is required.

As detailed below, the challenge is to obtain excellent performance in a device where the sensitivity to angular rate is small. Obstacles include manufacturing tolerances and the relatively large magnitudes of non-Coriolis forces and electrical drive and excitation signals.

MODE ORDERING

A first challenge is designing the angular rate sensor’s dynamic eigenfrequencies. If one considers the TFG proof masses (Figure 1) rigid and the suspension beams without mass, 3 rotations and 3 translations times 2 masses imply at least 12 dynamic modes. For advanced designs, proof mass compliance and suspension modes add further considerations. The TFG is designed so that the lowest frequency modes are generally: 1) drive or tuning fork, 2) translation, 3) sense, and 4) out-of-plane. In the tuning-fork mode, the proof masses move antiparallel to the substrate. One usually attempts to excite this mode through the electrostatic motor drive. Similar proof mass amplitudes are the design goal. The drive frequency is designed for 10-20 kHz to reduce vibration and acoustic effects. For the translation mode, the proof masses move parallel to the substrate. Because the drive combs are controlled to apply forces in opposite directions, translation should not be excited by electrostatic drive; however, translation is excited by linear acceleration. To ensure tuning-fork operation despite beam width tolerances, the in-plane translation frequency is usually set 10-15% or more away from the drive frequency.

The sense mode has the two proof masses moving away or toward the substrate in opposite directions. This could also be a rotation about their common center. For good gain, the sense eigenfrequency is set 5-15% away from the drive. While higher gain can be achieved at smaller separation, small variations in the resonant frequencies result in larger fractional changes of scale factor. When the out-of-plane mode is excited, the two proof masses move together perpendicular to the substrate. It is important that the lowest modes do not fall close to one another and that higher order modes are not integral multiples of the basic four.

Obtaining $\pm 2\%$ sense-drive frequency separation tolerance is challenging. The mechanical design is done using modal analysis in finite-element calculations. The tolerance required is estimated by noting that the beam mass is small compared with that of the proof mass. As a first approximation, stiffness is determined by beam bending (more detailed analyses include torsion elements) so that the sense resonant frequency depends on the beam thickness as $w^{1/2}t^{3/2}$, while the drive resonance depends on the beam width as $t^{1/2}w^{3/2}$. For a fixed thickness, the frequency separation is proportional to the beam widths. With greater detail, the frequency separation is still strongly determined by tolerances on the beam width and thickness. In the dissolved wafer process^[31] used for the Draper/Honeywell TFGs, the beam width and thickness are determined in independent steps. The thickness is determined by boron diffusion or by purchased silicon-on-insulator wafers. The beam widths are set by masks and deep reactive ion etching. Typical beam widths are 10 μm . Achieving 2% accuracy in frequency separation requires 0.2- μm absolute accuracy of the beam widths. This accuracy challenges the tolerances on masks and requires great control of deep etching.

Consider separation of the in-plane translation and drive or tuning-fork mode where the proof masses translate in parallel but opposite directions. Tuning-fork motion is desired to common mode reject in-plane linear accelerations and to reduce damping forces. With tuning-fork operation, the proof masses move in opposite directions so that the base beam (Figure 1) remains essentially stationary, and only small shear stresses are transmitted through the anchors to the substrate. With no anchors bending, energy is not transmitted or radiated to the substrate so that a high mechanical quality factor, a precursor to low force coupling (see next section), is attained. The tuning-fork eigenfrequency depends only on the suspension beams from the proof mass to the base beam (Figure 1). With only a single proof mass, acceleration near drive frequency would alter the proof mass velocity and appear directly as a scale-factor error in (4). For order of magnitude common mode rejection, the driven amplitudes of the two proof masses should match to 10%; that is, the common mode motion or translation mode should be 5% of the individual proof mass motion.

A lumped parameter, two-mass three-spring model for drive-translation motion is shown in Figure 2. Derived in Appendix A, the translation is related to the tuning fork or differential motion by:

$$\frac{\Sigma x(s)}{\Delta F(s)} = \left[\frac{-\frac{\Delta k}{2k}}{(s/\omega_H)^2 + 1} \right] \left[\frac{\Delta x(s)}{\Delta F(s)} \right] \quad (1)$$

where

- k = nominal stiffness of beam from proof mass to base beam
- Δk = stiffness deviation from nominal ($k_1 = k + \Delta k/2$,

$$k_2 = k - \Delta k/2)$$

Δx = differential proof mass motion ($x_1 - x_2$)

Σx = translation motion ($x_1 + x_2$)

ω_H = eigenfrequency of hula (in-plane translation) mode

ΔF = $F_1 - F_2$ = differential force (excites tuning-fork mode)

s = Laplace transform of $d/dt = j\omega_D$

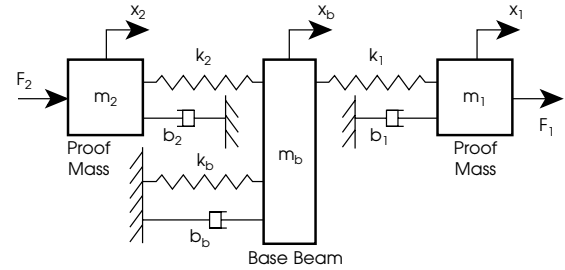


Figure 2. Lumped parameter model of in-plane dynamics.

Where the tuning-fork beams (from proof mass to base beam) largely determine the drive resonance, the translation mode also depends on the anchor beams (from anchors to base beam). Smaller differential stiffness and larger drive-translation frequency separation excites translation less. The stiffness depends on beam width cubed. Assume that the beam widths differ by 1% for the right and left proof masses, the differential stiffness is 3%. With the translation frequency 90% of the drive frequency, the translation motion is 6.4% of the tuning-fork motion. The beams must match to 0.1 μm (see earlier portion of this section). Achieving good separation often requires that the anchor beams be thinner than the tuning-fork beams. If the anchor beams are thick and rigid, the base beam is attached to the substrate and the proof masses move independently; that is, the drive and translation modes are identical. *These thin beams present challenges and often approach the limits of micromachining capability.*

FUNDAMENTAL DYNAMICS OF OSCILLATING CORIOLIS SENSORS

To understand TFG performance, consider a model that includes only the sense and drive modes. As shown in the previous section, the drive motion can often be considered separate from the translation (hula) modes. With only linear terms considered, the drive and sense axis dynamics are described by second-order spring-mass systems with coupling between modes:

$$\text{Drive} \quad (ms^2 + b_d s + k_d)x + [(b_{ds} - 2m\Omega_1)s + k_{ds}]y = F_d \quad (2)$$

$$\text{Sense} \quad [(2m\Omega_1 + b_{ds})s + k_{ds}]x + (ms^2 + b_d s + k_s)y = \alpha F_d \quad (3)$$

where

m = mass of one proof

d, s = subscripts that indicate drive and sense axes, respectively.

- b = damping $\sqrt{km/Q} = m\omega_N / Q$
- k = stiffness. Mostly mechanical with modifications by electrostatic forces
- k_{ds} = quadrature coupling. The drive axis suspension force coupling into the sense axes
- b_{ds} = in-phase damping ‘surfboard’ coupling to sense axis
- x = motion along drive axis (parallel to substrate)
- y = motion along sense axis (normal to substrate)
- s = Laplace transform of d/dt
- F_d = motor drive force applied by the outer combs in Figure 1
- Ω_1 = slowly varying input rate
- α = drive force coupling to sense axis
- Q = quality factor

From (2) and (3), another challenge emerges. The driving force as well as the drive axis suspension force and drive axis damping are coupled into the sense axis. With good design, these forces should be small compared with the Coriolis Force $2m\Omega_1\dot{x}$.

For low-frequency angular rate inputs, the desired output is the angular rate modulated by the drive frequency. As shown in the electrical circuit of Figure 3, the proof masses are the negative input of a high input impedance, high-gain operational amplifier whose input node is at virtual ground. The feedback resistor is large so that it does not affect the output at the gyro’s drive frequencies. From (3) and Figure 3, the preamplifier output is given by (Appendix B):

$$V_o(t) = \left(\frac{2\Omega_1\omega_d x_o \sin(\omega_d t + \theta) - \frac{F_s(t)}{m}}{\omega_s^2 - \omega_d^2} \right) \frac{dC_s}{dy} V_s + \frac{\Sigma C V_N(t) - C_c V_c(t)}{C_{fb}} \quad (4)$$

where

- V_o = output of preamplifier
- V_s = bias voltage (plus and minus applied to right and left sense plates in Figure 1) on sense electrodes (5 V, example values are given in parentheses)
- V_c = coupling (drive feedthrough)
- V_N = preamplifier input voltage noise (10^{-8} V/ $\sqrt{\text{Hz}}$)
- C_{fb} = feedback capacitor about the sense axis preamplifier (2 pF)
- C_s = total of sense capacitors (2 pF)
- C_N = preamplifier input capacitance to ground (5 pF)
- C_c = coupling (undesirable capacitor) to virtual ground (preamplifier input)

- dC_s/dy = differential change of sense capacitors with y motion (2 pF/3 μm)
- ΣC = sum of all capacitors attached to the virtual ground. Includes strays, working, feedback, and amplifier capacitors (12 pF).
- ω_d = drive mode undamped natural frequency $\sqrt{k_d/m}$ (20 kHz \times 2 π rad/s)
- ω_s = sense mode undamped natural frequency $\sqrt{k_s/m}$ (22 kHz \times 2 π rad/s)
- x_o = amplitude of drive motion (10 μm zero-to-peak)
- F_s = cross coupling forces acting along the sense direction (B-6)
- θ = phase shift through sense dynamics (B-6)

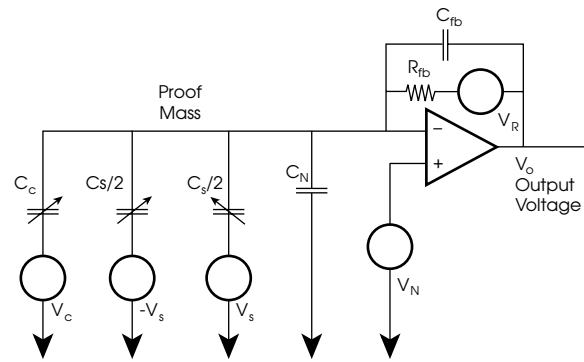


Figure 3. Circuit diagram for sense preamplifier analysis.

In (4), it is assumed that the proof mass motion is driven so that the displacement is a sinusoidal function of time. The rate signal, the Coriolis term, is in phase with the proof mass velocity, i.e., in quadrature with the proof mass position. For the sample parameters above, the gyro scale factor at the preamplifier output is 1.3 mV/rad/s. With a field effect transistor (FET) preamplifier whose input noise at drive frequency is 10 nV/ $\sqrt{\text{Hz}}$, the rate equivalent noise is 10 deg/h/ $\sqrt{\text{Hz}}$. *Attaining the theoretical noise limit is a challenge* discussed further in the ‘Electrical Coupling’ section.

Because of the sense-drive frequency separation and high sense-axis quality factor, the damping term is omitted in the denominator of (4); therefore, gain does not depend on damping. High resonant frequencies are desired to remove the gyro’s sensitive frequencies from acoustic noise and vibration and to permit isolators that allow adequate bandwidth. For a fixed sense-plate bias, higher sensitivity is achieved by lowering the resonant frequencies and/or by decreasing the separation between sense and drive mode. Drive frequencies of 10-25 kHz and sense-drive mode separations of 5-15% have worked well for MEMS TFGs. At baseband, the transfer function of output voltage to rate input has a lightly damped peak at the frequency separation. Placing the separation at 1-2 kHz allows a 100-Hz bandwidth, which adequately filters

the undamped peak. If the frequency separation is small, the scale factor becomes sensitive to small variations in resonant frequencies (4).

Demodulation (Figure 4) multiplies the output (4) by $\sin(\omega_d t + \varphi)$, a signal in-phase with the drive velocity. The output after demodulation and low-pass filtering is (Appendix B):

$$V_D(t) = G_{ac} \left\{ \begin{aligned} & \left[\frac{-\Omega_1 \omega_d + \frac{(\alpha b_d - b_{ds}) \omega_d}{2m} + \frac{k_{ds}}{2m} (\varphi - \theta)}{\omega_s^2 - \omega_d^2} \right] x_o \omega_d \frac{dC_s}{dy} V_s \\ & + \frac{\text{dem}[V_N(t) \Sigma C - C_c(t) V_c(t)]}{C_{fb}} \end{aligned} \right\} + V_B \quad (5)$$

where

G_{ac} = gain before the demodulator

V_B = bias voltage in dc section often caused by amplifier offset voltages.

dem = demodulation operation. Frequencies near the demodulation frequency are transferred to base-band by the $\sin(\omega_d t + \varphi)$ demodulation

φ = small phase shift between rate signal in sense chain and demod reference

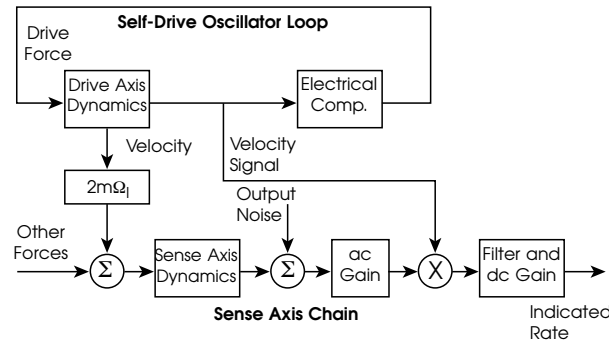


Figure 4. TFG electrical block diagram.

In (5), small angle approximations for the angles θ and φ were applied. The ac gain, typically 5-20 V/V, and the low-pass filtering blocks are shown in Figure 4. This low pass filter, typically 50-100 Hz, sets the gyro's bandwidth. Feedthrough terms (5) are extremely important. The demodulation function *dem* emphasizes that extra voltages in phase with drive velocity appear directly as dc bias errors in the TFG. Components in quadrature to drive velocity are greatly reduced at the dc output; however, mechanical and electric phase shift error causes quadrature terms to appear as in-phase bias. Individual challenges and their implications on gyro construction are discussed in the next section.

ERROR MECHANISMS

Force-Related Errors – The Impetus for Evacuation

Vacuum packaging is needed to reduce the required motor force and the voltage required to drive the motor. From (3), the motor force couples into the sense axis. For reasonable scale factor, large drive amplitude is desired so that the drive axis is operated at resonance; that is, the motor force is in phase with the drive velocity. When the interdigitated combs are over a ground plane, lift forces are exerted.^[33] Derived in Appendix C, the erroneous estimated angular rate can be calculated from:

$$\hat{\Omega}_1 = \alpha \frac{\omega_d}{2Q_d} \quad (6)$$

For a single set of combs, the coupling coefficient α is of the order of 0.3.^[33] Because the left and right motors behave similarly, this is common mode coupling. Since both outer combs cause lift and since the sense plate excitation is selected to detect differential motion, the differential coupling determines the gyro bias. The coupling coefficient depends strongly on vertical misalignment (the disengagement) of the moving and stationary combs.^[33] With a 20-kHz drive frequency and 100,000 quality factor, the erroneous common mode angular rate is 0.2 rad/s. The differential magnitude is typically an order of magnitude smaller. Because damping changes by a factor of three over operating temperature, thermal compensation is usually employed; nevertheless, the absolute tolerances and stability of the comb disengagements must be held very closely to achieve tactical performance.

In addition to the electrostatic force coupling, hydrodynamics couple drive force into sense force. Described by lubrication theory, the fluid coupling is described in detail with closed-form solutions in Reference [34]. Once the coupling coefficient is calculated, (6) can be used to estimate the impact on estimated angular rate. Evacuation and pressure relief holes are required for acceptably low effects on in-phase bias. Perforated designs such as Figure 1 result in hydrodynamic lift that is smaller than the electrostatic coupling. The perforations also assist cleaning and inspection.

The random motion of the proof mass is dictated by Brownian motion. To achieve preamplifier limited performance, gas damping must be reduced by evacuation so that the principal damping is material and radiation through the anchors into the glass.

Even if a vacuum is not required (as in an accelerometer), the small gaps and masses dictate hermetic sealing since humidity variation causes unacceptable variations in scale factor because of effective gap change. As temperature changes even with hermetic sealing, outgassing deposits material and changes the sense and motor gaps so that the scale factor is changed.

To summarize, evacuation is required in high-performance gyros for the following reasons: 1) reduce the electrostatic

drive force and, hence, coupling into sense axis force; 2) reduce hydrodynamic lift (surfboarding) effects; 3) maintain acceptable phase stability between sense and drive axes (the omitted damping in the denominators of (4) and (5)); 4) render Brownian motion small so that wide bandwidth resolution is achieved; and 5) enhance resolution since low damping does not restrict sense-axis motion in (4) and (5).

Low damping increases proof mass motion if shocks are applied. These effects are reduced by the two-mass design, which rejects common mode inputs, and modal frequency selection. The high resonant frequencies are above most shock spectra, which are often defined to a few kilohertz. With high resonant frequencies, shocks and acoustic inputs are reduced by suspension isolating the IMU. The sense axis baseband peak, which occurs at the drive-sense separation, typically 10 kHz, is greatly reduced by sense chain low-pass filtering.

Mechanical Quadrature

The drive axis is operated at resonance so that the stiffness and inertial forces in (2) cancel and the drive-axis response is dominated by damping; nevertheless, a relatively large spring force is being exerted. Because of manufacturing imperfections or tolerances, the mechanical stiffness force results in the cross-coupling term k_{ds} . A slender beam tries to bend along its principal axes of inertia.^[35] If the principal inertias are not aligned with the drive and sense axes, an attempt to bend the beams in the x direction results in a y force. Consider the cross section of a simple suspension beam where the sidewalls are not cut vertical but at an angle θ to form a parallelogram cross section as shown in Figure 5. For small sidewall angles θ , the ratio of cross-coupling to in-plane force is given by:^[36]

$$\alpha_Q = \frac{k_{ds}}{k_d} = \frac{t^2}{w^2} \theta \quad (7)$$

where

t = thickness of suspension beams and proof mass as defined in Figure 5

w = nominal beam width as defined in Figure 5

θ = tilt of sidewalls

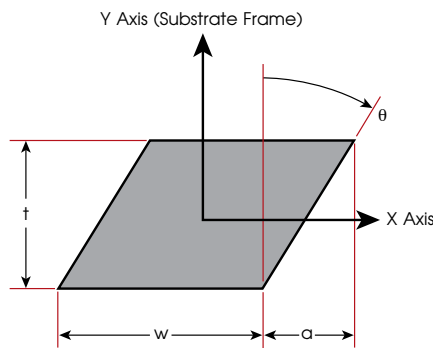


Figure 5. Nomenclature for analyzing quadrature from beam sidewall angle.

Because the suspension consists of several beams rather than a simple cantilever, the mechanical quadrature is 3-10 times smaller than that calculated by (7). Equating the Coriolis term to the cross-coupled term as in Appendix C, the estimated input rate error from cross coupling is given by:

$$\hat{\Omega}_Q = \alpha_Q \frac{\omega_d}{2} \quad (8)$$

Because the coupling is in-phase with drive position, the cross-coupled force term is in quadrature with the desired rate signal. With good demodulation (see “Mode Ordering”), little quadrature should appear in the indicated rate output. In a typical TFG, $t/w = 2$. Because of the two proof masses, the differential coupling between right and left masses is the principal concern. With sidewall slopes matched to 0.002 r (0.1 deg), a tight tolerance for vertical deep etching in silicon, the coupling ratio α_Q is 0.008 and the magnitude of the quadrature signal (8) is 502 rad/s (10^8 deg/h). *For tactical performance, the sheer magnitude of the possible quadrature signal presents major design challenges.* In addition to dynamic range, small variations in demodulator phase lead to unacceptable bias shifts.

The TFG handles quadrature by very careful micromachining and by applying a quad nulling loop^[37] to reduce the quadrature signal injected into the sense channel. As shown in Figure 4, the sense axis output is demodulated into components in-phase and in quadrature with the desired input rate-drive velocity signal. The sense chain quadrature signal is nulled by applying a dc voltage bias to the drive combs in addition to the two frequencies motor drive. Because of limited available voltage, mechanical quadrature must be less than 50 rad/s for successful quad nulling. Because of the nulling loop, the sense chain does not require head room for the large mechanical quadrature. High-performance or as-etched quadrature larger than 50 rad/s requires mechanical trimming, a procedure described in Reference [36]. The difficulty of quadrature is that small imperfections lead to large quadrature; however, only small amounts of material must be removed for effective trimming.

Electrical Coupling

The drive voltages are typically 5 V. From (4) or (5), 100 fF ($C_c = 10^{-13}$ F) stray capacitance to the sense node results in an output voltage of 250 mV, equivalent to 200 rad/s (4×10^7 deg/h). Small coupling capacitance can lead to a sense change signal much larger than the desired angular rate resolution and to dynamic range issues. This coupling effect is mitigated by two-frequency operation and balanced drive. The coupling can occur at the combs or in the leads leading to the package or even in the electronics itself.

For an electrostatic drive, the force is proportional to the voltage squared; thus, the drive force could be at the difference frequency between two input voltages.^[37] Because the two frequencies can differ from the drive frequency

at which demodulation is done, coupling effects from the motor to the sense are greatly reduced (5). Because the half frequencies are generally derived from the motor position signal, the motor drive must be designed carefully to make motor frequency signals small.

Voltage squaring allows the motor to be driven with plus and minus voltages, which reduce the coupling into the sense chain. Because of amplitude mismatch (see “Mode Ordering”), the voltages must cancel for each proof mass so that layout and connections become more complicated. A bias is added to the motor drives to null mechanical quadrature signals and charge injected by the motor pickoff.

For proper operation, the motor drives must also be isolated from the motor sense so that the drive oscillator loop locks onto the mechanical motion and not onto the half frequency signals. *Considerations of dynamic range, motor loop oscillator, and stability dictate that capacitance be matched to 10 fF; a significant design and manufacturing challenge.* This figure is supported by simulation and results of production units.

CONCLUSION

For TFGs, the phenomena that cause the principal errors in estimating angular rate were evaluated. To realize a working MEMS gyroscope, many design features must be done correctly. Design teams must converge quickly to a feasible solution or have sufficient resources to afford several iterations. The challenges overcome in realizing a high-performance MEMS gyro included: 1) geometric tolerances, 2) attaining theoretical noise limits, 3) vacuum packaging, 4) reduction of mechanical quadrature, 5) eigenfrequency location, 6) electrical coupling, and 7) thermal expansion effects. Precise suspension beam dimensions were required to maintain the desired ordering of modes and frequency separation to achieve beam symmetry for reasonable quadrature and to maintain comb disengagement, which causes vertical forces. Achieving acceptable quadrature required mechanical trimming and electrical feedback. Reaching theoretical noise limits required careful, symmetric layout of electrical leads, of electronics, and of the sensor itself to avoid coupling through unbalanced stray capacitance. Thermal expansion changes dimensions that change gyro performance; for example, comb engagement alters sense axis force, and, hence, instrument bias, and sense gap alters scale factor. Alternatives for overcoming the above challenges are presented by introducing the Analog Devices and BEI angular rate sensors.

Draper used the considerations and analyses presented here in developing the TFG technology Honeywell has applied to its navigation systems. After a decade of excellent test data, production quantities are now being realized. In 2004, several hundred systems were delivered for mainly military applications, such as artillery shell and mortar shell guidance. Gyro noise is 5-10 deg/h/√Hz with bias and scale factor repeatability over temperature and

turn off better than 30 deg/h and 400 ppm, respectively. Raw, uncompensated thermal sensitivities are 10 deg/h/°C and 250 ppm/°C.

APPENDIX A. DERIVATION OF TRANSLATION MODE FROM DIFFERENTIAL FORCE

The relation for translation mode versus differential mode (1) is derived. From Figure 2, consider only motion parallel to the substrate. Neglect damping and apply Newton's law to proof masses 1 and 2 and to the base beam:

$$F_1 = m_1 s^2 x_1 + k_1 (x_1 - x_b) \quad (A-1)$$

$$F_2 = m_2 s^2 x_2 + k_2 (x_2 - x_b) \quad (A-2)$$

$$0 = (m_b s^2 + k_b) x_b - k_1 (x_1 - x_b) - k_2 (x_2 - x_b) \quad (A-3)$$

where

k = stiffness of extension spring

m = mass

x = displacement of mass

1,2,b = subscripts indicating proof mass 1, proof mass 2, or base beam

s = Laplace transform of d/dt = jω_D

Add (A-1) and (A-2) to obtain the translation equation:

$$\Sigma F = (ms^2 + k)\Sigma x + \frac{(\Delta ms^2 + \Delta k)}{2} \Delta x - 2kx_b \quad (A-4)$$

where

Δk = stiffness deviation from nominal (k₁ = k + Δk/2, k₂ = k - Δk/2)

Δm = mass deviation from nominal (m₁ = m + Δm/2, m₂ = m - Δm/2)

Δx = differential proof mass motion (x₁ - x₂)

Σx = sum of translation motion (x₁ + x₂)

ΔF = F₁ - F₂ = differential force (excites tuning-form mode) usually applied by electrostatic comb drive

ΣF = F₁ + F₂ = sum of forces (excites translation). Loads caused by substrate acceleration along the drive direction are included here.

Subtract (A-2) from (A-1) to obtain the differential drive mode equation.

$$\Delta F = \frac{(\Delta ms^2 + \Delta k)}{2} \Sigma x + (ms^2 + k)\Delta x - \Delta kx_b \quad (A-5)$$

With perfect construction, the translation (A-4) includes the base motion while the differential motion (A-5) is free of base motion. Reorder (A-3).

$$0 = -k\Sigma x - \frac{\Delta k}{2} \Delta x + (m_b s^2 + k_b + 2k)x_b \quad (A-6)$$

With a large number of teeth, the differential drive force is much larger than the sum. The base beam mass is much

less than the proof masses. Therefore, set m_b and ΣF to zero and solve (A-4) through (A-6) simultaneously for Σx , Δx , and x_b .

$$\frac{\Sigma x(s)}{\Delta F(s)} = \left[\frac{-\frac{\Delta m s^2}{2m\omega_H^2} - \frac{\Delta k}{2k}}{(s/\omega_H)^2 + 1} \right] \begin{bmatrix} \Delta x(s) \\ \Delta F(s) \end{bmatrix} \quad (\text{A-7})$$

where ω_H = eigenfrequency of hula (in-plane translation) mode

$$= \sqrt{\frac{kk_b}{m(k_b + 2kt)}} = \omega_d \sqrt{\frac{k_b}{k_b + 2k}}$$

$$\omega_d = \text{drive frequency} = \sqrt{k/m}$$

Because of their larger lateral dimensions, proof masses match more closely than the spring stiffnesses; therefore, Δm in (A-7) was set to zero to obtain (1).

APPENDIX B. DERIVATION OF SENSE PREAMPLIFIER OUTPUT

The sense axis preamplifier output (4) and the demodulated output (5) are derived. Solve (2) and (3) simultaneously for the drive and sense axis positions x and y . Assume that fluid and suspension cross couplings b_{ds} and k_{ds} , the Coriolis coefficient $2m\Omega_1$, and the force coupling α are small. Because motion is driven by small terms, the sense position becomes a small term. Neglecting the products of small terms, the drive and sense positions are determined by:

$$\frac{x(s)}{F_d(s)} = \frac{1}{ms^2 + b_d s + k_d} \quad (\text{B-1})$$

$$y(s) = \frac{\alpha F_d - [(2m\Omega_1 + b_{ds})s + k_{ds}]x(s)}{ms^2 + b_s s + k_s} \quad (\text{B-2})$$

where s = Laplace transform of time derivative d/dt

Because the drive oscillator loop requires that the drive loop operate at resonance, the drive position and force are sinusoids once steady-state operation is achieved; that is:

$$x(t) = x_o \cos(\omega_d t) \quad (\text{B-3})$$

$$F_d(t) = -b_d x_o \omega_d \sin(\omega_d t) \quad (\text{B-4})$$

Since the sense mode resonant frequency is typically 10% different from the drive resonant frequency, the damping can often be neglected in determining the steady-state sense position magnitude. Solve (B-2) with (B-3) and (B-4).

$$y(t) = \frac{(2m\Omega_1 + b_{ds} - \alpha b_d) x_o \omega_d \sin(\omega_d t + \theta) - k_{ds} x_o \cos(\omega_d t + \theta)}{-m\omega_d^2 + k_s} \quad (\text{B-5})$$

where

$$\theta = \text{phase shift through sense dynamics}$$

$$= -\tan^{-1} \left(\frac{\omega_d b_s}{k_s - m\omega_d^2} \right)$$

The hydrodynamic lift and the drive force coupling are in-phase with the desired rate signal, while the suspension force coupling is out of phase. The sense position (B-5) can be written as:

$$y(t) = \frac{2\Omega_1 \omega_d x_o \sin(\omega_d t + \theta) - \frac{F_s(t)}{m}}{\omega_s^2 - \omega_d^2} \quad (\text{B-6})$$

where

$$F_s = \text{force acting in sense direction}$$

$$F_s = (\alpha b_d - b_{ds}) x_o \omega_d \sin(\omega_d t + \theta) + k_{ds} x_o \cos(\omega_d t + \theta)$$

The sense preamplifier output is determined from the circuit diagram of Figure 3. The sense plates below the proof masses are biased with opposite voltages (Figure 1) so that antiparallel vertical motion is detected. Because of the amplifier's high gain, the preamplifier input, which is wired directly to the proof masses, is at virtual ground. Because the feedback resistor R_{fb} is large, the resistor and its Johnson noise are small effects at the gyro drive frequency ω_d .

$$V_o(t) = \frac{-V_s \frac{\partial C_s}{\partial y} y(t) + \Sigma C V_N(t) - C_c(t) V_C(t)}{C_{fb}} \quad (\text{B-7})$$

Inserting (B-6) into (B-7) yields (4). Demodulation (Figure 4) multiplies the output (4) by $\sin(\omega_d t + \varphi)$, a signal in-phase with the drive velocity. High-frequency content is removed by low-pass filtering so that the output after ac gain and demodulation is described by (5), which includes a bias voltage from amplifier offsets in the dc chain.

APPENDIX C. DERIVATION OF IN-PHASE BIAS ERROR FROM FORCE COUPLING

Equation (6) for calculating the in-phase bias caused by force coupling is derived. Since the TFG is operated at the drive resonance, the drive force amplitude on one proof mass is given by:

$$F_d = \frac{m\omega_d^2 x_o}{Q_d} \quad (\text{C-1})$$

To calculate the angular rate errors, the undesired sense axis forces F_s are compared to the Coriolis acceleration $2m\Omega_1 \omega_d x_o$; that is, the estimated rate is calculated from:

$$\hat{\Omega}_1 = \frac{F_s}{2m\omega_d x_o} \quad (\text{C-2})$$

The undesired force is the drive force multiplied by the coupling coefficient α_F . Inserting αF_d from (C-1) into (C-2)

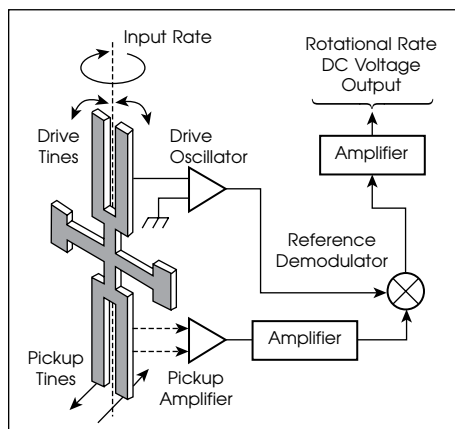
results in (6). Because both the coupled and Coriolis forces act on the sense axis dynamics, the frequency separation denominator of (4) does not appear in (C-2).

Appendix D. IN-PLANE QUARTZ GYROSCOPE

The quartz rate sensors (QRS) reached the market in the late 1980s, a decade before silicon MEMS devices were developed. The QRS has been a very successful product; therefore, a comparison with silicon TFGs is instructive. A typical Systron Donner/BEI QRS is shown in Figure 6. Per References [17] and [18], the actual designs differ depending on applications, which range from tactical to automotive. The H-shaped sensing mechanism is made of piezoelectric quartz, a significant variation from the electrostatically silicon gyros. Electrodes are deposited so that the upper tines are driven as a tuning fork with antiparallel motion in the substrate plane. Because of symmetric construction and mechanical coupling, the lower tines oscillate at the drive frequency, although they are not excited electrically. When the substrate is rotated about an axis parallel to the tines (Figure 6), the drive tines move into and out of the plane in response to the Coriolis acceleration, deflections that are coupled into the lower, sense tines. The sense electrodes are designed, deposited, and wired to sense the out-of-plane sense motion.



(a)



(b)

Figure 6. BEI quartz rate sensor: (a) sensing mechanism, (b) schematic of operation.^[18]

Because of the piezoelectric material, drive and detection signals are at the same frequency for constant rate inputs, and gaps around the moving elements are much larger than the 1-4 μm typical of the electrostatically-driven devices. Silicon micromachining's deposition, doping, and wafer bonding techniques are not available in quartz; therefore, quartz parts are generally limited to wafer thickness, which is greater than 100 μm (silicon parts are 5-20 μm thick or several hundred micron).

The greater thickness and the required proximity of in- and out-of-plane eigenfrequencies results in moving elements larger than those of the silicon MEMS devices. Drive oscillation at 9 to 17 kHz dictates the length of the tines, while the continuous beams and the number of tines dictate that the tines and tip masses must be shaped carefully.^[18] Because the wafers are 100 μm thick, the wafers are much smaller than those used in silicon processing. The combination of small wafers and large die tend to make the projected QRS costs higher than those for silicon rate sensors. Because of the thick part and large air gaps, sticking should not be an issue for the QRS. Because of the thicker parts and larger gaps that result in lower damping, it is possible that the QRS can be sealed at higher pressures than the TFG and still demonstrate low Brownian motion noise.

The quartz's etching characteristics are not as controlled as those of silicon because of the fundamental nature of quartz crystallographic properties and the etchants. The etching results in sidewalls (see "Error Mechanisms: Mechanical Quadrature") that require each part, including automotive, be trimmed.^[18] Trimming has been done by the addition of mass and by laser removal, a process that has been highly automated. For high-performance sensors, the level of quadrature trimming is suspected to be quite tight because the linear piezoelectric drive does not offer the possibility of quadrature nulling discussed in the "Error Mechanisms: Mechanical Quadrature" section.

With piezoelectric operation, both the drive signals and the sense output are at the same frequency for no rate input. In electrostatically operated silicon devices, the drive voltages can be at different frequencies from the sensed output (see "Error Mechanisms: Electrical Coupling"). For the QRS, the sense and drive electrodes are physically separated in the H structure so that coupling within the sensor should be small; nevertheless, controlling stray capacitance is challenging. BEI has demonstrated proprietary electronics^[18] that enable tactical performance so that other stray paths have been controlled.

Appendix E. ANALOG DEVICES OUT-OF-PLANE GYROSCOPES

Analog Devices began their gyro development with the ground rules that the instrument should be inexpensive but should satisfy automotive applications. To minimize expense, Analog's accelerometer CMOS and polysilicon

process was mandated. In the mid-1990s, the process focused on 2- μm thick suspended parts. Based on performance considerations, Analog has moved to 4- μm thick suspended polysilicon parts.^[38] The 4- μm thickness results in smaller moving parts, shorter beams, and smaller deflections than for the larger TFGs. To incorporate on-chip circuitry, the substrate must be silicon. The moving elements, wire runs, and bonding pads are isolated from the conducting silicon substrate by an oxide layer.

As shown in Figure 7, the gyro mechanism consists of two independent mechanical structures.^[38] For each structure, the inner member is driven and sensed electrostatically. The sensing frame supports the driven member. An angular rate about an axis perpendicular to the substrate moves the driven mass along the sense direction (Figure 7), which is parallel to the substrate plane. As discussed below, the suspension is

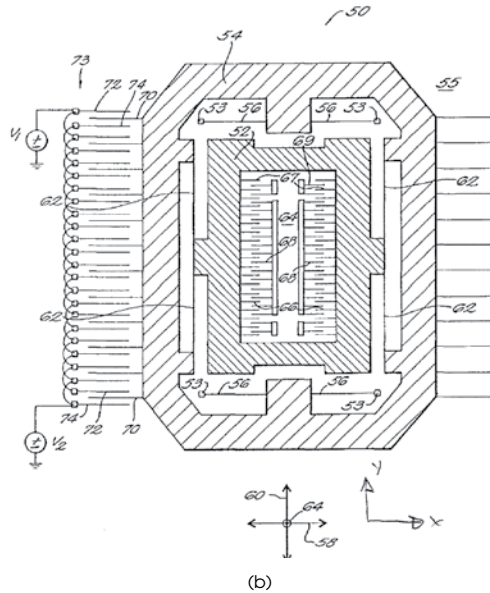
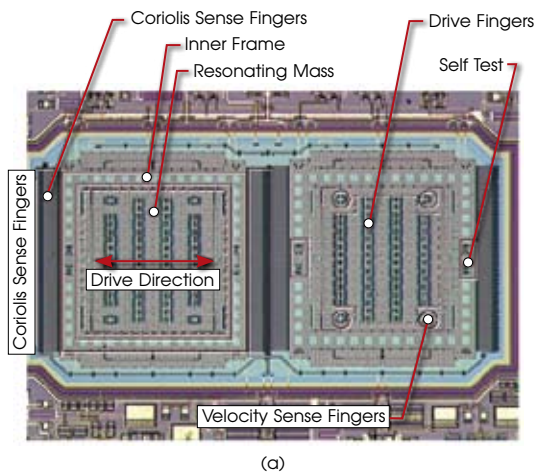


Figure 7. Mechanism for Analog Devices ADXRS angular rate sensor: (a) photomicrograph,^[41] (b) sketch of one proof mass assembly.^[42]

designed so that the sensing frame does not move in the drive direction, but follows the proof mass in the sense direction. Electrostatic combs detect the frame position.

Eliminating trimming to reduce quadrature was a dominant decision in ADXRS design.^{[38]-[42]} With crab leg or folded beam suspension, different beam stiffness can cause sense-axis motion when driving the proof mass.^[40] Because this motion is in phase with position, it is in quadrature to the desired rate-induced motion. The ADXRS beam widths are 1.7 μm , and width tolerances are 0.2 μm so that quadrature reduction was a major design goal.^[38] Straight beams between the sense and drive elements (Figure 7) result in very little sense-axis motion. The beams have stress relief at their ends (not shown in Figure 7) to reduce longitudinal stresses from polysilicon thermal expansion and from drive motion. Although Analog has not employed it, a fine quadrature trim is possible by fingers excited to exert a sense force that is modulated by the drive motion.^[43]

In the ADXRS, both the sense and drive motions are parallel to the substrate's plane; thus, all critical dimensions are done in one masking and etching operation. If the polysilicon thickness is off, all frequencies move together so that mode ordering is maintained. While the proof mass is driven at 7- μm amplitude, the sense motion for angular rate is roughly 10^{-10} m/rad/s,^[38] an order of magnitude lower than for TFGs. This smaller motion is attributed to smaller drive amplitude, the fact that the drive mass must also drive the additional sense mass, and 20 to 30% separation of sense and drive resonant frequencies. The greater separation is consistent with 2- μm beam width compatible with 4- μm thickness and the resulting proof mass and suspension dimensions.

The gyro consists of two mechanically independent mechanisms (not tuning forks, see "Mode Ordering" section) whose drive frequency is roughly 15 kHz and whose quality factor is 45.^[38] The units are electrically cross-connected^[42] so that the proof masses move antiparallel to common mode reject linear acceleration. To achieve common mode rejection with a Q of 45, the two drive resonant frequencies should be within 1% of each other.

If the moving drive teeth are not centered with respect to the stationary teeth (i.e., the entire proof mass is moved relative to the stationary combs), a large coupling to drive force results. The coupling of drive force to sense-axis effects are described in (3). Since the drive force is large because of the high damping and since the drive force is in phase with the drive velocity and, hence, the Coriolis acceleration, the proof mass must be centered to very tight levels.

With 1.7- μm wide beams, achieving the geometric control for sense drive frequency separation, matching drive frequencies, and centering the combs is challenging.

The ADXRS is hermetically sealed at 1 atmosphere. Because of the resulting damping, noise is limited by Brownian motion.^[38] To achieve drive amplitude, the 5-V supplies must be boosted to approximately 12 V. Damping adds phase shift between sense and drive axes. Electronics design and increasing separation between sense and drive frequencies reduce the effect of this additional phase shift. The resulting damping renders the ADXRS tolerant of operating shock.

The ADXRS relies heavily on its on-chip electronics to overcome the small size and low scale factor of the mechanical parts. The sense displacement per rate input is 10% and the capacitance variation is 1% of the 20- μm thick TFGs. Analog measures displacement resolution similar to the TFGs, but with much smaller capacitors.

Acknowledgments

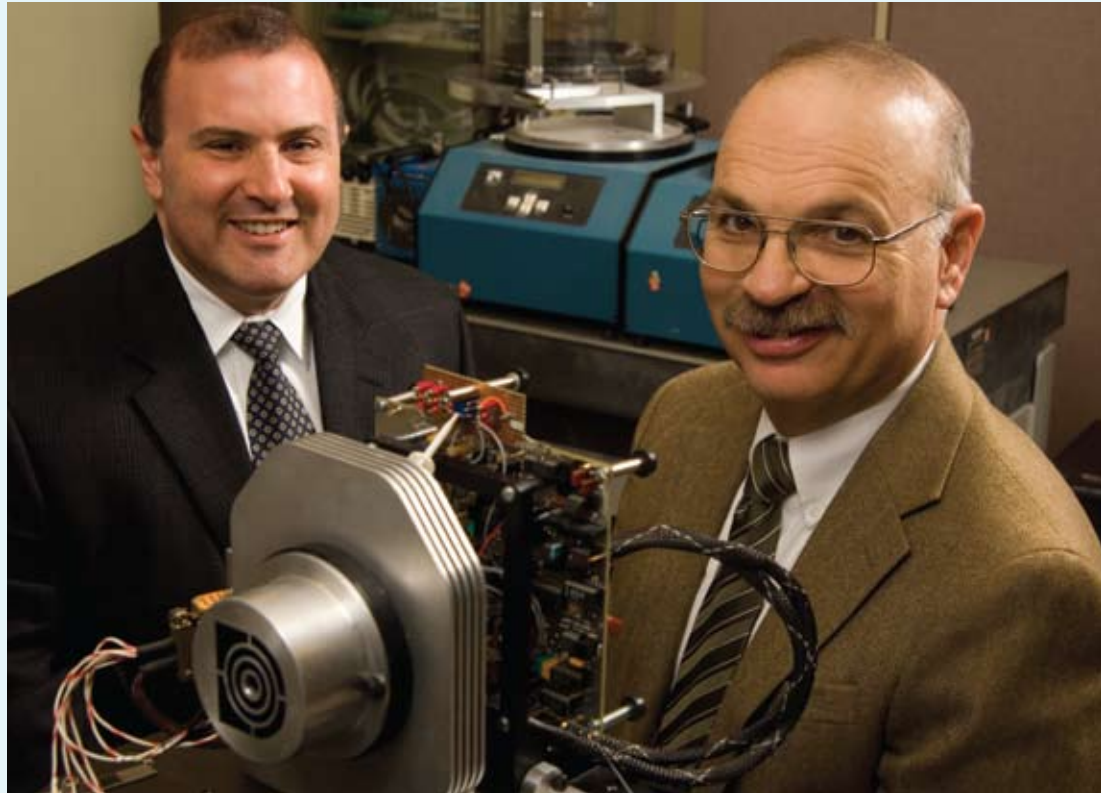
We gratefully acknowledge Draper Laboratory's financial support and the dedicated work of Draper's silicon fabrication and packaging groups. John Geen of Analog Devices offered fruitful insight into the ADXRS operation. Thanks to Beverly Tuzzalino for final preparation of the manuscript and to Neil Barbour for proofreading and discussions.

REFERENCES

- [1] Yazdi, N., F. Ayazi, and K. Najafi, "Micromachined Inertial Sensors," *Proc. IEEE*, Vol. 86, No. 8, 1998, pp. 1640-59.
- [2] Bernstein, J., "An Overview of MEMS Inertial Sensing Technology," *Sensors*, Vol. 20, No. 2, February 2003, pp. 14-21.
- [3] Ljung, P., *Micromachined Gyroscopes with Integrated Electronics*, Doctoral Thesis, EECS, University of California, Berkeley, CA, 1997.
- [4] Juneau, T., *Micromachined Vibratory Rate Gyroscopes*, Doctoral Thesis, EECS, University of California, Berkeley, CA, 1997.
- [5] Clark, W.A., *Micromachined Vibratory Rate Gyroscopes*, Doctoral Thesis, EECS, University of California, Berkeley, CA, 1997.
- [6] Yates, R., C. Williams, et al., "A Micromachined Rotating Gyroscope," IEE Colloquium on Silicon Fabricated Inertial Instruments, Savoy Place, London, UK, December 2, 1996.
- [7] Wood, D., G. Cooper, et al., "A Monolithic Silicon Gyroscope," IEE Colloquium on Silicon Fabricated Inertial Instruments, Savoy Place, London, UK, December 2, 1996.
- [8] Paoletti, F., M.A. Gretillat, N.F. de Rooij, "A Silicon Micromachined Vibrating Gyroscope with Piezoresistive Detection and Electromagnetic Excitation," *IEEE MEMS '96*, February 11-15, 1996.
- [9] Hashimoto, M., C. Cabuz, et al., *Silicon Resonant Angular Rate Sensor Using Electromagnetic Excitation and Capacitive Detection*, IOP Publishing Ltd., 1995.
- [10] Allen, J.J., R.D. Kinney, et al., "Integrated Micro-Electro-Mechanical Sensor Development for Inertial Applications," *Aerospace and Electronic Systems Magazine, IEEE*, Vol. 13, No. 11, November 1998, pp. 36-40.
- [11] Tang, T.K., R.C. Gutierrez, et al., "Silicon Bulk Micromachined Vibratory Gyroscope," Solid-State Sensor and Actuator Workshop, Hilton Head, SC, June 1996.
- [12] Logeeswaran, V.J., D.C.K. Ng, F.E.H. Tay, "A New Design Concept for Vibrating Microgyroscope," *SPIE Micromachining and Microfabrication*, Singapore, November 28-30, 2000.
- [13] Putty, M., *A Micromachined Vibrating Ring Gyroscope*, Doctoral Thesis, University of Michigan, Ann Arbor, MI, 1995.
- [14] Putty, M.W. and K. Najafi, "A Micromachined Vibrating Ring Gyroscope," Solid-State Sensor and Actuator Workshop, Hilton Head, SC, June 13-16, 1994.
- [15] Leger, P., "Quapason-A New Low-Cost Vibrating Gyroscope," Third St. Petersburg International Conference on Integrated Navigation Systems, St. Petersburg, Russia, 1994.
- [16] Leger, P., "Overview of the European MEMS Industry," Yole Development, Accessed January 24, 2004, <http://www.glen-nan.org/Documents/MEMS%20Europe.pdf>.
- [17] Madni, A.M. and R.D. Geddes, "A Micromachined Quartz Angular Rate Sensor for Automotive and Advanced Inertial Applications," *Sensors*, September 1999, pp. 26-33.
- [18] Madni, A.M., L.E. Costlow, S.J. Knowles, "Common Design Techniques for BEI Gyro Chip Quartz Rate Sensors for Both Automotive and Aerospace/Defense Markets," *IEEE Sensors J.*, Vol. 3, No. 5, 2003, pp. 569-78.
- [19] Lutz, M., W. Golderer, et al., "A Precision Yaw Rate Sensor in Silicon Micromachining," *Transducers '97*, Chicago, IL.
- [20] Lutz, M., W. Golderer, et al., "The Bosch Process," Accessed January 22, 2004, http://www.europractice.bosch.com/en/download/the_bosch_process.pdf.
- [21] Oskay, O., "Personal Communication," O-Navi Micro Avionics, January 23, 2003.
- [22] Park, K.Y., C.-W. Lee, et al., "Laterally Self-Oscillated and Force-Balanced Micro Vibratory Gyroscope Packaged in a Vacuum Package with a Conditioning ASIC," *SPIE*, Vol. 3242, 1997.
- [23] An, S., Y. Oh, et al., "Force-Balanced Microgyroscope," *SPIE*, Vol. 3242, 1997.
- [24] Andersson, G.I., N. Hedenstierna, et al., "A Novel Silicon Bulk Gyroscope," *Transducers '99*.
- [25] Adams, S., J. Groves, K. Shaw, "A Single-Crystal Silicon Gyroscope with Decoupled Drive and Sense," *SPIE Conference on Micromachined Devices and Components V*, Santa Clara, CA, September 1999.
- [26] Adams, S., J. Groves, K. Shaw, "SAR 10 Angular Rate Gyro," Accessed 1/26/2005, <http://www.sensor.com/>
- [27] Iyer, S.V., *Modeling and Simulation of Non-idealities in a Z-axis CMOS-MEMS Gyroscope*, PhD Thesis, Carnegie Mellon University, April 2003.
- [28] Iyer, S.V. and T. Mukherjee, "Simulation of Manufacturing Variations in a Z-Axis CMOS-MEMS Gyroscope," 5th International Conference on Modeling and Simulation of Microsystems (MSM), San Juan, Puerto Rico, April 22-25, 2002.
- [29] Acar, C. and A.M. Shkel, "Nonresonant Micromachined Gyroscopes with Structural Mode Decoupling," *IEEE Sensors Journal*, Vol. 3, No. 4, 2003, pp. 497-506.

- [30] Painter, C.C. and A.M. Shkel, "Structural and Thermal Modeling of a Z-Axis Rate Integrating Gyroscope," *Journal of Micromechanical Microengineering*, Vol. 13, 2003, p. 229-37.
- [31] Bernstein, J., S. Cho, et al., "A Micromachined Comb-Drive Tuning-Fork Rate Gyroscope," IEEE Microelectromechanical Systems, Fort Lauderdale, FL, February 7-10, 1993.
- [32] Bernstein, J. and M. Weinberg, *Comb Drive Tuning Fork Gyroscope*, U.S. Patent No. 5,349,855, September 27, 1994.
- [33] Tang, W.C., T.-C.H. Nguyen, et al., "Electrostatic Comb Drive of Laterally Driven Resonators," Transducers '89, Montreux, Switzerland, June 25-30, 1989.
- [34] Kwok, P.Y., M.S. Weinberg, K.S. Breuer, "Fluid Effects in Vibrating Micro-Machined Structures," *JMEMS*, Vol. 14, No. 4, August 2005.
- [35] Crandall, S.H. and N.C. Dahl, eds., *An Introduction to the Mechanics of Solids*, McGraw-Hill Book Co., New York, 1959.
- [36] Weinberg, M.S., K. Kumar, and A.T. King, *Dynamically Balanced Micromechanical Devices*, U.S. Patent No. 6,571,630 B1, June 3, 2003.
- [37] Ward, P., Electronics for Coriolis Force and Other Sensors, U.S. Patent No. 5,481,914, January 9, 1996.
- [38] Geen, J.A., S.J. Sherman, et al., "Single-Chip Surface Micromachined Integrated Gyroscope with 50 $\%$ Allan Deviation," *IEEE Journal of Solid State Circuits*, Vol. 37, No. 12, 2002, pp. 1860-6.
- [39] Geen, J.A. and D.W. Carow, *Micromachined Devices*, U.S. Patent No. 6,684,698 B2, February 3, 2004.
- [40] Geen, J.A. and D.W. Carow, *Micromachined Gyros*, U.S. Patent No. 6,122,961, September 26, 2000.
- [41] Geen, J. and D. Krakauer, "New iMEMS Angular-Rate-Sensing Gyroscope," *Analog Dialogue*, Vol. 37, No. 1, January 2003, pp. 12-5.
- [42] Geen, J.A. and D.W. Carow, *Micromachined Gyros*, U.S. Patent No. 6,505,511 B1, January 14, 2003.
- [43] Clark, W.A., T.N. Juneau, et al., *Dual-Mass Vibratory Rate Gyroscope with Suppressed Translational Acceleration Response and Quadrature-Error Correction Capability*, U.S. Patent No. 6,230,563 B1, May 15, 2001.

(l-r) Anthony Kourepenis
and Marc Weinberg



Marc Weinberg is a Laboratory Technical Staff Member. He has been responsible for the design and testing of a wide range of traditional micromechanical gyroscopes, accelerometers, hydrophones, microphones, angular displacement sensors, chemical sensors, and biomedical devices. He holds 25 patents with 12 additional in application. He served in the United States Air Force at the Aeronautical System Division, Wright-Patterson Air Force Base during 1974 and 1975, where he applied modern and classical control theory to design turbine engine controls, and at the Air Force Institute of Technology, where he taught gas dynamics and feedback control. He has been a member of the American Society of Mechanical Engineers (ASME) since 1971. Dr. Weinberg received BS (1971), MS (1971), and PhD (1974) degrees in Mechanical Engineering from MIT where he held a National Science Foundation Fellowship.

Anthony Kourepenis is currently Associate Director of the Tactical Programs Office at Draper Laboratory. He has been principally involved with the design of solid-state inertial instruments and has been the technical lead for several successful instrument and systems design, development, and demonstration programs. His diverse background includes experience in both hardware and software design, applied physics, data acquisition and analysis, sensor, instrument, and systems design, electronics architecture development, test and evaluation, error modeling and interpretation, and signal processing. He holds six patents and has four pending. Dr. Kourepenis received BSEE (1988) and MSEE (1992) degrees from Northeastern University and an MSEM (1996) from Tufts University.

Model-Based Variational Smoothing and Segmentation for Diffusion Tensor Imaging in the Brain

Mukund N. Desai,¹ David N. Kennedy,² Rami S. Mangoubi,¹ et al.

Copyright © 2006 Humana Press, Inc. Published in Neuroinformatics, Vol. 4, No. 3, 2006, pp. 217-234

abstract

This paper applies a unified approach to variational smoothing and segmentation to brain diffusion tensor image data along user-selected attributes derived from the tensor, with the aim of extracting detailed brain structure information. The application of this framework simultaneously segments and denoises to produce edges and smoothed regions within the white matter of the brain that are relatively homogeneous with respect to the diffusion tensor attributes of choice. The approach enables the visualization of a smoothed, scale-invariant representation of the tensor data field in a variety of diverse forms. In addition to known attributes such as fractional anisotropy, these representations include selected directional tensor components and, additionally associated continuous valued edge fields that may be used for further segmentation. A comparison is presented of the results of three different data model selections with respect to their ability to resolve white matter structure. The resulting images are integrated to provide a better perspective of the model properties (edges, smoothed image, etc.) and their relationship to the underlying brain anatomy. The improvement in brain image quality is illustrated both qualitatively and quantitatively, and the robust performance of the algorithm in the presence of added noise is shown. Smoothing occurs without loss of edge features due to the simultaneous segmentation aspect of the variational approach, and the output enables better delineation of tensors representative of local and long-range association, projection, and commissural fiber systems.

INTRODUCTION

Diffusion weighted and diffusion tensor magnetic resonance imaging (MRI) has come into widespread use over the past few years. This is mainly because of the unique view diffusion imaging provides of the microstructural details within the cerebral white matter in health and disease. As it represents a relatively new class of image data, the processing required for visualization and analysis of tensor data provides numerous new challenges.

¹ Control and Information Systems Division, Draper Laboratory, Cambridge, MA.

² Center for Morphometric Analysis and Massachusetts General Hospital (MGH)/MIT Athinoula A. Martinos Center for Biomedical Imaging, Department of Neurology, MGH, Boston.

The history and general descriptions of the standard methods for diffusion imaging are discussed in detail in recent reviews of the field.^{[11]-[3]} Diffusion imaging has been used in a host of clinical and research application areas.^{[4]-[13]} The ability to use diffusion tensor imaging (DTI) directionality and anisotropy to characterize the compact portion of discrete corticocortical association pathways in the cerebral white matter of living humans has been demonstrated and validated.^[14] Identification and visualization of specific fiber tracts^{[15]-[24]} and exploration of the potential to elicit information about functional specificity^[25] have also been carried out. The wide variety of application areas, along with the fact that the novel *in vivo* data are obtainable in this fashion makes DTI a potentially powerful clinical tool.

Compared with conventional MRI, however, DTI image acquisition is quite slow, due to the need to encode multiple different directions of diffusion sensitivity. This leads to practical tradeoffs in the use of DTI between acquisition time, diffusion sampling method, spatial resolution, and slice coverage. Partial volume effects are particularly problematic in DTI since competition of multiple different directional features within a voxel can render the resultant tensor not representative of the underlying anatomic structure. The development of methods that take optimal advantage of the diffusion data in light of potentially low signal-to-noise ratio (SNR) is an important objective for making DTI more clinically relevant.

Prior work in regularizing or smoothing diffusion tensor fields include the work in Reference [15], where a Markovian model is proposed to track brain fiber bundles in the DTI data. Diffusion direction is applied to fiber tract mapping and smoothing in Reference [26], in which the total variation norm algorithm is applied to the raw data. Regularization of diffusion-based direction maps to track brain white matter fascicles is reported in Reference [21], in which the emphasis is on the use of prior information in a Bayesian framework, and in Reference [27], in which the paths of anatomic connectivity are determined based on the directionality of the tensor. A continuous field approximation of discrete DTI data has been applied in Reference [28] to extract microstructural and architectural features of brain tissue. Smoothing employing parametric patches has been applied in Reference [23] to three-dimensional (3D) scattered data that describe anatomic structure.

In this paper, we present an algorithm for *simultaneous* smoothing or denoising and segmentation of diffusion tensor data. This algorithm smooths the image field within homogeneous regions, while at the same time preserves the edges of these regions at discontinuities by generating the associated edge fields based on user-selected tensor attributes. The smoothing and edge estimation are applied with respect to a user-selectable “mapping,” or models, of the input tensor data in order to emphasize specific properties of the tensor. Sample application of the algorithm is presented that demonstrates smoothing with respect to normalized tensor magnitude and principal eigenvector direction. In

these examples, the identification of white matter anatomic structure is qualitatively enhanced and reduction of regional anisotropy variance is quantified. This reduction in variance is then shown to be robust in the presence of added noise.

While demonstrated with respect to specific data models, this simultaneous smoothing and segmentation framework is general and opens a rich and versatile set of processing options to address the noisy, voxel-averaged sampling of DTI data. It also enables the selection of appropriate models of various physical characteristics of the diffusion tensor in cerebral white matter. Specific clinical objectives will dictate the optimal selection of “mapping” models and parameters for enhanced smoothing and segmentation and will be the focus of future studies.

MATERIALS AND METHODS

Data Acquisition

The sample data used in this paper used the following protocol: Siemens 1.5 Tesla Sonata, five sets of interleaved axial slices to provide $2 \times 2 \times 2$ mm³ contiguous coverage, single-shot echo-planar imaging (EPI) with six directional diffusion encoding directions, and a nonencoded baseline acquisition was performed with TR = 8 s, TE = 96 ms, averages = 12, number of slices = 12 per interleave, data matrix = 256 (read-out) \times 128 (phase encode), and diffusion sensitivity $b = 568$ s/mm². The total imaging time for the session was approximately 45 minutes. The subject provided informed consent and was a 35-year old, right-handed male normal control from a study of schizophrenia. The Institutional Review Board of the Massachusetts General Hospital approved the study protocol.

Computation of the Diffusion Tensor Attributes

Once the diffusion tensor, g , is sampled, the magnitude (or trace) can be calculated to express the *total* (no directionality) diffusivity at the voxel location. The directionality of the diffusion is assessed by an eigen decomposition of the diffusion tensor

$$g = \sum_{i=1}^3 \lambda_i s_i s_i^T$$

where λ_i , s_i , $i = 1, \dots, 3$ are the three eigenvalue-eigenvector pairs for the tensor with eigenvectors of unit magnitude. The largest eigenvalue and the associated eigenvector correspond to the major directionality of diffusion at that location. The fractional anisotropy fa ^[29] is a scalar measure that is often used to characterize the degree to which the major axis of diffusion is significantly larger than the other orthogonal directions.

$$fa = \sqrt{\frac{3}{2}} \sqrt{\frac{\sum_i \left(\lambda_i - \frac{1}{3} \sum_j \lambda_j \right)^2}{\sum_i \lambda_i^2}}$$

Specifically regarding brain imaging, to the extent that white matter fiber systems have homogeneous directionality at the spatial scale of the voxel size, these fiber systems

are expected to demonstrate significant anisotropy. More general eigenvalue/eigenvector-based scalar as well as vector and tensor features can be used to capture the underlying structure in the diffusion tensor image.

We have developed a segmentation and smoothing approach that permits user selection among these (and other) features of the tensor image in order to capture the relevant underlying structural details.

The Approach

The core concept of the method is the simultaneous variational segmentation and smoothing formulation. Given an observed tensor field, g , the objective is to obtain two outputs: the smoothed tensor u , and edge field v . These outputs, respectively, represent the simultaneous smoothing and segmentation of the raw tensor data. The approach, shown schematically in Figure 1, makes use of the following:

- A specified data fidelity model $H(u, g)$.
- A continuity model, $f(u)$, that forms a basis for adaptively determining the regions of continuity within which smoothing is to take place.

Energy Functional

In general, we may consider a region of interest Ω in a Euclidean space \mathbb{R}^n . Let x designate the pixel position in Ω . Thus, for 3D spatial data, we have $n = 3$. Our results are based on the processing of a slice from a brain image, so $n = 2$, and Ω is a two-dimensional (2D) region, and the vector x is a 2D position vector in, for instance, Cartesian coordinates. Over this region Ω , estimation of a field $u = u(x)$ is of interest, and measurements $g = g(x)$ are collected. The following energy functional^[30] for scalar fields is based on the energy functional of References [31] and [32]

$$E(u, v) = \int_{\Omega} \left(\alpha(1 - v)^2 \text{Tr} \left[u_x^T(x) u_x(x) \right] + \beta \text{Tr} \left((g - u)^T (g - u) \right) + \frac{\rho}{2} \text{Tr} (v_x^T v_x) + \frac{1}{2\rho} v^2 \right) dx \quad (1)$$

We generalize the above functional to vector field smoothing (introduction of tensor notation at this stage, although more cumbersome, provides no additional insight) with the introduction of the data fidelity and continuity functions ($h_1(u)$, $h_2(g)$), and $f(u)$, respectively

$$E(u, v) = \int_{\Omega} \left(\alpha(1 - v)^2 F(f_x(u)) + \beta H(h_1(u), h_2(g)) + \frac{\rho}{2} \text{Tr} (v_x^T v_x) + \frac{1}{2\rho} v^2 \right) dx \quad (2)$$

For a given data g and choices of functions $h_1(u)$, $h_2(g)$, and $f(u)$, the energy functional is minimized with respect to u and v . Input data g and smoothed data u are *vector* fields (tensor processing can be recast as vector processing) of dimensions m and r , respectively, whereas v is a *scalar* field that represents the edges of the smoothed vector field u . Further g , u and v are continuous n -dimensional fields and are *defined* for all x in *region* Ω in an n dimensional space x . The first term in the above functional represents a smoothing penalty term that favors spatial smoothness of vector field $f(u)$, rather than of u , at all interior points of the region, where edge field $v \ll 1$ with $0 \leq v \leq 1$, as explained later. It is worth noting that the field f may be of a lower dimension than the field u and that the smoothing penalty is in terms of a metric $F(f_x(u))$ of $f_x(u)$, the Jacobian with respect to x of the smoothed continuity function $f(u(x))$, which we simply denote by $f(u)$. Note that since the edge field v is also simultaneously estimated, the spatial extent of smoothing is adaptive with the smoothing penalty tending to zero over parts of region Ω , where edge strength v tends to 1.

The second term reflects data fidelity between the input data g , and smoothed field u , as given by the metric $H(h_1(u), h_2(g))$. We specify explicit forms for h_1 , h_2 , and f in the next section. The third and fourth terms represent prior models for the characteristics on the type of edge field dependent on just parameter ρ . The third term provides for smoothness of the edge field in terms of the 2-norm of its spatial gradient v_x , while the fourth term penalizes the excessive presence

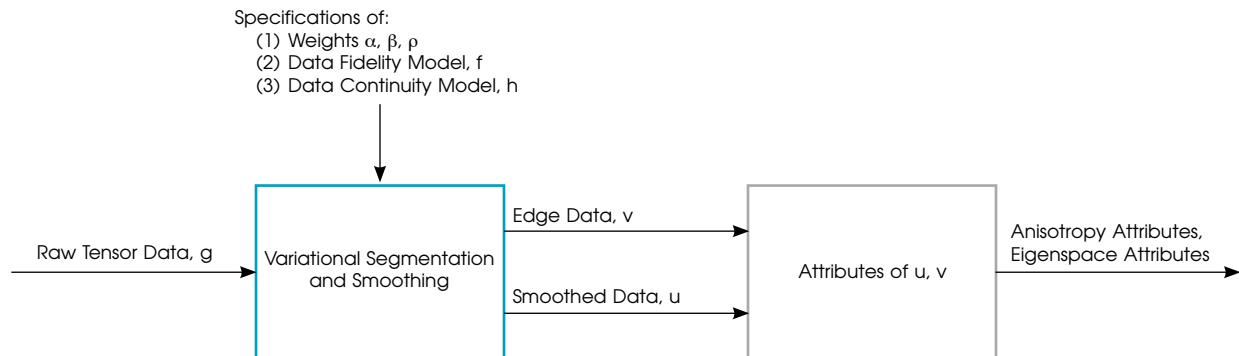


Figure 1. Block diagram of the variational segmentation processing framework. Variables are referred to in Eq. (1).

of edges. The constants α , β , and ρ represent the chosen weights on the accompanying cost components and determine the nominal smoothing radius, the edge width, as well as govern the value of edge function v . Specifically, the ratio α/β is related to the nominal smoothing radius, ρ to the edge width, and α governs the edge strength. Further details governing the choice of constants α , β , and ρ is discussed in Reference [33]. For more details on the segmentation approach and on the results of the application of the functional for smoothing and segmentation of phantom, MRI and functional magnetic resonance imaging (fMRI) scalar data, as well as for the fusion of different modality data, see References [33]-[36] and the references therein.

The edges are estimated based on continuity attributes $f(u)$ of the smoothed tensor field u and the specified prior model on edge field. The Euler Lagrange equations that are the necessary conditions associated with the minimization of the energy functional can be solved by the gradient descent method (e.g., References [33]-[35]).

From the outputs u and v , additional relevant attributes associated with size, shape, and orientation of the diffusion ellipsoid may be distilled for further analysis. Example attributes include the trace (for diffusion magnitude), anisotropy measures (for diffusion “shape”), and the direction of eigenvectors (for diffusion orientation).^[37] The ability to select functions $f(u)$ and $h_1(u)$, $h_2(g)$ to satisfy various continuity and data fidelity requirements, respectively, is an important advantage that enables the viewing of the same DTI data from different perspectives.

Application to DTI Data

Depending on the objective, one can select the continuity functions $h_1(u)$, $h_2(g)$ and fidelity function $f(u)$ to obtain an edge field v and an accompanying smoothed tensor field u with respect to specific features of the data. Differential smoothing concerns can thus be applied to different weighted eigenspace components of the tensor, and more generally, to any other sets of attributes of the tensor.

We next illustrate two different models that capture different characteristics of spatial similarity for the tensor data by selection of different forms of continuity function $f(u)$ and the data fidelity function $h_2(g)$ while retaining the same form of function $h_1(u) = u$

- (a) Normalized tensor smoothing

$$f = \frac{u}{\|u\|_2}, h_2(g) = g$$

- (b) Dominant directional tensor component smoothing

$$f = \frac{u}{\|u\|_2}, h_2(g) = \lambda_1 s_1 s_1^T$$

where λ_1 is the maximum of the three eigenvalues of the tensor g .

The first model represents a scale-invariant continuity criterion for the tensor data g . By contrast, the second model

assumes the same invariance continuity criterion as the first, but with respect to only the subspace of tensor g associated with its dominant eigenvector s_1 . The objective of identifying regions of spatial continuity within the image, or equivalently, segmenting, motivates the choice of model. It may be noted that for dominant directional tensor smoothing in (b) above, we have chosen to work in the rank-1 dominant tensor space $s_1 s_1^T$ rather than the vector space of associated direction s_1 .

For measures, we adopt the following choices for F , H of Eq. (2)

$$F(f_x(u)) = \|f_x(u)\|_2^2 = \text{Tr} [f_x(u)^T f_x(u)] \quad (3)$$

$$H(h_1(u), h_2(g)) = \|u - h_2(g)\|_2^2 = \text{Tr} [(u - h_2(g))^T (u - h_2(g))] \quad (4)$$

where F and H represent the Euclidean norm of the gradient of $f(u)$ and the estimated error $u - h_2(g)$, respectively.

Assessment

In order to assess the results of the application of this processing to clinically relevant DTI data, we selected a representative axial slice that included a comprehensive set of neuroanatomic white matter regions of interest (ROIs). These anatomic regions include the corpus callosum, internal capsule, superior longitudinal fasciculus, and cingulum bundle. First, we visually inspect the results of the smoothing modes on the appearance of fractional anisotropy (fa) maps as well as in visualization of tensor orientation information. Second, we quantify these observations by evaluating the distribution of fa values over the anatomic regions listed above. Third, we evaluate the sensitivity of the proposed methodology by comparing, using images and the change in performance with traditional methods when noise is added to the raw data. We choose to add Gaussian noise at increasing levels to the data, with negative values set to zero to remain within the physical constraint of non-negative intensity. In addition to comparing the proposed method and the traditional approach using images, we also quantify the effect of noise on the performance of the proposed approach in terms of the coefficient of variation of the fa over each anatomic region of interest.

Results

In this section, we demonstrate the operation of the algorithm in the context of two different smoothing models, characterize this processing in the context of anatomic information contained within the DTI data, and summarize some of the noise properties of the implementation. Figure 2 demonstrates a number of different views of the results of this smoothing procedure on an axial brain slice. This includes the raw (unsmoothed) data in the first column as well as the results of the two different smoothing models: normalized tensor in the second column, and directional projection in the third column. The “cuboid” and color representations^[38] of the directional information contained

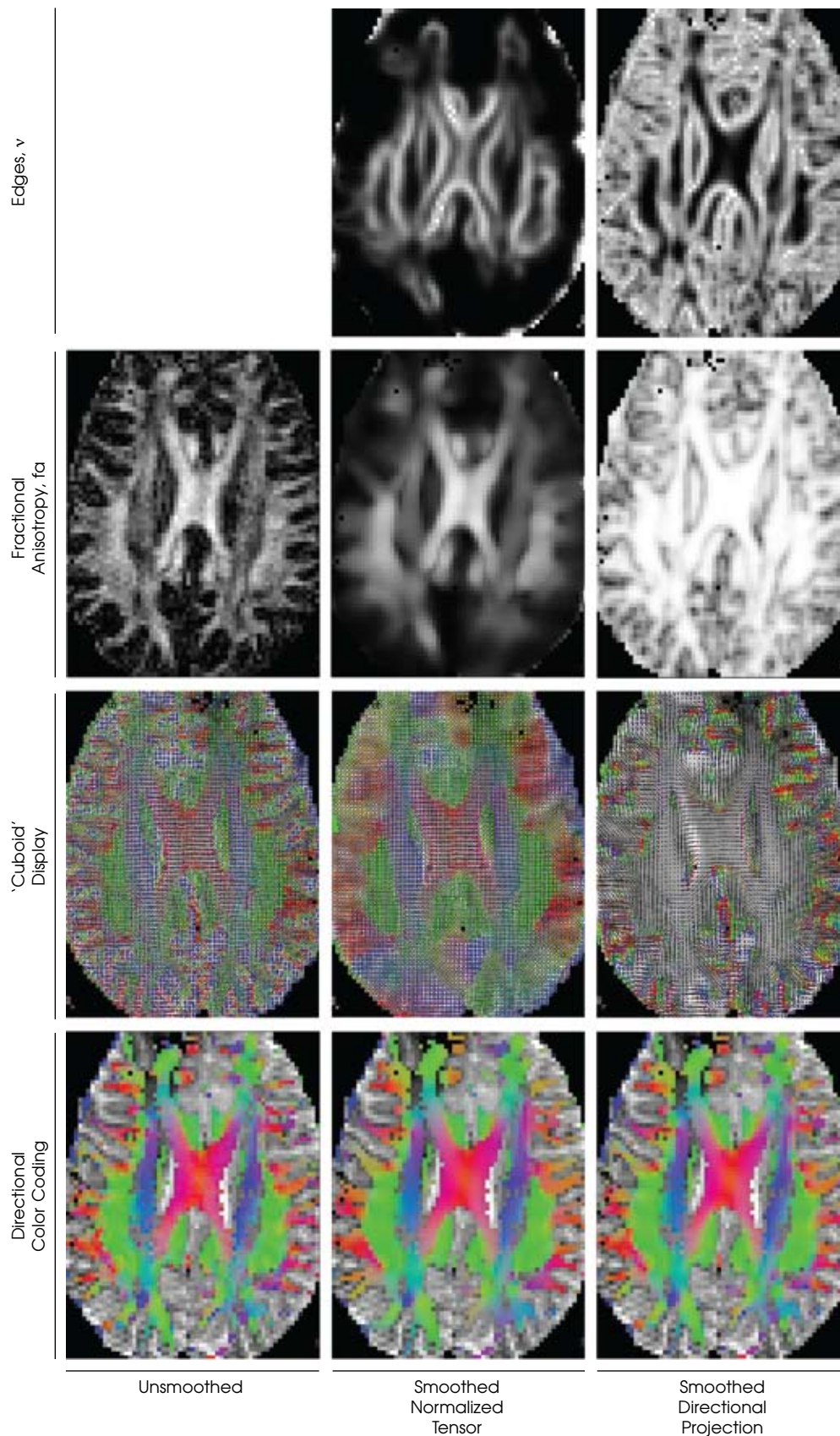


Figure 2. Effect of two smoothing models (2nd and 3rd columns) on an axial brain slice. The fractional anisotropy and edge maps are displayed in the first two rows, and the “cuboid” and color representations of the directional information contained in the resultant tensor fields are displayed in the last two rows. Maximum details emerge when smoothing is most selective, directional projection based (3rd column), within the edge field boundaries.

in the resultant tensor fields are presented in the third and fourth rows, respectively.

From the edge field visualization in the first row, it is clear that the most details consistent with the anatomic structure emerge when smoothing is most selective within the edge field boundaries. Specifically, the edge map in the third column, which is based on the directional projection, displays more details than the edge map in the second column, which is based on the normalized tensor.

The second row of images indicates that the impact of edge preservation on the smoothing of the tensor field and its components can also be appreciated from the fa images for the smoothed tensor. The raw data's fractional anisotropy is shown in the first column for comparison.

It might be remarked that by definition, the fractional anisotropy of the directional component in the raw data will be unity and of interest is the deviation from unity that arises from the spatial variation of the dominant direction component that is reflected in the smoothing. The quantitative impact of different modes of smoothing is presented

in Table 1. This includes the mean and standard deviation of the functional anisotropy fa (as well as the coefficient of variation (CV)) for five anatomically motivated and manually defined regions annotated in Figure 3. These regions were identified by a trained neuroanatomist using both tensor orientation and anisotropy information. For the case of normalized tensor smoothing, SNR, or equivalently the reciprocal of the CV, is improved for all regions except for lateral ventricle whose edges with the adjacent region of the internal capsule are not well delineated, resulting in loss of restricted regional smoothing at the border of that region. For the case of directional smoothing, SNR values are uniformly enhanced for all regions due to better regional edge details and attendant region limited smoothing. The CV is reduced by at least 2.5-fold when comparing directional smoothing to the original measures of anisotropy, indicating a concomitant increase in the resultant SNR for these measures.

The “cuboid” displays in the third row of Figure 2 can explain the superior performance of the directional projection method in the third column. These cuboid displays are better appreciated by looking at a closeup of particular regions, as is done in

Table 1.

	Raw Tensor fa	Smoothed Normalized Tensor fa	Smoothed Dominant Directional Tensor Component fa
Corpus Callosum			
Mean (μ)	0.646	0.5806	0.9575
Std. Dev (σ)	0.117	0.1014	0.0493
CV (100 σ/μ)	18.1	17.46	5.14
Cingulum Bundle			
Mean (μ)	0.5524	0.4306	0.9238
Std. Dev (σ)	0.151	0.0953	0.0515
CV (100 σ/μ)	27.3	22.13	5.57
Internal Capsule			
Mean (μ)	0.3615	0.28	0.9308
Std. Dev (σ)	0.0768	0.0493	0.0620
CV (100 σ/μ)	21.24	17.61	6.67
Superior Longitudinal Fasciculus			
Mean (μ)	0.5676	0.4928	0.9496
Std. Dev (σ)	0.1078	0.0799	0.0598
CV (100 σ/μ)	18.99	16.21	6.30
Lateral Ventricle			
Mean (μ)	0.2647	0.2078	0.8103
Std. Dev (σ)	0.1136	0.1233	0.0883
CV (100 σ/μ)	42.92	59.34	10.90

This table demonstrates the quantitative impact of different modes of smoothing and segmentation in terms of mean, standard deviation and coefficient of variation (CV) statistics of fractional anisotropy fa in five different regions of the brain for the particular 2-D slice of DTI data shown in Figure 4. The CVs are lowest, an indication that directional smoothing yields effective segmentation of homogeneous regions.

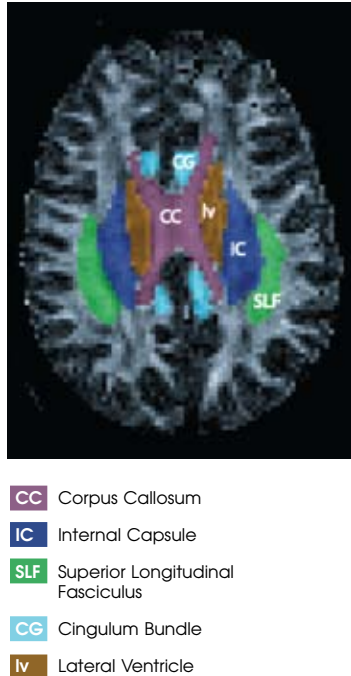


Figure 3. Manual delineation of five anatomically motivated regions for further analysis (Figure 6, Table 1) of impact of different modes of smoothing and segmentation on fractional anisotropy of smoothed tensor in the regions. Delineations were based on tensor orientation and anisotropy and are shown with respect to the fractional anisotropy map here.

the second row of Figure 4. The closeup region, a portion of the cerebral hemisphere, is indicated in the top image of the first row. We added images displaying the dominant direction vectors for the raw data, the smoothed normalized tensor, and the smoothed directional projection in the third row of Figure 4 for the sake of comparison. Again, we see that direction details are better kept using the smoothed directional projection. One example is the region above the thick arrows, where directional (curved corners) structure is preserved in the directional image, but smoothed over in the normalized tensor image. *Comparison of other parts of the closeup views leads to a similar conclusion. It is this preservation of the higher dimensional directional characteristics of the tensor at the pixel level that is responsible for the superior image obtained from the directional projection method.*

We now consider added noise, our third assessment criterion. The effect of added noise is evaluated to establish the robustness of the approach. In Figures 5 and 6, we compare the results of increasing noise levels added to the raw data. Levels of the additional noise range from 0 (no simulated noise added) to approximately 5 times the estimated sigma value. The sigma

value was estimated from the raw data outside the brain. These images include: top row – raw data fractional anisotropy (fa); second row – smoothed fractional anisotropy; third row – our edge field v ; bottom row - conventional Sobel edge field of raw fa. Using anatomically-based ROIs, Figure 6 illustrates, for the corpus callosum region, that the smoothed tensor-based estimate of regional anisotropy fa in the second row of Figure 5 has a substantially lower coefficient of variation (bottom curve in Figure 6) than the original data (top curve in Figure 6); the reduction is by almost a factor of 10. Similar reductions were obtained for all other regions of Figure 4: cingulum bundle, superior longitudinal fasciculus, and internal capsule. Additionally, as Figure 5 indicates, comparison of edge fields from our approach on the third row with a conventional Sobel edge field on the fourth row illustrates that, while added noise has a deleterious effect on the Sobel edge field, the new models introduced to the energy functional preserve details even as noise is added.

DISCUSSION

The above results demonstrate the model-based variational segmentation functional approach's ability to provide a diverse collection of output images within a unified framework. The usefulness of the variational segmentation functional approach has been demonstrated for other forms of brain imaging, such as structural^[34] and functional magnetic resonance imaging data.^[35]

The versatility of these functionals, in their ability to produce a diverse collection of output images, is an important addition to the methods or tools available for image analysis. This innovation provides a unified framework for spatially selective smoothing of noisy brain image data along attributes of choice derived from the diffusion tensor whereby we can adaptively determine smoothed regions within the white matter that are relatively homogeneous with respect to specific tensor properties of shape, size, and orientation of the associated diffusion ellipsoid. In addition to providing a demarcation of the regions with respect to user-specified attributes of homogeneity in the DTI data, the segmentation functional is amenable and flexible to using prior information on attributes of both the tensor and edge field with incorporation of additional penalty terms in the functional. Determining smoothed regions with specific tensor properties enhances the ability to characterize the morphometric properties of the compact portion, or "stem," of the major white matter pathways in regions where partial volume problems and the validity of the tensor assumption are less problematic.^[14]

A comparison has been presented of attributes such as anisotropy and direction of diffusion for the raw tensor itself without smoothing, the smoothed normalized tensor,

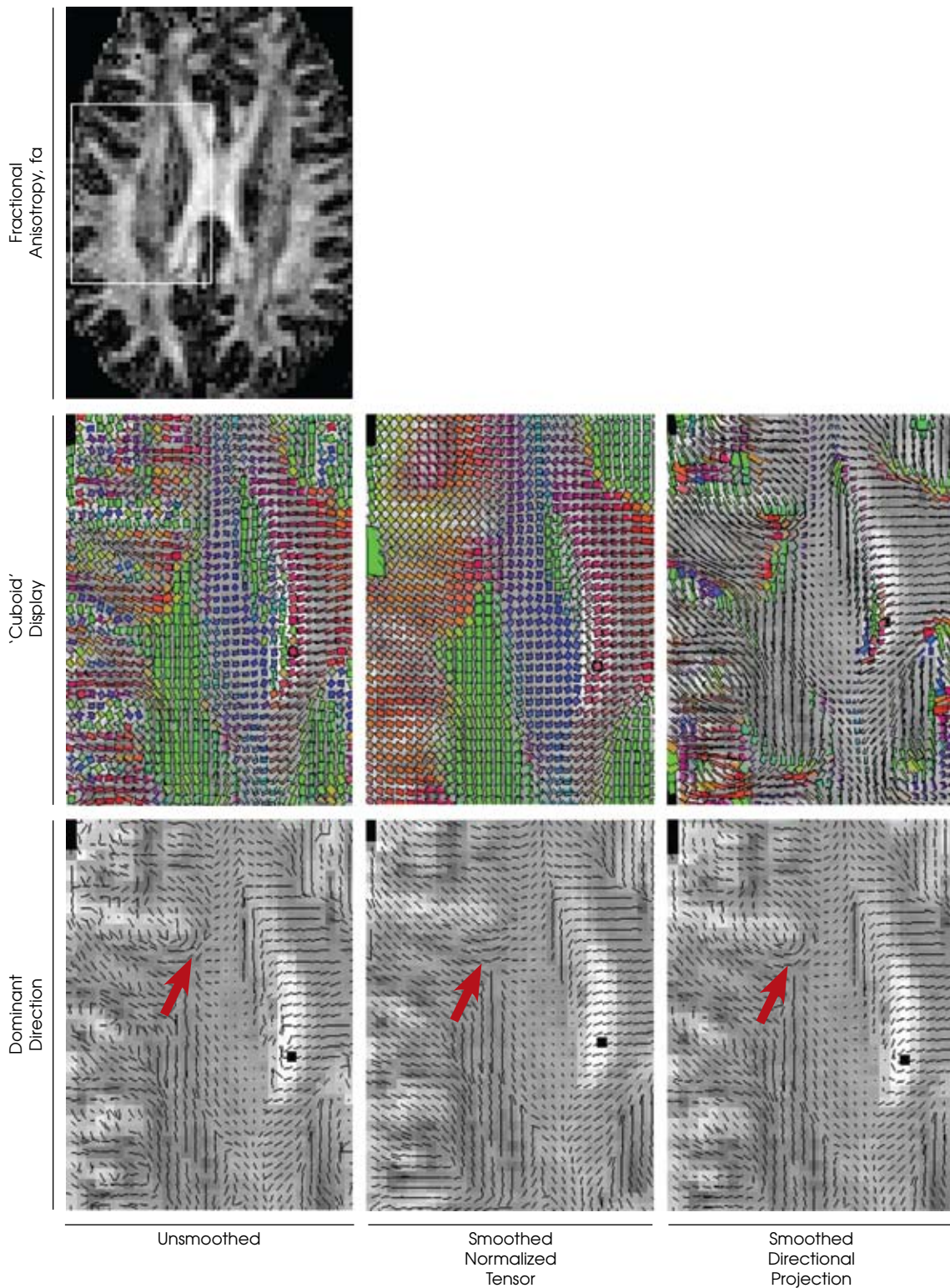


Figure 4. Closeup displays demonstrate the effect of normalized tensor (2nd column) and directional projection (3rd column) smoothing more clearly by displaying the 'cuboid' (2nd row) and dominant direction vector (3rd row) of the principal eigenvector for these two models for a portion of the cerebral hemisphere marked on fractional anisotropy display. Region above thick arrows are one example where directional projection preserves details more visibly.

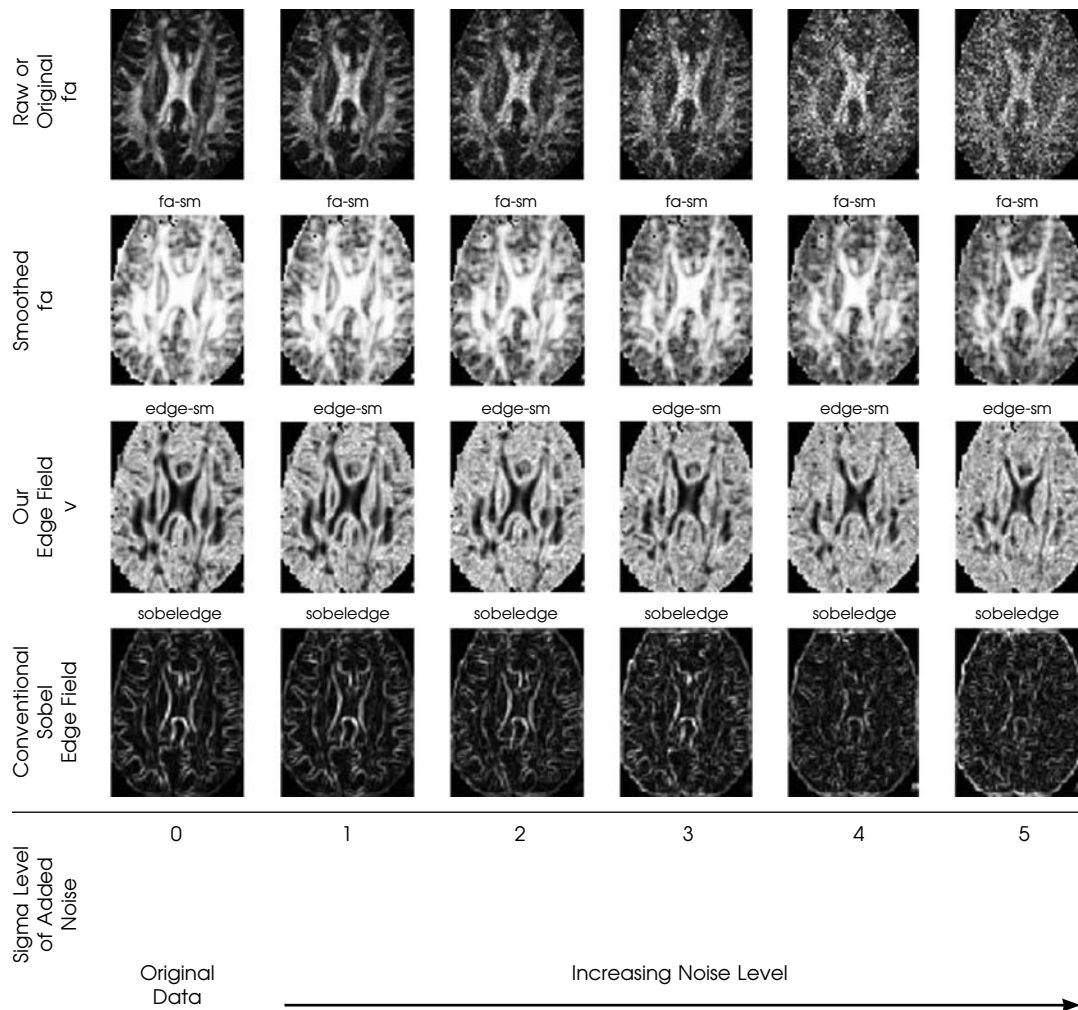


Figure 5. Effect of added noise on raw fa, smoothed fa, our edge field v , and conventional Sobel edge field. The directional projection-based smoothing and segmentation (2nd and 3rd row) are more robust to added noise.

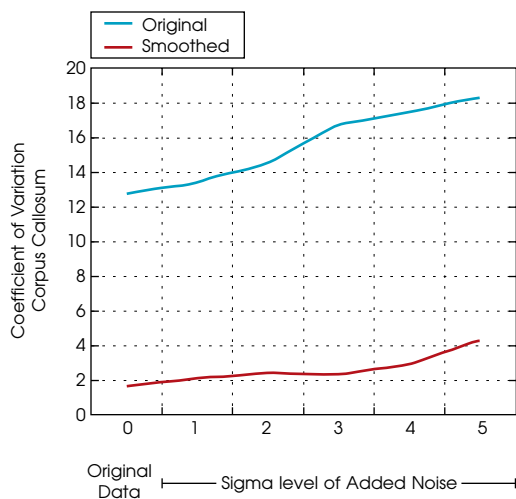


Figure 6. Effect of noise on smoothing. The coefficient of variation of the smoothed fa (bottom curve) corresponding to the second row of images in Figure 5 is significantly lower than that of the raw or original fa (top curve) corresponding to the first row of Figure 5. Curves are for corpus callosum region. Similar results obtain for other regions in Figure 3.

and the smoothed tensor component associated with the dominant eigenvector. The underlying diffusion characteristics of the white matter in the brain motivate the choice of these mappings, whereas normalization provides scale invariance of salient features. Therefore, it is possible to visualize attributes of anisotropy and direction of the resultant tensor fields and the associated edge field in various ways. In this fashion, the applicability of a unified and versatile image processing framework for smoothing and feature extraction in support of fiber pathway identification within the human brain is demonstrated.

Specifically, promise of the utility of the variational simultaneous smoothing and segmentation functional to improve the characteristics of tensor-valued imaging data has been demonstrated. The result is an improvement of the overall signal that preserves the anatomic detail. Within the directional component smoothing case, regions of discrete directionality are smoothed, but transitions between regions are well preserved. This can be particularly well seen as one traverses from the cortex toward the central portion of the images shown in Figure 4. The white matter contained within the gyral folds near the cortex remains nicely visualized and oriented “out” of the gyri. Transitions of radially oriented white matter of the corona radiata and U fibers with the perpendicularly oriented internal capsule and various associational pathways are clearly demarked. This level of detail is only retained in the directional smoothing case. Finally, it should be noted that visualization based on the dominant direction coding in Figure 2 is less sensitive to the underlying variations and noise structure, presumably due to the subtleties of the variations in intensity of directional noise compared to the large color differences of the different fiber systems. For the images examined, directional smoothing thus seems appropriate because of the simple fact that it simultaneously smooths while preserving directionality. This smoothing can act as a preprocessing step for virtually any subsequent processing of the diffusion data, such as between group analyses of anisotropy data,^{[11],[39]} anatomic regional characterization,^[40] and tractographic reconstruction.^{[41]-[43]}

Turning to the results of Figures 5 and 6, we examine respectively two aspects: the edges and the coefficient of variation over ROIs. First, as the graph demonstrates, the coefficient of variation of μ calculated over the anatomic region of the corpus callosum is dramatically reduced (improved) with simultaneous smoothing and segmentation, and that this substantial improvement holds even in the presence of the greatly reduced image quality at the maximum added noise.

Turning to the edges in Figure 5, we observe that with incrementally increasing noise added to the raw data, the conventional (Sobel) edge field is seen to deteriorate more rapidly. By contrast, with our approach, edges are

maintained at the increased noise levels. This result is a direct consequence of working with a most dominant feature of the tensor, specifically, the dominant rank-1 tensor.

Limitations

A method that is generalizable in terms of processing image data and its dimensionality is presented. The application used to illustrate the processing, namely DTI, is an important and new radiological tool for the clinical assessment of cerebral white matter. Processing can improve the resultant SNR without penalizing the resultant spatial resolution, and thus can enhance the utility of these measurements. This improvement in SNR can be used to shorten the potentially lengthy diffusion acquisition time. It is acknowledged that the tensor acquisition may not be optimal for observation of specific fiber tracts themselves, and that this acquisition optimization is an open research question. These processing tools, however, will extend to a higher order (i.e., q-space and high angular resolution) diffusion acquisitions,^{[44]-[46]} and can still play an important role in the processing and analysis of these classes of data acquisition. Indeed, the utility of submodel-based smoothing becomes even more important as the complexity of the input data increases. The flexibility of the methods we report here can be adapted easily for processing models defined in terms of any matrix decomposition of the acquired data, not just the eigen-decomposition typical in the six-direction tensor acquisitions. Also, there is a spatial resolution tradeoff between the need for high resolution to observe subtle white matter pathways and the acquisition time available for the subjects. These processing tools will be helpful to extend the limits of SNR in the extraction of meaningful anatomic information. An additional area of potential impact for a tool such as this includes utilizing tensor information in solving for neural systems-based functional imaging.^{[47]-[49]} It might be remarked that the focus of the reported work is the model-based optimal extraction of information for a given SNR and DTI data acquisition parameters, and future work remains necessary for optimization involving SNR and data acquisition parameters.

We note that the simultaneous smoothing and segmentation process can change the nature of the error in the smoothed estimates and the use of smoothed estimates for further analysis, such as for group analysis, which may need to employ alternate analysis approaches that are not necessarily based on a specific noise model assumption such as Gaussian noise. For example, for decision support, methods such as support vector machines can be employed.

In addition, the method's appeal is the flexibility to use various lower dimensional attributes of the higher dimensional data using functions F and H , and we demonstrate this strength here primarily in the context of 2D data. The method, however, can be readily applied to 3D data. In the

case of 3D analysis, additional terms associated with gradients of the data and edge fields in the added third dimension arise in the energy functional E of (2). We, therefore, have edge surfaces in 3D that are smoother than those obtainable from edge boundaries produced by the 2D analysis.

To conclude, we have presented a general framework for smoothing diffusion tensor data and have developed a tool to execute this processing. The preferred choice of the fidelity and continuity functions $h_1(u)$, $h_2(g)$ and $f(u)$ generally will depend on both the image and the objective of the image analysis task. There is no universal image model that outperforms all others in all situations. Moreover, different regions of the data domain require segmentations based on more than one model. An important objective in this study is, therefore, to identify for DTI data a small number of potent models that can be adapted for effective segmentation. Further, as no single model applies over the entire image due to variations in the underlying tissue and partial volume effects, *adaptive learning of relevant features at every voxel based on neighborhood characteristics* is another focus of ongoing research. The improved output data will enable a more refined analysis, including segmentation of white matter substructures using various manual and automated techniques.

Acknowledgment

This work supported by PHS Research Grant no. 2 R01 NS34189 from the National Institute of Neurological Disorders and Stroke (NINDS), National Cancer Institute (NCI) and National Institute of Mental Health (NIMH), as part of the Human Brain Project, and a Draper Laboratory R&D project. We also acknowledge Van Wedeen and David Tuch for helpful discussions and visualization tools.

REFERENCES

- [1] Mori, S. and P.B. Barker, "Diffusion Magnetic Resonance Imaging: Its Principle and Applications," *Anat. Rec.*, Vol. 257, No. 3, 1999, pp. 102-109.
- [2] Le Bihan, D., J.F. Mangin, C. Poupon, C.A. Clark, S. Pappata, N. Molko, H. Chabriat, "Diffusion Tensor Imaging: Concepts and Applications," *J. Magn. Reson. Imaging*, Vol. 13, No. 4, 2001, pp. 534-546.
- [3] Parker, G.J. "Analysis of MR Diffusion Weighted Images," *Br. J. Radiol.* 77 Spec. No 2: S176-85, 2004.
- [4] Pierpaoli, C., A. Righini, I. Linfante, J.H. Tao-Cheng, J.R. Alger, G. Di Chiro, "Histopathologic Correlates of Abnormal Water Diffusion in Cerebral Ischemia: Diffusion-Weighted MR Imaging and Light and Electron Microscopic Study," *Radiology*, Vol. 189, No. 2, 1993, pp. 439-448.
- [5] Hossmann, K.A., M. Fischer, K. Bockhorst, M. Hoehn-Berlage, "NMR Imaging of the Apparent Diffusion Coefficient (ADC) for the Evaluation of Metabolic Suppression and Recovery after Prolonged Cerebral Ischemia," *J. Cereb. Blood Flow Metab.*, Vol. 14, No. 5, 1994, pp. 723-731.
- [6] Sorensen, A.G., F.S. Buonano, R.G. Gonzalez, L.H. Schwamm, M.H. Lev, F.R. Huang-Hellinger, T.G. Reese, R.M. Weisskoff, T.L. Davis, N. Suwanwela, U. Can, J.A. Moreira, W.A. Copen, R.B. Look, S.P. Finkelstein, B.R. Rosen, W.J. Koroshetz, "Hyperacute Stroke: Evaluation with Combined Multisection Diffusion-Weighted and Hemodynamically Weighted Echo-Planar MR Imaging," *Radiology*, Vol. 199, No. 2, 1996, pp. 391-401.
- [7] Sorensen, A.G., O. Wu, W.A. Copen, T.L. Davis, R.G. Gonzalez, W.J. Koroshetz, T.G. Reese, B.R. Rosen, V.J. Wedeen, R.M. Weisskoff, "Human Acute Cerebral Ischemia: Detection of Changes in Water Diffusion Anisotropy by Using MR Imaging," *Radiology*, Vol. 212, No. 3, 1999, pp. 785-792.
- [8] Lim, K.O., M. Hedehus, M. Moseley, A. de Crespigny, E.V. Sullivan, A. Pfefferbaum, "Compromised White Matter Tract Integrity in Schizophrenia Inferred from Diffusion Tensor Imaging," *Arch. Gen. Psychiatry*, Vol. 56, No. 4, 1999, pp. 367-374.
- [9] Klingberg, T., M. Hedehus, E. Temple, T. Salz, J.D. Gabrieli, M.E. Moseley, R.A. Poldrack, "Microstructure of Temporo-Parietal White Matter as a Basis for Reading Ability: Evidence from Diffusion Tensor Magnetic Resonance Imaging," *Neuron*, Vol. 25, No. 2, 2000, pp. 493-500.
- [10] Meyer, J.R., A. Gutierrez, B. Mock, D. Hebron, J.M. Prager, M.T. Gorey, D. Homer, "High-b-Value Diffusion-Weighted MR Imaging of Suspected Brain Infarction," *AJNR Am. J. Neuroradiol.*, Vol. 21, No. 10, 2000, pp. 1821-1829.
- [11] Pfefferbaum, A., E.V. Sullivan, M. Hedehus, K.O. Lim, E. Adalsteinsson, M. Moseley, "Age-Related Decline in Brain White Matter Anisotropy Measured with Spatially Corrected Echo-Planar Diffusion Tensor Imaging," *Magn. Reson. Med.*, Vol. 44, No. 2, 2000, pp. 259-268.
- [12] Wiegell, M.R., H.B. Larsson, V.J. Wedeen, "Fiber Crossing in Human Brain Depicted with Diffusion Tensor MR Imaging," *Radiology*, Vol. 21, No. 3, 2000, pp. 897-903.
- [13] Beaulieu, C., "The Basis of Anisotropic Water Diffusion in the Nervous System, a Technical Review," *NMR Biomed.*, Vol. 15, 2002, pp. 435-455.
- [14] Makris, N., A.J. Worth, A.G. Sorensen, G.M. Papadimitriou, O. Wu, T.G. Reese, V.J. Wedeen, T.L. Davis, J.W. Stakes, V.S. Caviness, E. Kaplan, B.R. Rosen, D.N. Pandya, D.N. Kennedy, "Morphometry of In Vivo Human White Matter Association Pathways with Diffusion-Weighted Magnetic Resonance Imaging," *Ann. Neurol.*, Vol. 42, No. 6, 1997, pp. 951-962.
- [15] Poupon, C., J.F. Mangin, V. Frouin, J. Regis, F. Poupon, M. Pachot-Clouard, D. LeBihan, I. Bloch, "Regularization of MR Diffusion Tensor Maps for Tracking Brain White Matter Bundles," *Proceedings of MICCAI'98*, 1998, pp. 489-498.
- [16] Conturo, T.E., N.F. Lori, T.S. Cull, E. Akbudak, A.Z. Snyder, J.S. Shimony, R.C. McKinstry, H. Burton, M.E. Raichle, "Tracking Neuronal Fiber Pathways in the Living Human Brain," *Proc. Natl. Acad. Sci. USA*, Vol. 96, No. 18, 1999, pp. 10422-10427.
- [17] Mori, S., B.J. Crain, V.P. Chacko, P.C. van Zijl, "Three-Dimensional Tracking of Axonal Projections in the Brain by Magnetic Resonance Imaging," *Ann. Neurol.*, Vol. 45, No. 2, 1999, pp. 265-269.
- [18] Basser, P.J., S. Pajevic, C. Pierpaoli, J. Duda, A. Aldroubi, "In Vivo Fiber Tractography Using DT-MRI Data," *Magn. Reson. Med.*, Vol. 44, No. 4, 2000, pp. 625-632.
- [19] Zhang, S., C. Curry, D.S. Morris, D.H. Laidlaw, "Visualizing Diffusion Tensor MR Images Using Streamtubes and Stream-surfaces," *Proceedings of the IEEE Visualization Conference*, Utah, 2000.

- [20] Pierpaoli, C., A. Barnett, S. Pajevic, R. Chen, L.R. Penix, A. Virta, P. Basser, "Water Diffusion Changes in Wallerian Degeneration and Their Dependence on White Matter Architecture," *Neuroimage*, Vol. 13, No. 6, Pt. 1, 2001, pp. 1174-1185.
- [21] Poupon, C., J. Mangin, C.A. Clark, V. Frouin, J. Regis, D. Le Bihan, I. Bloch, "Towards Inference of Human Brain Connectivity from MR Diffusion Tensor Data," *Med. Image Anal.*, Vol. 5, No. 1, 2001, pp. 1-15.
- [22] Stieltjes, B., W.E. Kaufmann, P.C. van Zijl, K. Fredericksen, G.D. Pearlson, M. Solaiyappan, S. Mori, "Diffusion Tensor Imaging and Axonal Tracking in the Human Brainstem," *Neuroimage*, Vol. 14, No. 3, 2001, pp. 723-735.
- [23] Grimm, C.M., J.J. Crisco, D.H. Laidlaw, "Fitting Manifold Surfaces to Three-Dimensional Point Clouds," *J. Biomech. Eng.*, Vol. 124, No. 1, 2002, pp. 136-140.
- [24] Mori, S., W.E. Kaufmann, C. Davatzikos, B. Stieltjes, L. Amodei, K. Fredericksen, G.D. Pearlson, E.R. Melhem, M. Solaiyappan, G.V. Raymond, H.W. Moser, P.C. van Zijl, "Imaging Cortical Association Tracts in the Human Brain Using Diffusion-Tensor-Based Axonal Tracking," *Magn. Reson. Med.*, Vol. 47, No. 2, 2002, pp. 215-223.
- [25] Darquie, A., J.B. Poline, C. Poupon, H. Saint-Jalmes, D. Le Bihan, "Transient Decrease in Water Diffusion Observed in Human Occipital Cortex During Visual Stimulation," *Proc. Natl. Acad. Sci. USA*, Vol. 98, No. 16, 2001, pp. 9391-9395.
- [26] Vermuri, B.C., Y. Chen, M. Rao, T. McGraw, Z. Wang, T. Mareci, "Fiber Tract Mapping from Diffusion Tensor MRI," *Proceedings of the IEEE Workshop on Variational Level Set Methods in Computer Vision*, 2001, pp. 81-88.
- [27] Parker, G.J.M., C.A.M. Wheeler-Kingshott, G.J. Barker, "Estimating Distributed Anatomical Connectivity Using Fast Marching Methods and Diffusion Tensor Imaging," *IEEE Trans. On Med. Imaging*, Vol. 21, No. 5, 2002, pp. 505-512.
- [28] Pajevic, S., A. Aldroubi, P.J. Basser, "A Continuous Tensor Field Approximation of Discrete DT-MRI Data for Extracting Microstructural and Architectural Features of Tissue," *J. Magn. Reson.*, Vol. 154, No. 1, 2002, pp. 85-100.
- [29] Basser, P.J. and C. Pierpaoli, "Microstructural and Physiological Features of Tissues Elucidated by Quantitative-Diffusion-Tensor MRI," *J. Magn. Reson. B*, Vol. 111, 3, 1996, pp. 209-219.
- [30] Ambrosio L. and V.M. Tortorelli, "On Approximation of Functionals Depending on Jumps by Quadratic Elliptic Functionals," *Boll. Un. Mat. Ital.*, Vol. 6-B, 1992, pp. 105-123.
- [31] Mumford, D. and J. Shah, "Boundary Detection by Minimizing Functionals," *Proc. of IEEE Conference on Computer Vision and Pattern Recognition*, 1985, pp. 22-26.
- [32] Mumford, D. and J. Shah, "Optimal Approximations by Piecewise Smooth Functions and Associated Variational Problems," *Communications on Pure and Applied Mathematics*, Vol. XLII, No. 5, 1989, pp. 577-684.
- [33] Shah, J., "A Common Framework for Curve Evolution, Segmentation and Anisotropic Diffusion," *Proc. IEEE Conference on Computer Vision and Pattern Recognition*, 1996, pp. 136-142.
- [34] Pien, H., M. Desai, J. Shah, "Segmentation of MR Images Using Curve Evolution and Prior Information," *Int'l J. Pattern Recognition and Artificial Intelligence*, Vol. 11, No. 8, 1997, pp. 1233-1245.
- [35] Desai, M., R. Mangoubi, J. Shah, W. Karl, D.N. Kennedy, H. Pien, A. Worth, "Functional MRI Activity Characterization Using Robust Non-Gaussian Detection and Curve Evolution," *IEEE Trans. Med. Imag.*, Vol. 21, No. 11, 2002, pp. 1402-1412.
- [36] Kogan, R., M. Desai, H. Pien, "Model-Based Visualization of Ultrasound Images," *AeroSense '99 Battlefield Biomedical Technologies Conference*, Orlando, FL, 1999.
- [37] Hasan, K.M., P.J. Basser, D.L. Parker, A.L. Alexander, "Analytical Computation of the Eigenvalues and Eigenvectors in DT-MRI," *J. Magn. Reson.*, Vol. 152, No. 1, 2001, pp. 41-47.
- [38] Pajevic, S. and C. Pierpaoli, "Color Schemes to Represent the Orientation of Anisotropic Tissues from Diffusion Tensor Data: Application to White Matter Fiber Tract Mapping in the Human Brain," *Magn. Reson. Med.*, Vol. 43, No. 6, 2000, pp. 921.
- [39] Szeszko, P.R., B.A. Ardekani, M. Ashtari, A.K. Malhotra, D.G. Robinson, R.M. Bilder, K.O. Lim, "White Matter Abnormalities in Obsessive-Compulsive Disorder: a Diffusion Tensor Imaging Study," *Arch. Gen. Psychiatry*, Vol. 62, No. 7, 2005, 782-90.
- [40] Makris, N., D.N. Kennedy, S. McInerney, A.G. Sorensen, R. Wang, V.S. Caviness, Jr., D.N. Pandya, "Segmentation of Subcomponents Within the Superior Longitudinal Fascicle in Humans: A Quantitative, In Vivo, DT-MRI Study," *Cereb. Cortex*, Vol. 15, No. 6, 2005, pp. 854-69.
- [41] Johansen-Berg, H., T.E. Behrens, E. Sillery, O. Ciccarelli, A.J. Thompson, S.M. Smith, P.M. Matthews, "Functional-Anatomical Validation and Individual Variation of Diffusion Tractography-Based Segmentation of the Human Thalamus," *Cereb. Cortex*, Vol. 15, No. 1, 2005, pp. 31-39.
- [42] Jones, D.K. and C. Pierpaoli, "Confidence Mapping in Diffusion Tensor Magnetic Resonance Imaging Tractography Using a Bootstrap Approach," *Magn. Reson. Med.*, Vol. 53, No. 5, 2005, pp. 1143-1149.
- [43] Kang, N., J. Zhang, E.S. Carlson, D. Gembris, "White Matter Fiber Tractography via Anisotropic Diffusion Simulation in the Human Brain," *IEEE Trans. Med. Imaging*, Vol. 24, No. 9, 2005, pp. 1127-37.
- [44] Tuch, D.S., T.G. Reese, M.R. Wiegell, N. Makris, J.W. Belliveau, V.J. Wedeen, "High Angular Resolution Diffusion Imaging Reveals Intravoxel White Matter Fiber Heterogeneity," *Magn. Reson. Med.*, Vol. 48, No. 4, 2002, pp. 577-582.
- [45] Jones, D.K., "The Effect of Gradient Sampling Schemes on Measures Derived from Diffusion Tensor MRI: a Monte Carlo Study," *Magn. Reson. Med.*, 2004, Vol. 51, No. 4, pp. 807-15.
- [46] Frank, L.R., "Anisotropy in High Angular Resolution Diffusion-Weighted MRI," *Magn. Reson. Med.*, Vol. 45, No. 6, 2001, pp. 935-939.
- [47] Buchel, C., "Perspectives on the Estimation of Effective Connectivity from Neuroimaging Data," *Neuroinformatics*, Vol. 2, No. 2, 2004, pp. 169-174.

- [48] McIntosh, A.R., "Contexts and Catalysts: A Resolution of the Localization and Integration of Function in the Brain," *Neuroinformatics*, Vol. 2, 2, 2004, pp. 175-82.
- [49] Valdes-Sosa, P.A., "Spatio-Temporal Autoregressive Models Defined over Brain Manifolds," *Neuroinformatics*, Vol. 2, No. 2, 2004, pp. 239-250.
- [50] Basser, P.J., J. Mattiello, D. Le Bihan, "Estimation of the Effective Self-Diffusion Tensor from the NMR Spin Echo," *Journal of Magnetic Resonance, Series B*, Vol. 103, 1994, pp. 247-254.
- [51] Basser, P.J. and C. Pierpaoli, "A Simplified Method to Measure the Diffusion Tensor from Seven MR Images," *Magn. Reson. Med.*, Vol. 39, No. 6, 1998, pp. 928-934.
- [52] Le Bihan, D., E. Breton, D. Lallemand, P. Grenier, E. Cabanis, M. Laval-Jeantet, "MR Imaging of Intravoxel Incoherent Motions: Applications to Diffusion and Perfusion in Neurologic Disorders," *Radiology*, Vol. 161, 1986, pp. 401-407.
- [53] Mattiello, J., P.J. Basser, D. Le Bihan, "The b Matrix in Diffusion Tensor Echo-Planar Imaging," *Magn. Reson. Med.*, Vol. 37, No. 2, 1997, pp. 292-300.
- [54] Moseley, M.E., Y. Cohen, J. Kucharczyk, J. Mintorovitch, H.S. Asgari, M.R. Wendland, J. Tsuruda, D. Norman, "Diffusion-Weighted MR Imaging of Anisotropic Water Diffusion in Cat Central Nervous System," *Radiology*, Vol. 176, 1990 pp. 439-446.
- [55] Pierpaoli, C., P. Jezzard, P.J. Basser, A. Barnett, G. Di Chiro, "Diffusion Tensor MR Imaging of the Human Brain," *Radiology*, Vol. 201, No. 3, 1996, pp. 637-648.
- [56] Stejskal, E.O. and J.E. Tanner, "Diffusion Measurements: Spin Echoes in the Presence of a Time-Dependent Field Gradient," *J. Chem. Phys.*, Vol. 42, No. 1, 1965, pp. 288-292.
- [57] Turner, R.; D. Le Bihan, J. Maier, R. Vavrek, L.K. Hedges, J. Pekar, "Echo-Planar Imaging of Intravoxel Incoherent Motion," *Radiology*, Vol. 177, No. 2, 1990, pp. 407-414.

(l-r) Mukund N. Desai and
Rami S. Mangoubi

bios

Mukund Desai is a Distinguished Member of the Technical Staff at Draper Laboratory. He has led research in optimal control, planning, estimation, optimal and robust detection, and image processing. His research work found novel applications at Draper in aircraft flight path management, path planning, battlefield management, mine hunting, target tracking, and distributed sensing. He holds two patents for helicopter swash-plate control and for finite capacity interaction processes. He has three more patents under filing. He has numerous technical publications, including two book chapters. Current research activities include the development of robust non-Gaussian and nonlinear signal modeling, learning, and detection, with application to chemical sensing, image and signal processing. His current work in multidimensional estimation has been applied to simultaneous denoising and segmentation of structural, functional magnetic resonance images and diffusion tensor images. He is also interested in ad hoc communication between distributed sensors, with application to the detection of transient phenomena. He also supervises graduate students conducting their research at Draper. He received BS and MS degrees with distinction from the Indian Institute of Science (IISc), Bangalore, India, and a PhD in Applied Mathematics from Harvard University.

David N. Kennedy is an Associate Professor of Neurology at the Harvard Medical School, and jointly appointed in the Neurology and Radiology Departments at the MGH. He has extensive expertise in the development of image analysis techniques and co-founded the Center for Morphometric Analysis at MGH. He has participated in the advent of such technologies as MRI-based morphometric analysis (1989), functional MRI (1991), and diffusion tensor pathway analysis (1998). He has long-standing experience with the development of neuroinformatics resources (Internet Brain Volumetric Database, Internet Brain Segmentation Repository, Internet Analysis Tools Registry), is co-Principal Investigator of the morphometry Biomedical Informatics Research Network (mBIRN), has been a Human Brain Project grant recipient since 1996, and is a founding editor of *Neuroinformatics*, which debuted in 2003.

Rami Mangoubi is a Senior Member of the Technical Staff at Draper Laboratory. He has worked on problems and led projects in operations research, control, alignment and calibration, and statistical signal detection, with a wide range of applications including computer networks, control of and failure detection in autonomous and space vehicles, biochemical sensing, magnetic resonance brain imaging and components mathematical model development and validation. Earlier in his career, he introduced the use of robust game theoretic filters for failure detection in dynamic plants. Current research includes robust non-Gaussian signal detection and cellular imaging. His numerous publications include *Robust Estimation and Failure Detection: A Concise Treatment* (Springer Verlag, London, UK, 1998). He supervises graduate students conducting their research at Draper. Dr. Mangoubi was an invited plenary speaker for the 2000 International Federation of Automatic Control's (IFAC) SAFEPROCESS conference in Budapest, Hungary. He is currently a principal investigator on an NIH research grant in the area of cellular imaging. He is a member of the IFAC SAFEPROCESS Technical Committee and a senior member of AIAA. He received a BS in Mechanical Engineering, an MS in Operations Research, and a PhD in Detection, Estimation, and Control from MIT.



2006 published Papers

Aceti, J.; Bernstein, J.; Borenstein, J.T.; Clark, H.A.; Zapata, A.M.
Engineering Solutions to Problems of National Significance: Applying Biomedical Engineering Technologies to Healthcare Needs
Explorations, The Charles Stark Draper Laboratory, Inc., Fall 2006

Abramson, M.R.; Carter, D.W.; Collins, B.K.; Kolitz, S.E.; Miller, J.V.; Scheidler, P.J.; Strauss, C.M.
Operational Use of EPOS to Increase the Science Value of EO-1 Observation Data
6th Earth Science Technology Conference (ESTC), Baltimore, MD, June 26-29, 2006. Sponsored by: NASA's Earth-Sun Systems Technology Office (ESTO)

Armstrong, J.T.; Mozurkewich, D.; Hajian, A.R.; Johnston, K.J.; Thessin, R.N.; Peterson, D.M.; Hummel, C.A.; Gilbreath, G.C.
The Hyades Binary Theta Squared Tauri: Confronting Evolutionary Models with Optical Interferometry
Astronomical Journal, Vol. 131, No. 5, May 2006

Benson, D.A.; Rao, A.V.; Huntington, G.T.; Thorvaldsen, T. P.
Direct Trajectory Optimization and Costate Estimation via a Gauss Pseudospectral Method
AIAA Guidance, Navigation, and Control Conference, Keystone, CO, August 21-24, 2006

Bernstein, J.J.; Lee, T.W.; Rogomentich, F.J.; Bancu, M.G.; Kim, K.H.; Maguluri, G.; Bouma, B.E.; DeBoer, J.F.
Magnetic Two-Axis Micromirror for 3D OCT Endoscopy
2006 Solid State Sensors, Actuators, and Microsystems Workshop, Hilton Head, SC, June 4-8, 2006, pp. 7-10

Bettinger, C.J.; Orrick, B.; Misra, A.; Langer, R.; Borenstein, J.T.
Microfabrication of Poly (Glycerol-Sebacate) for Contact Guidance Applications
Biomaterials, Elsevier, Vol. 27, No. 12, April 2006, pp. 2558-2565

Bettinger, C.J.; Weinberg, E.J.; Kulig, K.M.; Vacanti, J.P.; Wang, Y.; Borenstein, J.T.; Langer, R.
Three-Dimensional Microfluidic Tissue-Engineering Scaffolds Using a Flexible Biodegradable Polymer
Advanced Materials, Vol. 18, No. 2, January 19, 2006, pp. 165-169

Bickford, J.A.
Extraction of Antiparticles Concentrated in Planetary Magnetic Fields. Phase I Study
NASA Institute for Advanced Concepts (NIAC) Fellows Meeting, March 8, 2006, Atlanta, GA

Bickford, J.; Schmitt, W.M.; Spjeldvik, W.N.; Gusev, A.; Pugacheva, G.I.; Martin, I.
Natural Sources of Antiparticles in the Solar System and the Feasibility of Extraction for High Delta-V Space Propulsion
New Trends in Astrodynamics and Applications, III, Princeton, NJ, August 16-18, 2006. Sponsored by: American Institute of Physics (AIP)

Borenstein, J.T.
The Role of Engineering in Advancing Health Care in the 21st Century
Presentation posted on Wentworth Institute of Technology's web site

Candler, R.N.; Duwel, A.; Varghese, M.; Chandorkar, S.; Hopcroft, M.; Park, W.T.; Kim, B.; Yama, G.; Partridge, A.; Lutz, M.; Kenny, T.W.
Impact of Geometry on Thermoelastic Dissipation in Micromechanical Resonant Beams
IEEE JMEMS, Vol. 15, No. 927, 2006

Carlen, E.T.; Weinberg, M.S.; Dube, C.E.; Zapata, A.M.; Borenstein, J.T.
Micromachined Silicon Plates for Sensing Molecular Interactions
Applied Physics Letters, AIP, Vol. 89, No. 17, October 23, 2006

Cernosek, R.W.; Robinson, A.L.; Cruz, D.Y.; Adkins, D.R.; Barnett, J.L.; Bauer, J.M.; Blain, M.G.; Byrnes, J.E.; Dirk, S.M.; Dulleck, G.R.; Ellison, J.A.; Fleming, J.G.; Hamilton, T.W.; Heller, E.J.; Howell, S.W.; Kottenstette, R.J.; Lewis, P.R.; Manginell, R.P.; Moorman, M.W.; Mowry, C.D.; Manley, R.G.; Okandan, M.; Rahimian, K.; Shelmidine, G.J.; Shul, R.J.; Simonson, R.J.; Sokolowski, S.S.; Spates, J.J.; Staton, A.W.; Trudell, D.E.; Wheeler, D.R.; Yelton, W.G.; Eds.: Thomas, G.; Zhong-Yang, C.

Micro-Analytical Systems for National Security Applications

Micro (MEMS) and Nanotechnologies for Space Applications, April 19-20, 2006, Kissimmee, Florida

Chen, D.; Lin, P.J.

Minimum Energy Path Planning for Ad Hoc Networks

Wireless Communications and Networking Conference (WCNC), Las Vegas, NV, April 3-6, 2006. Sponsored by: IEEE

Davis, C.E.; Krebs, M.D.; Tingley, R.D.; Zeskind, J.E.; Holmboe, M.E.; Kang, J.-M.
Alignment of Gas Chromatography-Mass Spectrometry Data by Landmark Selection from Complex Chemical Mixtures

Chemometrics and Intelligent Laboratory Systems, Vol. 81, No.1, March 2006, pp. 74-81

Desai, M.N.; Kennedy, D.N.; Mangoubi, R.S.; Shah, J.; Karl, C.; Worth, A.; Makris, N.; Pien, H.
Model-Based Variational Smoothing and Segmentation for Diffusion Tensor Imaging in the Brain
Neuroinformatics, Vol. 4, No. 3, 2006, pp. 217-234

Desai, M.N.; Mangoubi, R.S.; Kennedy, D.
Robust Constrained Non-Gaussian fMRI Detection
International Symposium on Biomedical Imaging from Nano to Macro, Arlington, VA, April 6-9, 2006. Sponsored by: IEEE

Dever, C.; Mettler, B.; Feron, E.; Popovic, J.; McConley, M.
Nonlinear Trajectory Generation for Autonomous Vehicles Via Parameterized Maneuver Classes
Journal of Guidance Control and Dynamics, Vol. 29, No. 2, March-April 2006, pp. 289-302

Duwel, A.E.; Candler, R.N.; Kenny, T.W.; Varghese, M.
Engineering MEMS Resonators with Low Thermoelastic Damping
Journal of Microelectromechanical Systems, IEEE, Vol. 15, No. 6, December 2006, pp. 1437-1445

Fucetola, C.; Carter, D.J.
Process Latitude of Deep-Ultraviolet Conformable Contact Photolithography

50th International Conference on Electron, Ion, and Photon Beam Technology and Nanofabrication, Baltimore, MD, May 30-June 2, 2006

Fuhrman, L.R.
Future of Lunar Landing Systems

29th Rocky Mountain Guidance and Control Conference, Breckenridge, CO, February 4-8, 2006, *Advances in the Astronautical Sciences*, Vol. 125, 2006, pp. 213-223. Sponsored by: American Astronautical Society (AAS)

Gustafson, D.E.; Elwell Jr., J.M.; Soltz, J.A.
Innovative Indoor Geolocation Using RF Multipath Diversity

Position Location and Navigation Symposium (PLANS), San Diego, CA, April 25-27, 2006. Sponsored by IEEE/ION

Harjes, D.I.; Clark, H.A.
Novel Optical Biosensor Arrays for Toxicity Screening in Drug Discovery

57th Pittsburgh Conference on Analytical Chemistry and Applied Spectroscopy (PITTCON), Orlando, FL, March 12-17, 2006

Hattis, P.D.; Campbell, D.P.; Carter, D.W.; McConley, M.; Tavan, S.
Providing Means for Precision Airdrop Delivery from High Altitude

AIAA Guidance, Navigation, and Control Conference, Keystone, CO, August 21-24, 2006

Hawkins, A.M.; Fill, T.J.; Proulx, R.J.; Feron, E.M.J.
Constrained Trajectory Optimization for Lunar Landing
Spaceflight Mechanics 2006, Tampa, FL, January 22-26, 2006, *Advances in the Astronautical Sciences*, Part I, Vol. 124, 2006, pp. 815-836

Heinrich, N.; Case, A.; Stein, R.L.; Clark, H.A.
Optical Sensors for the Monitoring of Enzymatic Reaction for Drug Screening in Neurodegenerative Disease
57th Pittsburgh Conference on Analytical Chemistry and Applied Spectroscopy (PITTCON), Orlando, FL, March 12-17, 2006

Hildebrant, R.
Framework for Autonomy
Optics East, International Symposium, Boston, MA, October 1-4, 2006. Sponsored by: SPIE

Hopkins III, R.E.

MEMS Inertial Technology. A Short Course
PLANS, San Diego, CA, April 25-27, 2006. Sponsored by: IEEE/ION; Joint Navigation Conference (JNC), Las Vegas, NV, May 1-4, 2006. Sponsored by: Joint Service Data Exchange (JSDE)

Huntington, G.T.; Rao, A.V.

Optimal Reconfiguration of a Tetrahedral Formation Via a Gauss Pseudospectral Method
Advances in the Astronautical Sciences, AAS, Vol. 123, Part II, 2006, pp. 1337-1358

Huntington, G.T.; Benson, D.A.; Rao, A.V.

Post-Optimality Evaluation and Analysis of a Formation Flying Problem Via a Gauss Pseudospectral Method
Advances in the Astronautical Sciences - Proceedings of the AAS/AIAA Astrodynamics Conference, Vol. 123, No. 2, 2006

Jang, J-W.; Fitz-Coy, N.G.

Differential Games: A Pole Placement Approach
Proceedings of the University at Buffalo, State University of New York/AAS Malcolm D. Shuster Astronautics Symposium, Grand Island, NY, Vol. 122, 2006

Johnson, M.C.

Parameterized Approach to the Design of Lunar Lander Attitude Controllers
Guidance, Navigation, and Control Conference, Keystone, CO, August 21-24, 2006. Sponsored by: AIAA

Keegan, M.E.; Saltzman, W.M.

Surface-Modified Biodegradable Microspheres for DNA Vaccine Delivery
Methods in Molecular Medicine, Vol. 127; *DNA Vaccines: Methods and Protocols*, 2nd ed., Humana Press, 2006

Key, R.; Kahn, A.C., Deutsch, O.L.

Midcourse Phase Inventory Management with Uncertain Threats
Missile Defense Conference & Exhibit, Washington, DC, March 20-24, 2006. Sponsored by: AIAA

Khademhossini, A.; Bettinger, C.J.; Karp, J.M.;

Yeh, J.; Ling, Y.; Borenstein, J.T.; Fukuda, J.;

Langer, R.

Interplay of Biomaterials and Micro-scale Technologies for Advancing Biomedical Applications
Journal of Biomaterials Science, Polymer Edition, Vol. 17, No. 11, November 2006

Khademhossini, A.; Langer, R.; Borenstein, J.T.;

Vacanti, J.P.

Microscale Technologies for Tissue Engineering and Biology

Proceedings of the National Academy of Sciences of the USA, Vol. 103, No. 8, February 2006

Kondoleon, C.A.; Marinis, T.F.

Package Design for a Miniaturized Capacitive-Based Chemical Sensor

39th International Symposium on Microelectronics, San Diego, CA, October 8-12, 2006. Sponsored by: International Microelectronics and Packaging Society (IMAPS)

Kourepennis, A.S.; Barbour, N.M.; Hopkins III, R.E.;

Serna, F.J.; Varghese, M.

MEMS Technologies and Applications

International Test and Evaluation Association (ITEA) Annual Technology Review Conference, Cambridge, MA, August 8-10, 2006. Sponsored by: ITEA

Krebs, M.D.; Mansfield, B.; Yip, P.; Cohen, S.;

Sonenshein, A.L.; Hitt, B.A.; Davis, C.E.

Novel Technology for Rapid Species-Specific Detection of Bacillus Spores

Biomolecular Engineering, Vol. 23, February 2006, pp. 119-127

Krebs, M.D.; Kang, J.J.; Cohen, S.; Lozow, J.B.;

Tingley, R.D.; Davis, C.E.

Two-Dimensional Alignment of Differential Mobility Spectrometer Data

Sensors and Actuators B (Chemical), Vol. 119, No. 2, December 2006, pp. 475-482

Landis, D.L.; Thorvaldsen, T.P.; Fink, B.J.;

Sherman, P.G.; Holmes, S.M.

Deep Integration Estimator for Urban Ground Navigation

PLANS, San Diego, CA, April 25-27, 2006. Sponsored by: IEEE/ION

Lento, C.; McCarragher, B.; Magee, R.

The CERAS Pod Test Cell for Simultaneous Environment Testing

AIAA Missile Sciences Conference, Monterey, CA, November 14-16, 2006

Lim, S.Y.; Miotto, P.

Actuator Allocation Algorithm Using Interior Linear Programming

Guidance, Navigation, and Control Conference, Keystone, CO, August 21-24, 2006. Sponsored by: AIAA

- Lim, S.Y.**
Complementary Roll/Yaw Attitude Controller for Three-Axis Authority Momentum Spacecraft Guidance, Navigation, and Control Conference, Keystone, CO, August 21-24, 2006. Sponsored by: AIAA
- Lymar, D.S.; Neugebauer, T.C.; Perreault, D.J.**
Coupled-Magnetic Filters with Adaptive Inductance Cancellation
IEEE Transactions on Power Electronics, Vol. 21, No. 6, November 2006, pp. 1529-1540
- Marinis, T.F.; Soucy, J.W.; Hanson, D.S.; Pryputniewicz, R.J.; Marinis, R.T.; Klemptner, A.R.**
Isolation of MEMS Devices from Package Stresses by Use of Compliant Metal Interposers
56th Electronic Components and Technology Conference (ECTC), San Diego, CA, May 30-June 2, 2006. Sponsored by: IEEE, Components, Packaging, and Manufacturing Technology (CPMT) Society
- Masterson, R.A.; Miller, D.**
Dynamic Tailoring and Tuning of Structurally-Connected TPF Interferometer
Proceedings of the SPIE, Vol. 6271, July 2006
- Masterson, R.A.; Miller, D.**
Hardware Tuning for Dynamic Performance Through Isoperformance Updating
47th Structures, Structural Dynamics, and Materials Conference, Newport, RI, May 1-4, 2006. Sponsored by: AIAA, ASME, American Society of Computer Engineers (ASCE), American Helicopter Society (AHS), ASC
- Mather, R.A.; Matlis, J.**
Alternative Approach to Testing Embedded Real-Time Software
America's Virtual Product Development (VPD) Conference: Evolution to Enterprise Simulation, Huntington Beach, CA, July 17-19, 2006. Sponsored by: MSC Software
- McAlpine, J.; Najjar, R.C.; Thompson, J.**
Hazmat Response: Victim Extrication, Trauma Control, and Decontamination in a Laboratory Setting
Proceedings of the 24th College and University Hazardous Waste Conference, August 6-9, 2006
- McCarragher, B.; Chen, B.; Chamberlin, S.; Magee, R.**
The Simultaneous Application of Vibration, Shock, and Thermal Missile Environments
AIAA Missile Sciences Conference, Monterey, CA, November 14-16, 2006
- Mettler, B.; Feron, E.; Popovic, J.; McConley, M.**
Nonlinear Trajectory Generation for Autonomous Vehicles via Parameterized Maneuver Classes
Journal of Guidance Control and Dynamics, AIAA, Vol. 29, No. 2, March-April, 2006
- Miller, J.W.; Lommel, P.H.**
Biomimetic Sensory Abstraction Using Hierarchical Quilted Self-Organizing Maps
Intelligent Robots and Computer Vision XXIV: Algorithms, Techniques, and Active Vision, Boston, MA, October 1-4, 2006. Sponsored by: SPIE
- Mitchell, I.T.; Gorton, T.B.; Taskov, K.; Drews, M.E.; Luckey, D.; Osborne, M.L.; Page, L.A.; Norris, H.L., III; Shepperd, S.W.**
GN&C Development of the XSS-11 Micro-Satellite for Autonomous Rendezvous and Proximity Operations
29th Guidance and Control Conference, Breckenridge, CO, February 4-8, 2006. Sponsored by: AAS
- Neugebauer, T.C.; Perreault, D.J.**
Parasitic Capacitance Cancellation in Filter Inductors
Transactions on Power Electronics, IEEE, Vol. 21, No. 1, January 2006
- Pahlavan, K.; Akgul, F.O.; Heidari, M.; Hatami, A.; Elwell, J.M.; Tingley, R.D.**
Indoor Geolocation in the Absence of Direct Path
IEEE Wireless Communications, Vol. 13, No. 6, December 2006, pp. 50-58
- Perry, H.C.; Brady, T.M.; Breton, R.S.; Brodeur, S.J.; Brown, R.A.; Buckley, S.; Erikson, E.R.; Fuhrman, L.R.; Jackson, T.R.; Kochocki, J.A.; Turney, D.J.; Wyman Jr, W.F.**
Engineering Solutions to Problems of National Significance. Embedded Software and Draper IDEAS Explorations, The Charles Stark Draper Laboratory, Inc., Spring 2006
- Pierquet, B.J.; Neugebauer, T.C.; Perreault, D.J.**
Inductance Compensation of Multiple Capacitors with Application to Common- and Differential-Mode Filters
IEEE Transactions on Power Electronics, Vol. 21, No. 6, November 2006, pp. 1815-1824
- Putnam, Z.R.; Braun, R.D.; Bairstow, S.H.; Barton, G.H.**
Improving Lunar Return Entry Footprints Using Enhanced Skip Trajectory Guidance
Space 2006 Conference, San Jose, CA, September 19-21, 2006. Sponsored by: AIAA

- Ricard, M.J.; Nervegna, M.F.**
Risk-Aware Mixed-Initiative Dynamic Replanning (RMDR) Program Update
 Unmanned Systems North America, Orlando, FL, August 29-31, 2006. Sponsored by: Association for Unmanned Vehicle Systems International (AUVSI)
- Roth, K.W.; Llana P.; Westphalen D.; Quartararo, L.; Feng M.Y.**
Advanced Controls for Commercial Buildings: Barriers and Energy Savings Potential
Energy Engineering, 2006, Vol. 103, No. 6, pp. 6-36
- Rzepniewski, A.K.; Andrews, G.L.**
Legged Robot Motion with Explicit Stability Constraints: Theory and Application
 Unmanned Systems North America, Orlando, FL, August 29-31, 2006. Sponsored by: AUVSI
- Sawyer, W.D.; Prince, M.S.**
Silicon on Insulator Inertial MEMS Device Processing
 MOEMS-MEMS Micro & Nanofabrication, Photonics West, San Jose, CA, January 21-26, 2006. Sponsored by: SPIE
- Schmidt, G.T.**
Future Navigation Systems: INS/GPS Technology Trends
 The Charles Stark Draper Laboratory, Inc., 2006
- Schmitt, W.M.; Larsen, D.E.; Brown, D.N.; Harris, Bernard S.; Zuckerman, H.L.**
Importance of Secondary Scattering in X-Ray Transport for Shadowing Analysis
 Hardened Electronics and Radiation Technology (HEART) Conference, Santa Clara, CA, March 6-10, 2006. Sponsored by: Department of Defense (DoD)/Department of Energy (DoE).
- Serklaud, D.K.; Peake, G.M.; Geib, K.M.; Lutwak, R.; Garvey, R.M.; Varghese, M.; Mescher, M.**
VCSELS for Atomic Clocks
 Vertical-Cavity Surface-Emitting Lasers X, *Proceedings of SPIE*, January 25-26, 2006, San Jose, CA
- Springmann, P.; Proulx, R.; Fill, T.**
Lunar Descent Using Sequential Engine Shutdown
 AIAA/AAS Astrodynamics Specialist Conference and Exhibit, Keystone, CO, August 21-24, 2006
- Stoner, R.; Walsworth, R.**
Atomic Physics - Collisions Give Sense of Direction
Nature Physics, Vol. 2, No. 1, January 2006, pp. 17-18
- Stubbs, A.; Vladimerou, V.; Fulford, A.T.; King, D.; Strick, J.; Dullerud, G.E.**
Multivehicle Systems Control over Networks
IEEE Control Systems, Vol. 26, No. 3, 2006, pp 56-69
- Tawney, J.; Hakimi, F.; Willig, R.L.; Alonzo, J.; Bise, R.T.; DiMarcello, F.; Monberg, E.M.; Stockert, T.; Trevor, D.J.**
Photonic Crystal Fiber IFOGs
 18th International Conference on Optical Fiber Sensors, Cancun, Mexico, October 23-27, 2006. Sponsored by: Optical Society of America (OSA)
- Tetewsky, A.; Dow, B.; Bogner, T.; Mitchell, M.; Daley, S.; Shearer, J.**
Evaluating HYGPSIM's New GPS/INS HWIL Prediction Capabilities with 2004 Reentry Vehicle Flight Data
 AIAA Missile Science Conference (Classified) Monterey, CA, November 14-16, 2006
- Weinberg, E.J.; Kaazempur-Mofrad, M.R.**
Large-Strain Finite-Element Formulation for Biological Tissues with Application to Mitral Valve Leaflet Tissue Mechanics
Journal of Biomechanics, Vol. 39, No. 8, 2006, pp. 1557-1561
- Weinberg, M.S.; Kourepenis, A.S.**
Error Sources in In-Plane Silicon Tuning-Fork MEMS Gyroscopes
IEEE Journal of Microelectromechanical Systems, Vol. 15, No. 3, June 2006, pp. 479-491
- Weinberg, M.S.; Wall, C.; Robertsson, J.; O'Neil, E.W.; Sienko, K.; Fields, R.P.**
Tilt Determination in MEMS Inertial Vestibular Prosthesis
Journal of Biomechanical Engineering, Transactions of the ASME, Vol. 128, No. 6, December 2006, pp. 943-56.
- Weinberg, M.S.**
Tuning Fork MEMS Gyroscopes
 Presented at Tufts University, October 12, 2006

patents

Introduction

Draper Laboratory is well known for integrating widely diverse technical capabilities and technologies into innovative and creative solutions for problems of national importance. Draper's scientists and engineers are actively encouraged to advance the application of science and technology, to expand the functions of existing technologies, and to create new ones.

Draper has an established patent policy and understands the value of patents in directing attention to individual accomplishments. Disclosing inventions is an important step in documenting these creative efforts and is required under Laboratory contracts and by an agreement with Draper that all employees sign. Pursuing patent protection enables the Laboratory to pursue its strategic mission and to recognize its employees' valuable contributions to advancing the state-of-the-art in their technical areas. An issued patent is also recognition by a critical third party (the U.S. Patent Office) of innovative work for which the inventor should be justly proud.

Through December 31, 2006, 1297 Draper patent disclosures have been submitted to the Patent Committee since 1973; 655 of those were approved by Draper's Patent Committee for further patent action. As of December 31, a total of 4804 patents have been granted for inventions made by Draper personnel. Twelve patents were issued for calendar year 2006.

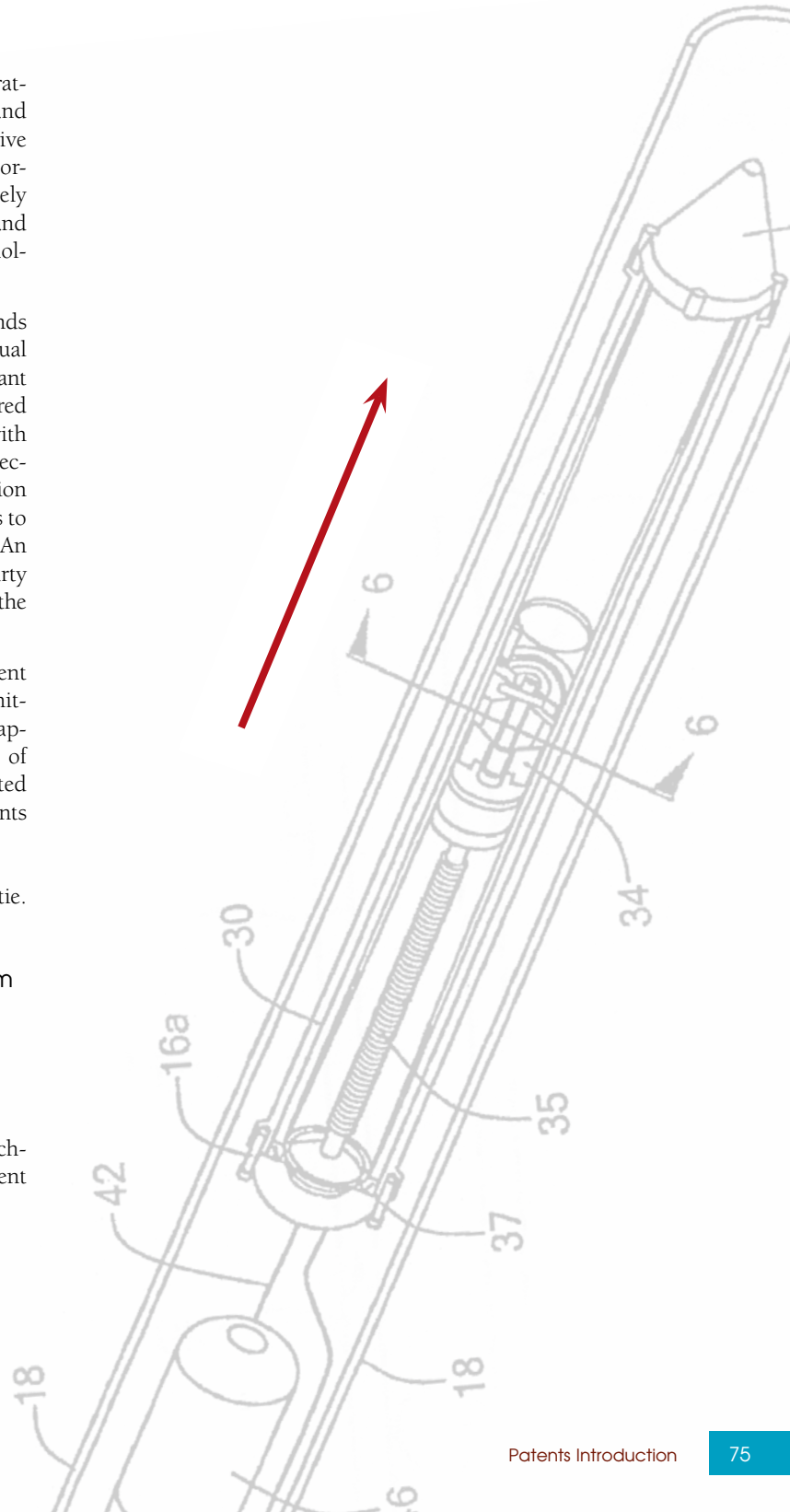
This year's competition for Best Patent resulted in a tie. The featured patents are:

Multi-gimbaled borehole navigation system

and

Flexural plate wave sensor

The following pages present an overview of the technology covered in each patent and the official patent abstracts issued by the U.S. Patent Office.



Multi-Gimbaled Borehole Navigation System

Patent # 7,093,370 B2 Date Issued: August 22, 2006

Mitchell L. Hansberry, Michael E. Ash, Richard T. Martorana

This invention addresses the need to monitor and guide the direction of a drill bit so that a borehole is created where desired. To determine the location of a drill bit in a borehole, the position and attitude must be known, including the vertical orientation and the north direction. Typically, gyroscopes can be used to determine the north direction, and accelerometers can be used to determine the vertical orientation. Prior systems have used single-orientation gyroscopes and/or single orientation accelerometers due to size limitations. However, these systems can suffer from long-term bias stability problems.

Many prior systems attempted to determine the drill bit's location accurately and efficiently, but each system had limitations. For example, where the internal diameter of a drill pipe is not large enough to fit the optimal number of typical navigation sensors, one prior system removed the drill bit from the borehole and lowered a monitoring tool down the borehole to determine its location. However, it is costly to stop drilling and spend time removing the drill bit to take measurements with the monitoring tool. Other systems used single-axis accelerometers to determine the vertical orientation of the drill bit. However, an accelerometer system cannot determine north, which is necessary to determine the full location of a borehole. Another prior design used magnetometers to determine the magnetic field direction from which the direction of north is approximated. However, such systems must correct for magnetic interference and magnetic materials used in the drill pipe and can suffer accuracy degradation due to the Earth's changing magnetic field.

This patent describes a novel navigation borehole system that can determine position and attitude for any orientation in a borehole using multiple gimbals that contain solid-state or other gyros and accelerometers. The navigation system includes a housing that can be placed within the smaller diameter drill pipes used toward the bottom of a borehole, an outer gimbal connected to the housing, and at least two or more stacked inner gimbals nested in and connected to the outer gimbal. The inner gimbals each have an axis parallel to one another and perpendicular to the outer gimbal. The inner gimbals contain electronic circuits, gyros, and accelerometers whose input axes span three-dimensional space. The system includes outer and inner gimbal drive systems to maintain the gyro and accelerometer input axes as substantially orthogonal triads and a processor that is responsive to the gyro accelerometer circuits to determine the attitude and the position of the housing in the borehole.

This borehole navigation system can average out navigation errors due to gyro and accelerometer bias, gyro scale factor, and input-axis alignment errors, and allows gyro and accelerometer bias and gyro scale-factor calibration as well as attitude determination during gyrocompassing. This invention also provides long-term performance accuracy with only short-term requirements on sensor accuracy, can determine position and attitude while drilling, when the drill bit is stopped, when the drill bit is inserted or withdrawn, as well as while logging, both descending and ascending on a log line after the drill bit has been withdrawn.



US007093370B2

(12) **United States Patent**
Hansberry et al.

(10) **Patent No.:** **US 7,093,370 B2**
(45) **Date of Patent:** ***Aug. 22, 2006**

- (54) **MULTI-GIMBALED BOREHOLE NAVIGATION SYSTEM**
- (75) Inventors: **Mitchell L. Hansberry**, Southborough, MA (US); **Michael E. Ash**, Lexington, MA (US); **Richard T. Martorana**, Andover, MA (US)
- (73) Assignee: **The Charles Stark Draper Laboratory, Inc.**, Cambridge, MA (US)

4,454,756 A	6/1984	Sharp et al.
4,537,067 A	8/1985	Sharp et al.
4,594,790 A	6/1986	Engebretson
4,696,112 A	9/1987	Hoffman
4,756,088 A	7/1988	Russell et al.
4,987,684 A	1/1991	Andreas et al.
5,126,812 A	6/1992	Greiff
5,156,056 A	10/1992	Pittman et al.
5,349,855 A	9/1994	Bernstein et al.

(*) Notice: Subject to any disclaimer, the term of this patent is extended or adjusted under 35 U.S.C. 154(b) by 0 days.

This patent is subject to a terminal disclaimer.

(Continued)

FOREIGN PATENT DOCUMENTS

WO WO 03/031912 A2 4/2003

OTHER PUBLICATIONS

U.S. Appl. No. 10/768,309, filed Jan. 30, 2004, Ash et al.

(Continued)

Primary Examiner—Christopher W. Fulton
(74) *Attorney, Agent, or Firm*—Iandiorio & Teska

(21) Appl. No.: **10/987,117**

(22) Filed: **Nov. 12, 2004**

(65) **Prior Publication Data**
US 2005/0126022 A1 Jun. 16, 2005

Related U.S. Application Data

(63) Continuation-in-part of application No. 10/632,717, filed on Aug. 1, 2003, now Pat. No. 6,895,678.

- (51) **Int. Cl.**
G01C 19/00 (2006.01)
- (52) **U.S. Cl.** **33/313; 33/321; 33/366.13**
- (58) **Field of Classification Search** **33/313, 33/304, 318, 321, 322, 323, 328, 366.11, 33/366.12, 366.13, 542, 544**
See application file for complete search history.

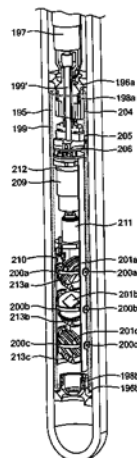
(56) **References Cited**
U.S. PATENT DOCUMENTS

3,079,696 A	3/1963	van Rooyen
3,883,788 A	5/1975	Storey, Jr.
4,052,654 A	10/1977	Kramer et al.
4,071,959 A	2/1978	Russell et al.

(57) **ABSTRACT**

An omnidirectional borehole navigation system is provided that includes a housing that can be placed within the smaller diameter drill pipes used towards the bottom of a borehole, an outer gimbal connected to the housing, and at least two or more stacked inner gimbals that are nested in and connected to the outer gimbal, the inner gimbals each having an axis parallel to one another and perpendicular to the outer gimbal. The inner gimbals contain electronic circuits, gyros whose input axes span three dimensional space, and accelerometers whose input axes span three dimensional space. There are an outer gimbal drive system, an inner gimbal drive system for maintaining the gyro input axes and the accelerometer input axes as substantially orthogonal triads, and a processor responsive to the gyro circuits and the accelerometer circuits to determine the attitude and the position of the housing in the borehole.

44 Claims, 16 Drawing Sheets



(l-r) Mitchell L. Hansberry
and Richard T. Martorana



bios

Richard T. Martorana is a Distinguished Member of the Technical Staff and the Technical Director for the WASP Program. With over 39 years of research, design, and development experience, he has directed and managed programs for NASA, USAF, DARPA, NAVSEA, and others. He was responsible for the thermal design of the Trident II inertial measurement unit (IMU). His responsibilities have included: Section Chief for Fluid Mechanics and Thermal Engineering, Division Manager for Mechanical Design and Analysis, and Director of Systems Integration, Test, Evaluation, and Quality Management. He holds three U.S. patents in the areas of mechanical and thermal design. Mr. Martorana has BS and MS degrees in Mechanical Engineering from Columbia University and MIT, respectively, an MBA focused on management of innovation from Northeastern University, and he is a graduate of Harvard Business School's Program for Management Development.

Mitchell L. Hansberry is a Senior Member of the Technical Staff and a Mechanical Design Engineer with 25 years experience at Draper Laboratory. Specializing in the development of hardware configurations to solve system-level problems, he has been the Lead Mechanical Designer on many projects involving navigation instruments and systems, space hardware, and biomedical mechanisms. He has a BS in Mechanical Engineering from SUNY at Stony Brook.

Michael E. Ash was a Principal Member of the Technical Staff in the System Integration, Evaluation, and Test Division, where he worked on inertial sensor and system modeling, simulation, and testing. Previously, he worked at the MIT Lincoln Laboratory on an interplanetary radar test of general relativity and on-satellite orbit determination. He was Chair of the Accelerometer Committee of the IEEE/Aerospace Electronics System Society (AESS) Gyro and Accelerometer Panel and an Associate Fellow of the AIAA. He received a BS from MIT and a PhD from Princeton University, both in Mathematics.

Flexural Plate Wave Sensor

Patent # 7,109,633 B2 Date Issued: September 19, 2006

Marc S. Weinberg, Brian T. Cunningham, Eric M. Hildebrandt

This patent describes an improved flexural plate wave (FPW) sensor that includes a thin flexural plate with drive teeth disposed across its entire length. Further improvements associated with drive combs of varying tooth length are described. This improved FPW sensor reduces the number of eigenmodes excited in the flexural plate and outputs a single pronounced peak or a peak much larger than any of the other peaks and a distinct phase. This distinct peak simplifies the operating and designing associated drive and sense electronics and improves stability by eliminating erroneous readings due to interference created by mode hopping between eigenmodes.

The FPW sensor includes a diaphragm or plate that is driven so that it oscillates at frequencies determined by a comb pattern and the flexural plate geometry. The comb pattern is disposed over the flexural plate and establishes electric fields that interact with the plate's piezoelectric properties to excite motion. The eigenmodes describe the diaphragm displacements, which exhibit spatially distributed peaks. Each eigenmode consists of n half sine periods along the diaphragm's length. A typical FPW sensor can be excited to eighty or more eigenmodes. In a typical FPW eigenmode, the plate deflection consists of many sinusoidal (or nearly sinusoidal) peaks.

Previous flexure plate wave sensor designs typically include drive combs at one end of the plate and sense combs at the other end. The drive combs of these devices typically cover only 25% to 40% of the total plate length. When the number of drive teeth is small compared to the number of eigenmodes peaks, the small number of drive teeth can align with several eigenmodes. Not only are the eigenmodes perfectly aligned with the comb teeth excited, but other eigenmodes are also excited. In signal processing and spectral analysis, this effect is known as leakage. The increased number of eigenmodes excited in the FPW sensor produces a series of resonance peaks of similar amplitude and irregular phase, increasing design complexity and the operation of such FPW sensors. Other previous FPW designs employ drive and sense combs at opposite ends of the flexural plate and rely on analysis based on surface acoustic waves (SAW) where the waves propagate away from the drive combs and toward the sense combs, and back reflections are regarded as interference. A disadvantage is that SAW theory does not account for the sensor's numerous small peaks and the electronics' locking onto different eigenmodes depending on noise or starting conditions.

Bioscale has licensed the FPW technology from Draper and will introduce a commercial product.



US007109633B2

(12) **United States Patent**
Weinberg et al.

(10) **Patent No.:** **US 7,109,633 B2**
(45) **Date of Patent:** **Sep. 19, 2006**

- (54) **FLEXURAL PLATE WAVE SENSOR**
- (75) Inventors: **Marc S. Weinberg**, Needham, MA (US); **Brian Cunningham**, Lexington, MA (US); **Eric Hildebrant**, Watertown, MA (US)
- (73) Assignee: **Charles Stark Draper Laboratory, Inc.**, Cambridge, MA (US)
- (*) Notice: Subject to any disclaimer, the term of this patent is extended or adjusted under 35 U.S.C. 154(b) by 0 days.

(56) **References Cited**

U.S. PATENT DOCUMENTS

4,454,440 A *	6/1984	Cullen	310/313 R
4,783,821 A *	11/1988	Muller et al.	381/173
5,216,312 A *	6/1993	Baer et al.	310/313 D
5,552,655 A *	9/1996	Stokes et al.	310/330
5,852,337 A *	12/1998	Takeuchi et al.	310/328
5,956,292 A *	9/1999	Bernstein	367/140
6,091,182 A *	7/2000	Takeuchi et al.	310/330
6,323,580 B1 *	11/2001	Bernstein	310/324

* cited by examiner

(21) Appl. No.: **10/675,398**

Primary Examiner—Mark Budd

(22) Filed: **Sep. 30, 2003**

(74) *Attorney, Agent, or Firm*—Iandiorio & Teska

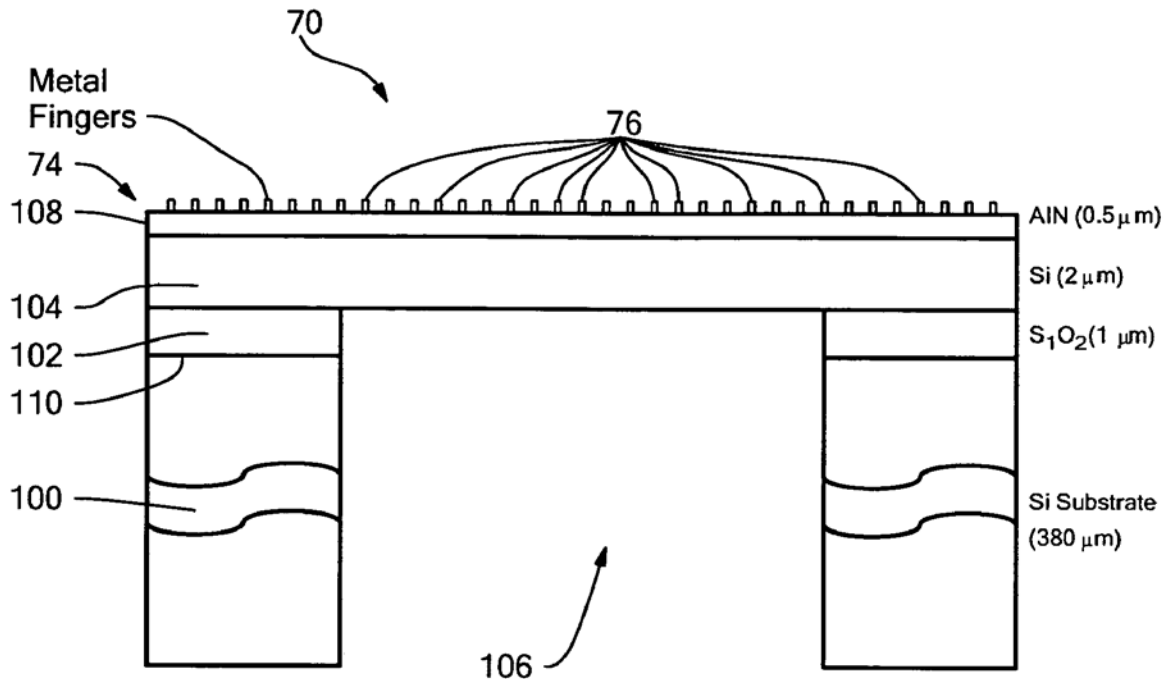
(65) **Prior Publication Data**
US 2005/0067920 A1 Mar. 31, 2005

(57) **ABSTRACT**

- (51) **Int. Cl.**
H01L 41/08 (2006.01)
- (52) **U.S. Cl.** **310/313 B**; 310/313 R; 310/324
- (58) **Field of Classification Search** 310/322, 310/328, 330–332, 313 R, 313 B, 366
See application file for complete search history.

A flexural plate wave sensor including a flexural plate having a length and a width and a comb pattern over the flexural plate with drive teeth disposed across the entire length of the flexural plate to reduce the number of eigenmodes excited in the plate and thereby simplifying the operation and design of the flexure plate wave sensor.

56 Claims, 22 Drawing Sheets



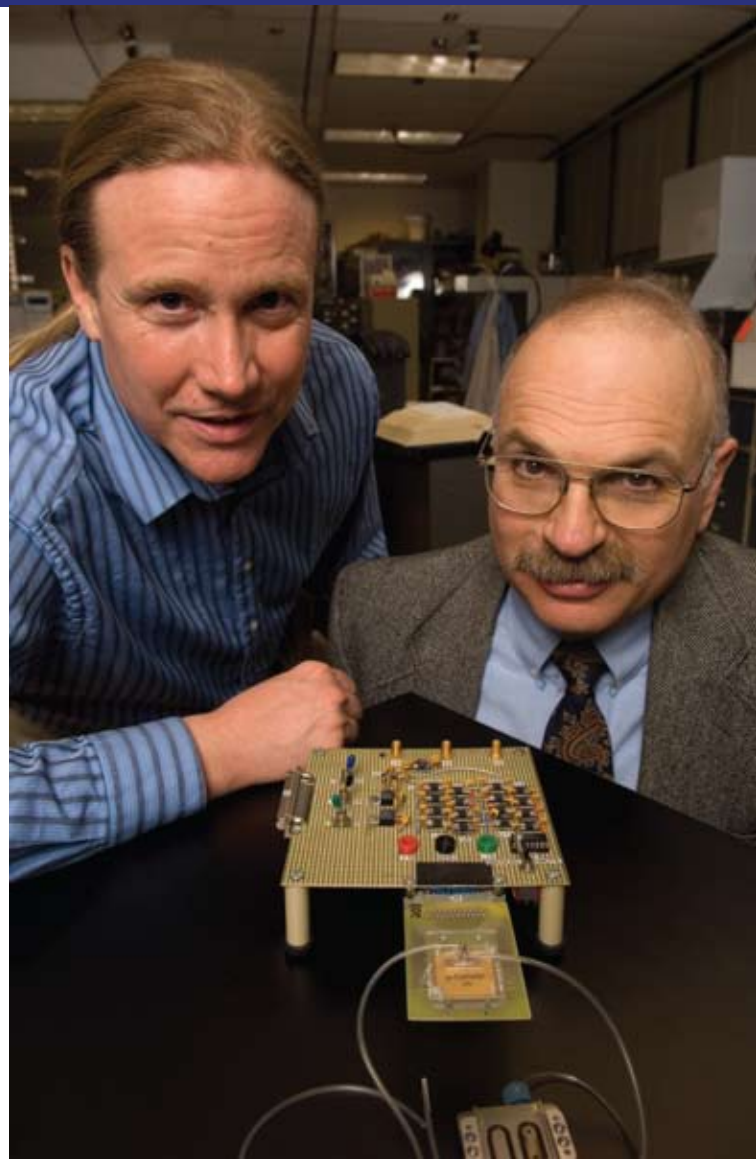
(l-r) Eric M. Hildebrant and
Marc S. Weinberg

bios

Marc S. Weinberg is a Laboratory Technical Staff Member at Draper Laboratory. He has been responsible for the design and testing of a wide range of traditional micromechanical gyroscopes, accelerometers, hydrophones, microphones, angular displacement sensors, chemical sensors, and biomedical devices. He served in the United States Air Force at the Aeronautical System Division, Wright-Patterson Air Force Base during 1974 and 1975, where he applied modern and classical control theory to design turbine engine controls, and at the Air Force Institute of Technology, where he taught gas dynamics and feedback control. He holds 25 patents with 12 additional in application. He has been a member of ASME since 1971. Dr. Weinberg received BS (1971), MS (1971), and PhD (1974) degrees in Mechanical Engineering from MIT where he held a National Science Foundation Fellowship.

Brian T. Cunningham was a Principal Member of the Technical Staff at Draper Laboratory. Currently, he is an Associate Professor of Electrical and Computer Engineering at the University of Illinois at Urbana-Champaign, where he is the Director of the Nano Sensors Group. His group focuses on the development of photonic crystal-based transducers, plastic-based fabrication methods, and novel instrumentation approaches for label-free biodetection. He is a founder and the Chief Technical Officer of SRU Biosystems (Woburn, MA), a life science tools company that provides high sensitivity plastic-based optical biosensors, instrumentation, and software to the pharmaceutical, academic research, genomics, and proteomics communities. Prior to founding SRU Biosystems in June 2000, he was the Manager of Biomedical Technology at Draper Laboratory, where he directed R&D projects aimed at utilizing defense-related technical capabilities for medical applications. He also served as Group Leader for MEMS sensors at Draper. Concurrently, he was an Associate Director of the Center for Innovative Minimally Invasive Therapy (CIMIT), a Boston-area medical technology consortium, where he led the Advanced Technology Team on Microsensors. Before joining Draper, he spent 5 years at the Raytheon Electronic Systems Division. Dr. Cunningham earned BS, MS, and PhD degrees in Electrical and Computer Engineering at the University of Illinois.

Eric M. Hildebrant is a Principal Member of the Technical Staff. Initially, he worked on the MK6 CCD stellar sensor system. Later work focused on developing electronic integrated circuitry for micromechanical gyros, accelerometers, and chemical sensors. He holds four patents in the field of instrumentation. He received SB (1976), SB (1982), and MS (1989) degrees in Life Sciences, Electrical Engineering, and Engineering Design from MIT and Tufts University.



2006
patents
Issued

Anderson, J.M.; Kerrebrock, P.A.; McFarland, W.W.; Ogrodnik, T.G.
Crawler Device
Patent Number 7,137,465 B1, November 21, 2006

Antkowiak, B.M.; Carter, D.J.; Duwel, A.E.; Mescher, M.J.; Varghese, M.; Weinberg, M.S.
MEMS Piezoelectric Longitudinal Mode Resonator
Patent Number 7,005,946 B2, February 28, 2006

Coskren, W.D.; Parry, J.R.; Williams, J.R.; Sebelius, P.W.
Sensor Apparatus and Method of Using Same
Patent Number 7,100,689 B2, September 5, 2006

Elliott, R.D.; Ward, P.A.
Apparatus for and Method of Sensing a Measured Input
Patent Number 7,055,387 B2, June 6, 2006

Greenspan, R.L.; Przyjemski, J.M.
Method and System for Implementing a Communications Transceiver Using Modified GPS User Equipment
Patent Number 7,123,895 B2, October 17, 2006

Hansberry, M.L.; Ash, M.E.; Martorana, R.T.
Multi-Gimbaled Borehole Navigation System
Patent Number 7,093,370 B2, August 22, 2006

Miller, R.A.; Nazarov, E.G.; Eiceman, G.A.; Krylov, E.
Method and Apparatus for Electrospray Augmented High Field Asymmetric Ion Mobility Spectrometry
Patent Number 7,075,068 B2, July 11, 2006

Miller, R.A.; Nazarov, E.G.; Zapata, A.M.; Davis, C.E.; Eiceman, G.A.; Bashall, A.D.
Systems for Differential Ion Mobility Analysis
Patent Number 7,057,168 B2, June 6, 2006

Robbins, W.L.; Miller, R.A.
Spectrometer Chip Assembly
Patent Number 7,098,449 B1, August 29, 2006

Weinberg, M.S.; Cunningham, B.T.; Hildebrant, E.M.
Flexural Plate Wave Sensor
Patent Number 7,109,633 B2, September 19, 2006

Williams, J.R.; Cunningham, B.T.
Flexural Plate Wave Sensor and Array
Patent Number 7,000,453 B2, February 21, 2006

Williams, J.R.; Dineen Jr., D.A.; Prince J.R.
Microfluidic Ion-Selective Electrode Sensor System
Patent Number 7,101,472 B2, September 5, 2006

The 2006 Draper Distinguished

performance

Awards

DPA Screening Committee Members

The DPA was established in 1989 and is the most prestigious award that Draper bestows for extraordinary achievements by individuals or teams. These achievements must constitute a major technical accomplishment, the technical effort must entail highly challenging work of substantial benefit to the Laboratory and the outside community, include a recent discrete accomplishment that is clearly extraordinary and represents a standard of excellence for the Laboratory, and the responsible individual or core team can be identified as the prime participant(s) in achieving the significant results. This year's committee was chaired by Scott Uhland. Members included Heather Clark, Christopher Gibson, Lauren Kessler, Edward Lanzilotta, David Owen, Dora Ramos, Elliot Ranger, and Roger Wilmarth. Administrative support was provided by Noel Cassidy.

Chairman of the Board John R. Kreick and then-President Vincent Vitto presented the 2006 Draper Distinguished Performance Awards (DPAs) to a team and to an individual at the Annual Dinner of the Corporation on October 4, 2006.

Accelerated Delivery of Miniaturized Radio Frequency Communications Hardware

The Next Generation Fastraker team members responsible for hardware achieved production qualification of the first engineering model, which was the first mixed-signal multichip module ever qualified for production by Draper. Production qualification occurred earlier than scheduled and in a package so much smaller than the sponsor's specifications that the overall system size was reduced by nearly a factor of three.



(clockwise from left) Michael T. Clohecy, Vincent J. Attenasio, Jr., Don A. Black, Michael J. Matranga, John R. Burns III, Donald I. Schwartz, and (inside center) Valerie H. Lowe

Development and Strategic Distribution of a Geospatial Intelligence Networked System to Middle Eastern Military Force

Harold A. Bussey led the team that adapted the Draper-developed U.S. Air Force system for handling geospatial information for use by NATO forces in the Middle East. He delivered the system to users in the field and trained them in its use. The system's usefulness has led other military organizations to consider adopting it.



(l-r) President James D. Shields, Award Recipient Harold A. Bussey, and Chairman of the Board John R. Kreick

The 2007 Charles Stark draper Prize

The Charles Stark Draper Prize was established in 1988 to honor the memory of Dr. Charles Stark Draper, “the father of inertial navigation.” Awarded annually, the Prize was instituted by the National Academy of Engineering (NAE) and endowed by Draper Laboratory. It is recognized as one of the world’s preeminent awards for engineering achievement and honors individuals who, like Dr. Draper, developed a unique concept that has contributed significantly to the advancement of science and technology and the welfare and freedom of society.



Photo credit: Bill Truslow

Sir Timothy Berners-Lee

The 2007 Charles Stark Draper Prize was presented to Sir Timothy Berners-Lee at a ceremony on February 20 in Washington, D.C. According to the NAE, Berners-Lee “imaginatively combined ideas to create the World Wide Web, an extraordinary innovation that is rapidly transforming the way people store, access, and share information around the globe. Despite its short existence, the Web has contributed greatly to intellectual development and plays an important role in health care, environmental protection, commerce, banking, education, crime prevention, and the global dissemination of information.” In addition, he “demonstrated a high level of technical imagination in inventing this system to organize and display information on the Internet.” His innovations include the uniform resource identifier (URI), HyperText Markup Language (HTML), and HyperText Transfer Protocol (HTTP).

Berners-Lee proposed his concept for the Web in 1989 while at the European Organization for Nuclear Research (CERN), launched it on the Internet in 1991, and continued to refine its design through 1993. He designed the Web with public domain scalable software and an open architecture to allow other inventions to be built on it.

Berners-Lee is currently a senior researcher and holder of the 3Com Founders Chair at the Computer Science and Artificial Intelligence Laboratory at MIT and a professor of computer science in the School of Electronics and Computer Science at the University of Southampton, UK. He continues to guide the Web’s evolution as founder and director of the World Wide Web Consortium (W3C), an international forum that develops standards for the Web. A graduate of Oxford University, England, he became a fellow of the Royal Society in 2001. He has received several international awards, including the Japan Prize, the Prince of Asturias Foundation Prize, the Millennium Technology Prize, and Germany’s Die Quadriga Award. Berners-Lee was knighted by Queen Elizabeth in 2004. He is the author of “Weaving the Web.”

Recipients of the Charles Stark Draper Prize

- 2006:** Willard S. Boyle and George E. Smith for the invention of the charge-coupled device (CCD)
- 2005:** Minoru Araki, Francis J. Madden, Don H. Schoessler, Edward A. Miller, and James W. Plummer for their invention of the Corona earth-observation satellite technology
- 2004:** Alan C. Kay, Butler W. Lampson, Robert W. Taylor, and Charles P. Thacker for the development of the world's first practical networked personal computers
- 2003:** Ivan A. Getting and Bradford W. Parkinson for their technological achievements in the development of the Global Positioning System
- 2002:** Robert S. Langer for bioengineering revolutionary medical drug delivery systems
- 2001:** Vinton Cerf, Robert Kahn, Leonard Kleinrock, and Lawrence Roberts for their individual contributions to the development of the Internet
- 1999:** Charles K. Kao, Robert D. Maurer, and John B. MacChesney for development of fiber-optic technology
- 1997:** Vladimir Haensel for the development of the chemical engineering process of "Platforming" (short for Platinum Reforming), which was a platinum-based catalyst to efficiently convert petroleum into high-performance, cleaner-burning fuel
- 1995:** John R. Pierce and Harold A. Rosen for their development of communication satellite technology
- 1993:** John Backus for his development of FORTRAN, the first widely used, general-purpose, high-level computer language
- 1991:** Sir Frank Whittle and Hans J.P. von Ohain for their independent development of the turbojet engine
- 1989:** Jack S. Kilby and Robert N. Noyce for their independent development of the monolithic integrated circuit

For information on the nominating process, contact the Awards Office at the National Academy of Engineering at (202) 334-1266 or <http://www.nae.edu/awards>.

The 2006 Howard Musoff Student

mentoring

Award



Laura Forest

The 2006 Howard Musoff Student Mentoring Award was presented to Laura Forest, a Human-System Collaboration Engineer in the Software System Architectures and Human-Computer Interfaces (HCI) Department. When asked about the importance of mentoring activities, Laura remarked, “It has been very rewarding to mentor and work with Draper Laboratory Fellows (DLF) and other student interns. I have especially enjoyed witnessing the students’ transformation as they step from undergraduate classroom-based problem solving to the broader scope of engineering research and subsequent publishing. Seeing the students take the knowledge and experience I share with them and use it for their own growth is truly fulfilling. Mentoring can also establish life-long contacts and friendships – I’m planning on attending one of my former DLF’s wedding in Reno, NV, this summer. Additionally, the students contribute to my own professional development through the research areas they explore, the leadership opportunities they present, and the associated expansion of my academic contacts. I look forward to continuing mentoring relationships in the future.”

In addition to her mentoring activities at Draper, for the past two years, Laura has been a volunteer with Science Club for Girls, a weekly after-school program in Cambridge. Volunteers perform a variety of science experiments with the girls and discuss their careers as scientists.

Laura’s primary research interests include cognitive engineering, human-guided algorithms, human factors, and HCI. She is currently working on projects that include research on human-guided algorithms, spacecraft automation for lunar landing, decision support for intelligence analysts, and requirements for facial recognition systems. A member of the Human Factors and Ergonomics Society (HFES), Society of Women Engineers (SWE), IEEE, and AIAA, Laura has a BS in Industrial and Systems Engineering from Georgia Tech and an MS in Aeronautics and Astronautics from MIT.

The Howard Musoff Mentoring Award was established in his memory in 2005. A Draper employee for more than 40 years, Musoff advised and mentored many Draper Fellows. This award is given each February during National Engineers Week and recognizes staff members who, as Musoff did, share their expertise and supervise the professional development and research activities of Draper Fellows. The award, endowed by the Howard Musoff Charitable Foundation, includes a \$1,000 honorarium and a plaque. Each Engineering Division Leader may submit one nomination of a staff person from his Division. The Education Office assists in the process by soliciting comments from students who were residents during that time period. The Selection Committee consists of the Vice President of Engineering, the Principal Director of Engineering, and the Director of Education.

2006 Graduate research Theses

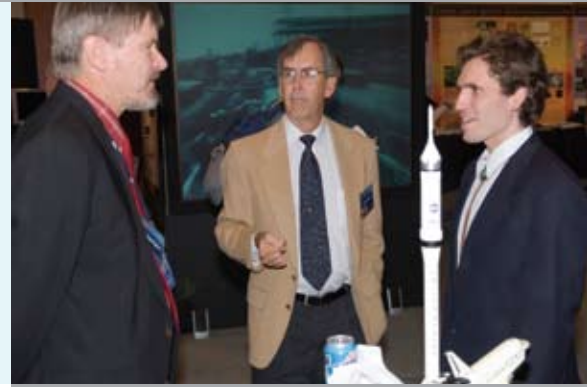
During 2006, the Draper Fellow Program served 65 students from MIT and several other universities. Abstracts of theses completed this year are available on the Laboratory's web site at www.draper.com. The list of completed theses follows:

- Anderson, A.D.; *Supervisors:* Gustafson, D.E.; Deyst, J.
Recovering Sample Diversity in Rao-Blackwellized Particle Filters for Simultaneous Localization and Mapping
Master of Science Thesis, MIT, June 2006
- Bairstow, S.H.; *Supervisors:* Barton, G.H.; Deyst, J.J.
Reentry Guidance with Extended Range Capability for Low L/D Spacecraft
Master of Science Thesis, MIT, February 2006
- Barker, D.R.; *Supervisors:* Singh, L.; How, J.
Robust Randomized Trajectory Planning for Satellite Attitude Tracking Control
Master of Science Thesis, MIT, June 2006
- Beaton, J.S.; *Supervisors:* Dever, C.W.; Appleby, B.D.
Human Inspiration for Autonomous Vehicle Tactics
Master of Science Thesis, MIT, May 2006
- Bryant, C.H.; *Supervisors:* Armacost, A.P.; Abramson, M.R.; Koltz, S.E.; Barnhart, C.
Robust Planning for Effects-Based Operations
Master of Science Thesis, MIT, June 2006
- Chau, D.; *Supervisors:* Racine, R.J.; Liskov, B.
Authenticated Messages for a Real-Time Fault-Tolerant Computer System
Master of Engineering Thesis, MIT, September 2006
- Earnest, C.A.; *Supervisors:* Dai, L.; Page, L.A.; Roy, N.; Barnhart, C.
Dynamic Action Spaces for Autonomous Search Operations
Master of Science Thesis, MIT, March 2006
- Harjes, D.I.; *Supervisors:* Clark, H.A.; Kamm, R.D.
High Throughput Optical Sensor Arrays for Drug Screening
Master of Science Thesis, MIT, September 2006
- Jimenez, A.R.; *Supervisors:* Kaelbling, L.P.; DeBietto, P.A.
Policy Search Approaches to Reinforcement Learning for Quadruped Locomotion
Master of Engineering Thesis, MIT, May 2006
- Krenzke, T.P.; *Supervisors:* McConley, M.W.; Appleby, B.D.
Ant Colony Optimization for Agile Motion Planning
Master of Science Thesis, MIT, June 2006
- McAllister, D.B.; *Supervisors:* Kahn, A.C.; Kaelbling, L.P.; Jaillet, P.
Planning with Imperfect Information: Interceptor Assignment
Master of Science Thesis, MIT, June 2006
- Mihok, B.E.; *Supervisors:* Miller, J.W.; Appleby, B.D.
Property-Based System Design Method with Application to a Targeting System for Small UAVs
Master of Science Thesis, MIT, June 2006
- Parikh, K.M.; *Supervisors:* Weinberg, M.S.; Freeman, D.M.
Modeling the Electrical Stimulation of Peripheral Vestibular Nerves
Master of Engineering Thesis, MIT, September 2006
- Ren, B.B.; *Supervisors:* Keshava, N.; Freeman, D.
Calibration, Feature Extraction and Classification of Water Contaminants Using a Differential Mobility Spectrometer
Master of Engineering Thesis, MIT, May 2006
- Sakamoto, P.; *Supervisors:* Armacost, A.P.; Koltz, S.E.; Barnhart, C.
UAV Mission Planning Under Uncertainty
Master of Science Thesis, MIT, June 2006
- Schaaf, B.T.; *Supervisors:* Andrews, G.L.; Appleby, B.D.
Using Learning Algorithms to Develop Dynamic Gaits for Legged Robots
Master of Science Thesis, MIT, June 2006
- Smith, C.A.; *Supervisors:* Cummings, M.L.; Forest, L.M.
Ecological Perceptual Aid for Precision Vertical Landings
Master of Science Thesis, MIT, June 2006
- Smith, T.B.; *Supervisors:* Nervegna, M.F.; Barnhart, C.
Decision Algorithms for Unmanned Underwater Vehicles During Offensive Operations
Master of Science Thesis, MIT, June 2006
- Springmann, P.N.; *Supervisors:* Proulx, R.J.; Deyst, J.J.
Lunar Descent Using Sequential Engine Shutdown
Master of Science Thesis, MIT, January 2006
- Sterling, R.M.; *Supervisors:* Racine, R.J.; Liskov, B.H.
Synchronous Communication System for a Software-Based Byzantine Fault-Tolerant Computer
Master of Science Thesis, MIT, August 2006
- Swanton, D.R.; *Supervisors:* Brown, R.A.; Kaelbling, L.P.
Integrating Timeliner and Autonomous Planning
Master of Science Thesis, MIT, August 2006
- Teahan, G.O.; *Supervisors:* Paschall II, S.C.; Battin, R.H.
Analysis and Design of Propulsive Guidance for Atmospheric Skip Entry Trajectories
Master of Science Thesis, MIT, June 2006
- Thrasher, S.W.; *Supervisors:* Dever, C.W.; Deyst, J.J.
Reactive/Deliberative Planner Using Genetic Algorithms on Tactical Primitives
Master of Science Thesis, MIT, June 2006
- Varsanik, J.S.; *Supervisors:* Duwel, A.E.; Kong, J-A
Design and Analysis of MEMS-Based Metamaterials
Master of Engineering Thesis, MIT, June 2006

2006

technology

Exposition



Ray Barrington (left) and Stephen Smith (center) discuss Draper's Space Programs with an interested visitor.

Each year, Draper hosts a Technology Exposition (Tech Expo) to showcase recent projects and highlight the Laboratory's core competencies. Held on October 4-5 to coincide with the fall meeting of Draper's Board of Directors and the Annual Meeting of the Corporation, guests included employees and Corporation members, students from local universities and Cambridge public schools, and sponsors.

The exhibits featured developing technologies in the Laboratory's program areas: strategic, tactical, space systems, special operations, biomedical engineering, and independent research and development. The exhibits also reflected the Laboratory's core competencies: guidance, navigation, and control; embedded, real-time software; microelectronics and packaging; autonomous systems; distributed systems; microelectromechanical systems; biomedical engineering; and prototyping system solutions. In coordination with Draper's Education Office, many projects also included graduate or undergraduate students on their teams.

Draper's subsidiary venture capital fund, Navigator Technology Ventures, LLC (NTV), displayed information about a number of its portfolio companies. These companies include Actuality Systems, Aircuity, Assertive Design, Food Quality Sensor (FQS) International, HistoRx, Polnox Corp., Polychromix, Renalworks Medical Corp., Sionex Corp., and Tizor Systems.



Malinda Tupper demonstrates one of several biological/chemical sensors under development as Draper continues to pursue the smallest, most robust, and selective electronic detection platforms.



Linda Fuhrman shares her enthusiasm for space exploration and Draper's role with Cambridge public school students.



Roger Wilmarth (left) and a Draper Fellow discuss innovations in small robotics systems for surveillance and rescue operations, including precision airdrop systems, small undersea vehicles, and systems designed to overcome difficult mobility challenges.



The Charles Stark Draper Laboratory, Inc.
555 Technology Square
Cambridge, MA 02139-3563
Phone: (617) 258-1000
www.draper.com

Business Development
busdev@draper.com
Phone: (617) 258-2124

Washington
Suite 501
1555 Wilson Boulevard
Arlington, VA 22209
Phone: (703) 243-2600

Houston
Suite 470
17629 El Camino Real
Houston, TX 77058
Phone: (281) 212-1101